

**Development of Copper Selenide Quantum Dots-Based
Therapeutic Drug Monitoring Biosensors for Toremifene –
A Breast Cancer Drug**



UNIVERSITY of the
WESTERN CAPE

By

Laura Gabriella Calmanovici Pacoste

A full thesis submitted in fulfilment of the requirements for the degree of

MAGISTER SCIENTIAE

In the Department of Chemistry, University of the Western Cape

Cape Town, South Africa

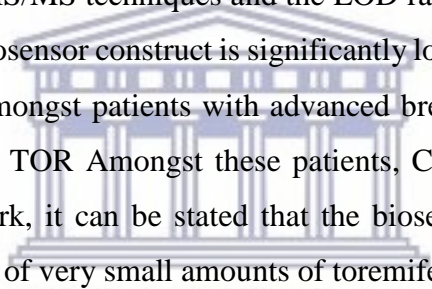
Supervisor: Prof Emmanuel Iwuoha

August, 2017

Abstract

With rising knowledge of the effects on plasma concentration caused by allelic variations in the cytochrome P450 genes and other metabolic factors such as drug-drug or drug-food interactions, more attention is paid to the possibility of therapeutic drug monitoring (TDM). Thus, there is a rising demand for quick, low-cost and efficient equipment for drug targeting. For such devices, electrochemical biosensing techniques serve as a promising alternative. Toremifene is the chlorinated analogue of tamoxifen and is used for adjuvant antiestrogenic treatment for breast cancer and could serve as a candidate for TDM treatments. In this work, a proof of concept enzymatic electrochemical biosensor is developed for the detection of toremifene in aqueous solution. The biosensor uses water-soluble 6-mercaptopropionic acid capped copper selenide quantum dots (6MHACuSe QDs) conjugated to a cysteamine self-assembled monolayer on a gold electrode. The 6MHACuSe QDs were further conjugated with CYP2C9 enzyme, which has shown to have a major part in the hydroxylation of toremifene (TOR) to form 4-hydroxytoremifene (4OH-TOR). The 6MHACuSe QDs were synthesized using a facile and rapid aqueous route. Results from synthesis of 3-mercaptopropionic acid (3MPA) and mercaptosuccinic acid (MSA) capped copper selenide QDs, are also presented in the study and compared to the results of the 6MHA capped copper selenide QDs. X-ray diffraction analysis (XRD) confirmed formation of copper selenide species of non-stoichiometric form Cu_{2-x}Se (for the 6MHA and 3MPA capped CuSe QDs) and $\beta\text{-CuSe}$ stoichiometric form (for the MSA capped CuSe QDs). XRD and high resolution electron microscopy (HRTEM) confirmed that 6MHA capped CuSe QDs had the smallest average particle core size when dried. Furthermore small-angle x-ray scattering (SAXS) and dynamic light scattering (DLS) showed MSA capped CuSe QDs had the smallest size in aqueous solution, though with a high ability to aggregate. The capping of CuSe QDs was confirmed by FTIR via the specific COOH, CH₂ and C-S signature bands of 3MPA and 6MHA. The water-soluble nature of the MSACuSe QDs pointed towards bonding of the thiol carboxylic acid. However, the MSA bond to the CuSe QDs is probably unstable, leading to lower stability of the QDs in aqueous solution. UV-vis absorption confirmed a large blue shift of the band gap compared to the bulk material for all formed QDs which is attributed to the quantum confinement effect. Photoluminescence (PL) measurements showed that the QDs emit light at 435 nm (6MHA and 3MPA capped CuSe QDs) and 485 nm (MSA capped CuSe QDs). Cyclic voltammetry studies confirmed favourable electrochemical properties showing that the QDs could be utilized as a component in electrochemical biosensors. This was further investigated

by applying the 6MHACuSe QDs in the final toremifene biosensor construct. Cyclic voltammetry (CV) and square-wave voltammetry (SWV) studies showed that the 6MHACuSe QDs served as an electron mediator and enzyme immobilizer on the electrode surface. The QDs also showed to retain the catalytic properties of the CYP2C9 enzyme. The small KM APP values obtained for CV and SWV (0.08 pM and 0.27 pM respectively) indicates high binding affinity between the substrate and CYP2C9 enzyme on the electrode surface. The biosensor response for the CV measurements had a very small dynamic linear range (DLR) up to 0.3 pM, $R^2 = 0.85078$, with a sensitivity of 241.2 nA pM^{-1} . The limit of detection (LOD) corresponded to 0.28 pg mL^{-1} . The DLR could be slightly improved by the use of SWV as a detection technique in comparison to cyclic voltammetry. The SWV measurements gave a DLR up to 0.6 pM ($R^2 = 0.98432$). The sensitivity obtained was 212.7 nA pM^{-1} with a LOD corresponding to 0.08 pg mL^{-1} . The LOD values obtained are lower than detection limits reported for other toremifene detection techniques. Toremifene in blood plasma or urine samples is commonly determined by HPLC or LC-MS/MS techniques and the LOD ranges within $0.2 - 30 \text{ ng mL}^{-1}$. In addition, the LODs of the biosensor construct is significantly lower than reported steady state plasma concentrations (C_{ss}) amongst patients with advanced breast cancer administered with 60 mg (normal daily dose) of TOR. Amongst these patients, $C_{ss} = 879 \text{ ng mL}^{-1}$. Thus, as a general conclusion of this work, it can be stated that the biosensor was shown to have the potential of detecting presence of very small amounts of toremifene in plasma samples.



UNIVERSITY of the
WESTERN CAPE

Keywords

Toremifene

Cytochrome P450 2C9 (CYP2C9)

Quantum dots

Self-assembled monolayers

Biosensors

Cyclic voltammetry

Square-wave voltammetry

Therapeutic drug monitoring (TDM)



UNIVERSITY *of the*
WESTERN CAPE

Declaration

I declare that “**Development of Copper Selenide Quantum Dots-Based Therapeutic Drug Monitoring Biosensors for Toremifene – A Breast Cancer Drug**” is my own work, that it has not been submitted before for any degree or examination at any other university, and that all the sources I have used or quoted have been indicated and acknowledged by complete references.

Laura Gabriella Calmanovici Pacoste

Signature:  Date: 2 October, 2017



Acknowledgements

I would like to give a special thanks to my supervisor, Prof Emmanuel Iwuoha, for guidance, support and for inspiring me throughout the work.

A warm thank you to my parents, Ina and Costin, for giving me love and support throughout. A special thanks to my sisters, Alexandra and Maria, for always lifting me up when I needed it. Also, a thank you to my partner Victor for his eternal support.

To my friends, Naturreservatet, thank you for always being there, believing in me and inspiring me.

To the Chemistry Department staff and SensorLab researchers, thank you for the inspiration, help and friendship.

Lastly, a special thanks to the sponsors of the Erasmus Mundus masters mobility program AESOP+, for making this year in South Africa possible for me and giving me the opportunity to conduct this study.



Dedication

This work is dedicated to: my late grandmother Georgeta Aurelia Calmanovici; my mother Ina Maria Calmanovici and father Costin Sorin Pacoste-Calmanovici, my sisters Maria Christina and Alexandra Maj Calmanovici Pacoste, and my partner Victor Nils Albert Eriksson.



UNIVERSITY *of the*
WESTERN CAPE

Table of Contents

| | |
|--|------|
| Abstract | i |
| Keywords | iii |
| Declaration | iv |
| Acknowledgements | v |
| Dedication | vi |
| List of Abbreviations..... | x |
| List of Figures | xiii |
| Chapter 1: Introduction | 1 |
| <i>Summary</i> | 1 |
| 1.1 Background..... | 2 |
| 1.1.1 Breast Cancer | 2 |
| 1.1.2 Treatment of Breast Cancer with Toremifene..... | 3 |
| 1.1.3 Motivation of the study..... | 5 |
| 1.2 Aims and objectives of the study..... | 7 |
| 1.3 Thesis layout..... | 8 |
| 1.4 References | 9 |
| Chapter 2: Literature review - The Role of Quantum Dots in Hemolytic Enzyme-based Electrochemical Biosensors | 12 |
| <i>Summary</i> | 12 |
| Abstract..... | 13 |
| 2.1 Introduction | 14 |
| 2.2 Redox center of Heme-containing Enzymes | 18 |
| 2.2.1 Monooxygenation reaction of CYP enzymes | 19 |
| 2.2.2 Mechanism of HRP Catalysis | 21 |
| 2.3 Quantum dots-based biosensors | 22 |
| 2.3.1 Biocompatible quantum dots | 22 |
| 2.3.2 Types of QDs biosensors | 23 |
| 2.4 Biosensing with QDs-CYP electrodes..... | 24 |
| 2.4.1 Electrochemical sensors..... | 24 |

| | |
|--|----|
| 2.4.2 Photoelectrochemical Sensors..... | 26 |
| 2.5 HRP-QDs bioelectrodes | 28 |
| 2.5.1 Peroxide sensors..... | 28 |
| 2.5.2 Other HRP analytes..... | 30 |
| 2.6 Other heme-enzyme biosensors | 33 |
| 2.7 Conclusions | 33 |
| 2.8 References | 35 |
| Chapter 3: Preparation of water-soluble CuSe QDs..... | 41 |
| <i>Summary</i> | 41 |
| Abstract..... | 42 |
| 3.1 Introduction | 43 |
| 3.2 Experimental..... | 46 |
| 3.2.1 Chemicals..... | 46 |
| 3.2.2 Instrumentation | 46 |
| 3.2.3 Synthesis of 6-mercaptohexanoic acid, 3-mercaptopropionic acid and mercaptosuccinic acid capped CuSe quantum dots | 47 |
| 3.2.4 Preparation of modified electrode..... | 48 |
| 3.3 Results and discussion | 49 |
| 3.3.1 Characterization | 49 |
| 3.3.2 Optical Properties..... | 64 |
| 3.3.3 Electrochemical properties..... | 72 |
| 3.4 Conclusion | 82 |
| 3.5 References | 83 |
| Chapter 4: Enzyme-based Toremifene Biosensor | 88 |
| <i>Summary</i> | 88 |
| Abstract..... | 89 |
| 4.1 Introduction | 90 |
| 4.2 Experimentals | 92 |
| 4.2.1 Chemicals..... | 92 |
| 4.2.2 Instrumentation | 92 |
| 4.2.3 Construction of Au/Cys/6MHACuSe/CYP2C9 biosensor | 93 |

| | |
|--|-----|
| 4.3 Results and discussion | 95 |
| 4.3.1 Characterization of Au/Cys/6MHACuSe/CYP2C9 electrode surface..... | 95 |
| 4.3.2 Electrochemical characterization of biosensor | 98 |
| 4.3.3 Biosensor detection response upon addition of toremifene citrate | 102 |
| 4.4 Conclusion | 107 |
| 4.5 References | 109 |
| Chapter 5: Conclusions and recommendations | 113 |
| <i>Summary</i> | 113 |
| 5.1 Conclusions and recommendations | 114 |
| 5.2 References | 118 |



UNIVERSITY *of the*
WESTERN CAPE

List of Abbreviations

| | |
|------------------|---|
| λ_{\max} | Absorption maxima |
| 3MPA | 3-mercaptopropionic acid |
| 4OH-NDM-TOR | 4-hydroxyl-N-desmethyl-toremifene |
| 4OH-TAM | 4-hydroxyl-tamoxifen |
| 4OH-TOR | 4-hydroxyl-toremifene |
| 6MHA | 6-mercaptophexanoic acid |
| 17EE | 17-alpha-ethinyl estradiol |
| Ab ₁ | Polyclonal goat antimouse IgG |
| Ab ₂ | HRP-labeled polyclonal goat antimouse IgG |
| Ag | Analyte mouse IgG |
| AFM | Atomic force microcopy |
| APTES | 3-aminopropyltriethoxysilane |
| AuNPs | Gold nanoparticles |
| AuSPE | Gold screen printed electrode |
| CB | Conduction band |
| CPR | Cytochrome P450 reductase |
| C _{ss} | Steady state plasma concentration |
| CuSe | Copper selenide |
| CV | Cyclic voltammetry |
| CYP | Cytochrome P450 |
| DFS | Disease-free survival |
| DLR | Dynamic linear range |
| DLS | Dynamic light scattering |
| DMSO | Dimethyl sulfoxide |
| DTSP | Di(N-hydroxylsuccinimide ester) |
| E2 | 17 β -estradiol |
| ECL | Electrochemiluminescent |

| | |
|--------------------|--|
| EDC | N-(3-dimethylaminopropyl)-N'-ethylcarbodiimide hydrochloride |
| EDS | Energy dispersive x-ray spectroscopy |
| E_{gap} | Band gap |
| Egd | Direct band gap |
| Egi | Indirect band gap |
| ER | Estrogen receptor |
| FTIR | Fourier transform infrared spectroscopy |
| FWHM | Full-width-at-half-maximum |
| Gly | Glyphosphate |
| HLMs | Human liver microsomes |
| HPLC | High performance liquid chromatography |
| HPR | Horse radish peroxidase |
| HRSEM | High resolution scanning electron microscopy |
| HRTEM | High resolution electron microscopy |
| hSO | Human sulfite oxidase |
| ITO | Indium tin oxide |
| K_M^{APP} | Michaelis-Menten constant |
| LC-MS/MS | Liquid chromatography-tandem mass spectrometry |
| LMCT | Ligand to metal charge transfer |
| LOD | Lower limit of detection |
| MS | Mesoporous |
| MSA | Mercaptosuccinic acid |
| NDM-TOR | N-desmethyl-toremifene |
| NHS | N-hydroxysuccinimide |
| OMS | Ordered mesoporous carbon |
| OS | Overall survival |
| PBS | Phosphate buffer saline |
| PDDA | Poly(diallyldimethylammonium chloride) |
| PDDA-GN | PDDA functionalized graphene |
| PDDF | Pair distance distribution function |

| | |
|--------|---|
| PDS | Poly dispersity index |
| PL | Photoluminescence |
| QDs | Quantum dots |
| SAED | Selected area electron diffraction |
| SAM | Self-assembled monolayer |
| SAXS | Small-angle x-ray scattering |
| SCE | Standard calomel electrode |
| SPE | Screen printed electrode |
| SSRIs | Selective serotonin reuptake inhibitors |
| SWV | Square wave voltammetry |
| TDM | Therapeutic drug monitoring |
| TGA | Thioglycolic acid |
| TNR | Total normalized reaction rate |
| UV-vis | Ultraviolet-visible |
| WHO | World health organization |
| VB | Valence band |
| XRD | X-ray diffraction |

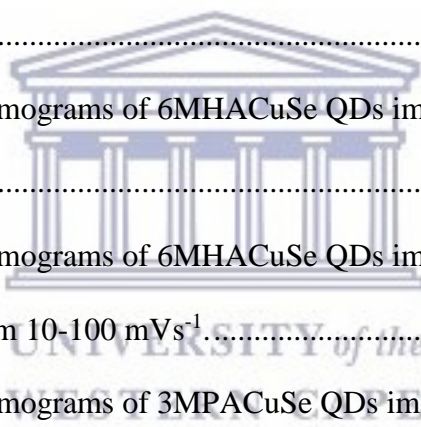


List of Figures

| | |
|--|----|
| Figure 1.1 Molecular structure of Toremifene (left) and Tamoxifen (right)..... | 3 |
| Figure 1.2 The suggested metabolic pathway of Toremifene to form its main metabolites: NDM-TOR, 4OH-TOR and 4OH-NDM-TOR. The figure illustrates the main enzymes involved and the metabolic contribution of each isoform normalized with the relative content of P450 in in pooled human liver microsomes in %TNR | 5 |
| Figure 2.1 The molecular structure of heme. | 18 |
| Figure 2.2 The catalytic cycle of cytochrome P450 enzymes for substrate hydroxylation..... | 20 |
| Figure 2.3 Peroxidases catalytic cycle for oxidation of xenobiotics. | 21 |
| Figure 2.4 Cyclic voltamograms of Au/Cys/CYP3A4, and Au/Cys/3MPA-ZnSe/CYP3A4 with 0.55 μM of E2 (black and red respectively) and without E2 (blue and green), in phosphate buffer of pH 7.4 at 40 mVs^{-1} | 25 |
| Figure 3.1 Molecular structure of MSA (left), 3MPA (middle) and 6MHA (right). | 44 |
| Figure 3.2 The X-ray diffractograms (left) and SAED spectra (right) of A) 6MHACuSe QDs B) 3MPACuSe QDs and C) MSACuSe QDs. | 49 |
| Figure 3.3 HRTEM images of 6MHACuSe QDs at magnitude of 0.20 μm (top), 10 nm (bottom left) and 2 nm (bottom right). Together with EDS graph (top), size distribution histogram (bottom left) and illustration of lattice fringes measures (bottom right)..... | 52 |
| Figure 3.4 HRTEM images of 3MPACuSe QDs at magnitude of 0.20 μm (top), 10 nm (bottom left) and 2 nm (bottom right). Together with EDS graph (top), size distribution histogram (bottom left) and illustration of lattice fringes measures (bottom right)..... | 53 |
| Figure 3.5 HRTEM images of MSACuSe QDs at magnitude of 0.20 μm (top), 10 nm (bottom left) and 2 nm (bottom right). Together with EDS graph (top), size distribution histogram (bottom left) and illustration of lattice fringes measures (bottom right)..... | 54 |

| | |
|---|----|
| Figure 3.6 HRSEM of 6MHACuSe on carbon SPE at magnitude of 1 μm (top) and 20 nm (bottom). EDS spectra is shown in top figure. | 56 |
| Figure 3.7 HRSEM of 3MPACuSe on carbon SPE at magnitude of 1 μm (top) and 20 nm (bottom). EDS spectra is shown in top figure. | 57 |
| Figure 3.8 HRSEM of MSACuSe on carbon SPE at magnitude of 1 μm (top) and 20 nm (bottom). EDS spectra is shown in top figure. | 58 |
| Figure 3.9 Representation of SAXS data for 6MHACuSe QDs in form of A) PDDF and B) particle radius (r) distributed by number of particles. | 60 |
| Figure 3.10 Representation of SAXS data for 3MPACuSe QDs in form of A) PDDF and B) particle radius (r) distributed by number of particles. | 60 |
| Figure 3.11 Representation of SAXS data for MSACuSe QDs in form of A) PDDF and B) particle radius (r) distributed by number of particles. | 61 |
| Figure 3.12 The FTIR spectra of MSACuSe QDs (green line), 3MPACuSe QDs (blue line) and 6MHACuSe QDs (red line). | 63 |
| Figure 3.13 Absorbance spectra of 6MHACuSe QDs (green line) and 1 mM aqueous solutions of $\text{Cu}(\text{NO}_3)_2$ (black line), NaOH (red line), 6MHA (deep blue line), $\text{Cu}(\text{NO}_3)_2$ and 6MHA mixture (light blue line), Se^{2-} (pink line). | 65 |
| Figure 3.14 6MHACuSe QDs absorption band with left insert corresponding to the direct band gap plot and right insert corresponding to the indirect band gap plot. | 65 |
| Figure 3.15 Absorbance spectra of 3MPACuSe QDs (green line) and 1 mM aqueous solutions of $\text{Cu}(\text{NO}_3)_2$ (black line), NaOH (red line), $\text{Cu}(\text{NO}_3)_2$ and 3MPA mixture (deep blue line), 3MPA (light blue line), Se^{2-} (pink line). | 67 |
| Figure 3.16 3MPACuSe QDs absorption band with left insert corresponding to the direct band gap plot and right insert corresponding to the indirect band gap plot. | 67 |

| | |
|---|----|
| Figure 3.17 Absorbance spectra of MSACuSe QDs (green line) and 1 mM aqueous solutions of Cu(NO ₃) ₂ (black line), NaOH (red line), Cu(NO ₃) ₂ and MSA mixture (deep blue line), MSA (light blue line), Se ²⁻ (pink line). | 68 |
| Figure 3.18 MSACuSe QDs absorption band with left insert corresponding to the direct band gap plot and right insert corresponding to the indirect band gap plot. | 68 |
| Figure 3.19 The excitation spectra (red line) and the emission spectra (black line) of 6MHACuSe QDs..... | 69 |
| Figure 3.20 The excitation spectra (red line) and the emission spectra (black line) of 3MPACuSe QDs. | 70 |
| Figure 3.21 The excitation spectra (red line) and the emission spectra (black line) of MSACuSe QDs. | 70 |
| Figure 3.22 The cyclic voltammograms of 6MHACuSe QDs immobilized on a bare Au electrode at 25 mVs ⁻¹ | 72 |
| Figure 3.23 The cyclic voltammograms of 6MHACuSe QDs immobilized on a bare Au at multiple scan rates varying from 10-100 mVs ⁻¹ | 72 |
| Figure 3.24 The cyclic voltammograms of 3MPACuSe QDs immobilized on a bare Au electrode at 25 mVs ⁻¹ | 73 |
| Figure 3.25 The cyclic voltammograms of 3MPACuSe QDs immobilized on a bare Au electrode at multiple scan rates varying from 10-100 mVs ⁻¹ | 73 |
| Figure 3.26 The cyclic voltammograms of MSACuSe QDs immobilized on a bare Au electrode at 25 mVs ⁻¹ | 74 |
| Figure 3.27 The cyclic voltammograms of MSACuSe QDs immobilized on a bare Au electrode at multiple scan rates varying from 10-100 mVs ⁻¹ | 74 |



| | |
|--|----|
| Figure 3.28 Cyclic voltammograms of 4 mM Cu(NO ₃) ₂ diluted in 0.1 M phosphate buffer (pH 7.40) measured with bare gold electrode with proposed reaction mechanisms responsible for the current peaks. | 77 |
| Figure 3.29 Cyclic voltammograms of 2 mM Se ²⁻ (right) diluted in 0.1 M phosphate buffer (pH 7.40) measured with bare gold electrode with proposed reaction mechanisms responsible for the current peaks. | 78 |
| Figure 3.30 Cyclic voltammogram measured with bare Au electrode of 32 mM 6MHA diluted in 0.1 phosphate buffer (pH 7.40) with proposed reaction mechanisms responsible for the current peaks. | 78 |
| Figure 3.31 Cyclic voltammogram measured with bare Au electrode of 32 mM 3MPA diluted in 0.1 phosphate buffer (pH 7.40) with proposed reaction mechanisms responsible for the current peaks. | 79 |
| Figure 3.32 Cyclic voltammogram measured with bare gold electrode of 32 mM MSA diluted in 0.1 phosphate buffer (pH 7.40) with proposed reaction mechanisms responsible for the current peaks. | 79 |
| Figure 4.1 Molecular structure of Toremifene (left) and Tamoxifen (right)..... | 90 |
| Figure 4.2 Schematic illustration of the biosensor formation. | 94 |
| Figure 4.3 The simulated topography of the bare AuSPE..... | 95 |
| Figure 4.4 The simulated topography of the Au/Cys modified AuSPE..... | 95 |
| Figure 4.5 The simulated topography of the Au/Cys/6MHACuSe modified AuSPE..... | 96 |
| Figure 4.6 The simulated topography of the biosensor constructed on AuSPE..... | 96 |
| Figure 4.7 Cyclic voltammogram of cysteamine covered gold electrode at anaerobic conditions (black line), aerobic condition (red line) and aerobic condition in presence of 1 pM TOR (blue line) at 25 mV s ⁻¹ scan rate in 0.1 M phosphate buffer (pH = 7.40). | 98 |

| | |
|--|-----|
| Figure 4.8 Cyclic voltammogram of Au/Cys/CYP2C9 modified electrode at anaerobic conditions (black line), aerobic condition (red line) and aerobic condition in presence of 1 pM TOR (blue line) at 25 mV s ⁻¹ scan rate in 0.1 M phosphate buffer (pH = 7.40). | 99 |
| Figure 4.9 Cyclic voltammogram of biosensor construct (Au/Cys/6MHACuSe/CYP2C9) at anaerobic conditions (blue line), aerobic condition (black line) and aerobic condition in presence of 1 pM TOR (red line) at 25 mV s ⁻¹ scan rate in 0.1 M phosphate buffer (pH = 7.40). | 99 |
| Figure 4.10 Cyclic voltammogram of the biosensor construct at different scan rates in full scale (left) and enlarge segment (right). | 100 |
| Figure 4.11 The reduction peak current (I _{pc}) of the reduction peak (occurring at E _{pc} = -631 mV) at different scan rates, for the biosensor construct. | 101 |
| Figure 4.12 Cyclic voltammogram of the biosensor construct at different TOR concentrations at full scale (left) and enlarged segment (right) at 25 mVs ⁻¹ in 0.1 M phosphate buffer (pH = 7.40). | 102 |
| Figure 4.13 The calibration plot of the current response (after subtraction of the 0 pM current response) for the reduction peak current occurring at E _{pc} = -631 mV to -589 mV. | 102 |
| Figure 4.14 The square-wave voltammograms of the biosensor construct at different TOR concentrations. | 104 |
| Figure 4.15 The calibration plot of the current response (after subtraction of the 0 pM current response) for the biosensor response from SWV measurements. | 104 |
| Figure 4.16 Proposed mechanism for reaction occurring at biosensor surface. | 106 |

Chapter 1: Introduction

Summary

This chapter gives an introduction to the need of the study. The problems that may occur with antiestrogenic treatment are explained together with the growing interest for personalized care and therapeutic drug monitoring. This chapter also explains the aims and objectives of the study which involves creating a biosensor for the detection of toremifene. The different parts of the study involve: synthesizing water soluble copper selenide quantum dots, modifying a gold electrode using cysteamine monolayer conjugated to quantum dots and cytochrome P450 2C9 enzyme and study the electrochemistry of the modified electrode in the presence of toremifene at different concentrations. Finally, the chapter presents the structure of the thesis.

1.1 Background

1.1.1 Breast Cancer

Breast cancer is the leading form of cancer amongst women and the number of cases are increasing. In the United States for instance, breast cancer is estimated to represent 30 % of the new cancer cases in 2017. This will result in 40 610 deaths within the American population. [1–3] Worldwide, breast cancer accounts for to 18.2 % of all cancer deaths.[4]

Cancer is caused by uncontrolled cell division of abnormal cells in a part of the body.[5] Most commonly breast cancers starts in the epithelial cells of the gland tissues in the breast. In such cases the cancer either starts in the milk ducts or in the milk producing glands called lobules. Less common types of breast cancers may also start in the cells of the fat, muscle or connective tissue.[6] The causes are not completely established but risk factors such as age, genetic impact and environmental factors plays a role in the likelihood of getting the disease.[4] The treatment used for breast cancer is depending on the cancer type and weather the cancer is *invasive* (has spread to surrounding tissue) or *in-situ* (in place).[6] The treatment can either consist of local treatment, such as radiation and operation, or systemic therapies using drugs. The systemic therapies involves chemo, hormone and targeted therapies. Amongst these, antiestrogenic treatments, such as tamoxifen, toremifene and raloxifene, has impact breast cancer treatment worldwide and has significantly reduced breast cancer recurrence and improved overall survival rate amongst women.[7]

However, there are still many problems remaining with the breast cancer treatments available today and the challenges regarding treatment response and the cancer reoccurring.[7] Lack of targeted hormone receptors in the cancer cells and hormone therapy resistance are some of the factors creating issues for the effectiveness of the hormonal cancer treatment.[7–9] Other potential problems could arise from individual allelic variations of drug metabolizing enzymes and interfering drug-drug interactions. Different approaches are taken to solve these issues in the aiming at reducing recurrence and mortality amongst patient. More interest is focused on the possibilities of personalized treatment and individual monitoring of administered drugs. [10–13]

1.1.2 Treatment of Breast Cancer with Toremifene

Antiestrogenic treatments is a fundament of medical breast cancer therapy, with tamoxifen as the oldest drug prescribed for these treatments.[14] Toremifene is the chlorinated analogue of Tamoxifen and both drugs falls under the category of selective estrogen receptor modulators (SERMs). SERMs binds to the estrogen receptor (ER). Depending on the tissue SERMs can act agonistic, which induces the effect of estrogen, or antagonistic, causing an antiestrogenic effect.[15–18] In general, SERMs exhibits antiestrogenic effects on the breast tissue, making them a useful treatment for ER-positive invasive breast cancer.[19,20] A cancer cell is said to be ER-positive if it contains estrogen receptors and thus relies on estrogen to grow. Antiestrogenic therapy aims to stop or reduce the estrogen induced growth of the cancer cells.[21] Some members of the SERM group of compounds, e.g. tamoxifen and raloxifene, has shown to significantly reduce the risk of breast cancer in women considered to be of high- and average-risk to develop the disease. These medications are also approved for preventative treatments of breast cancer. [20,22]

Toremifene was developed with the aim of making a more efficient antiestrogenic compound than Tamoxifen, for breast cancer treatment.[23] In 1997 the drug was approved by the U.S Food and Drug administration for treatment of advanced breast cancer in postmenopausal women with tumors that are ER+ or have an unknown ER status.[24,25] Toremifene differs from Tamoxifen with only one atom (Figure 1.1).

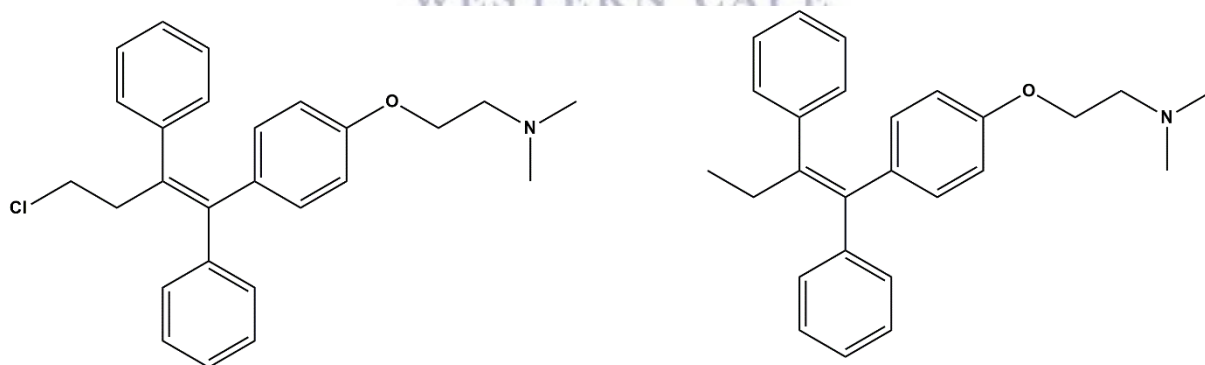


Figure 1.1 Molecular structure of Toremifene (left) and Tamoxifen (right).

Three prospective, randomized, controlled trials compared toremifene and tamoxifen as treatment of advanced breast cancer in postmenopausal women with ER+ or ER unknown tumors. All studies indicated that Toremifene and Tamoxifen are equally effective and safe treatments of postmenopausal women with ER+ and ER-unknown breast cancer.[26–28]

Studies has also been performed to investigate the difference between toremifene and tamoxifen as adjuvant treatment of postmenopausal women with endocrine-sensitive breast cancer. The studies compared the ratio of 5-year disease-free survival (DFS) and overall survival (OS). No significant difference in DFS and OS could be proven between the patient groups, indicating that the treatments have equal efficiency when used as adjuvant breast cancer therapy for the treatment of postmenopausal women.[27,29–33] Additionally, toremifene and tamoxifen have similar side effects and toxicity levels in both pre- and postmenopausal breast cancer patients.[29,33,34] However, a study performed on premenopausal breast cancer patients registered at Sun Yat-Sen Memorial Hospital (China) showed the same efficiency in overall 5-year survival but with significantly higher recurrence-free survival among the patients treated with Toremifene compared to patients treated with tamoxifen. [34] In vitro, the efficiency of toremifene in terms of ER affinity and growth inhibition of ER+ cancer cells is similar to that of tamoxifen. [23,35] However, two metabolites of tamoxifen which is 4-hydroxyl-tamoxifen (4OH-TAM) and 4-hydroxyl-N-desmethyl-Tamoxifen (endoxifen) are more potent in ER binding and inhibition of ER+ cancer cell growth than tamoxifen and toremifene. Thus, tamoxifen is often referred to as a prodrug with endoxifen as the main active metabolite.[35,10] Plasma concentrations of tamoxifen and its metabolites has shown to have significant variations in patients with different genotypes of the cytochrome P450 (CYP) 2D6 enzyme CYP. Furthermore, use of CYP2D6 inhibitors, for instance selective serotonin reuptake inhibitors (SSRIs), was also shown to give alteration in plasma concentration for tamoxifen and its metabolites. [10–12] Thus, the ability to metabolize tamoxifen into its active forms vary widely amongst individuals although there are still uncertainties on how these alterations actually affect the treatment outcome.[12]

Toremifene is not considered a prodrug and is not considered to be affected by CYP2D6 polymorphism alone. [12] A comparative metabolic study of Toremifene and Tamoxifen with human liver microsomes (HLMs) was performed by Watanabe and co-workers [35] This study suggested that CYP3A4 has the biggest impact on the direct metabolism of toremifene by catalyzing the N-demethylation of Toremifene to form N-desmethyl-Toremifene (NDM-TOR), which is the metabolite occurring in highest concentration in the plasma. Further, CYP2C9 had the biggest role in metabolizing toremifene to its second metabolite 4-hydroxyl-toremifene (4OH-TOR). Figure 1.2 shows the suggested reaction pathway along with the percentage of total normalized reaction rate (%TNR) which describes the metabolic contribution of each isoform normalized with the relative content of P450 in pooled human liver microsomes.[35]

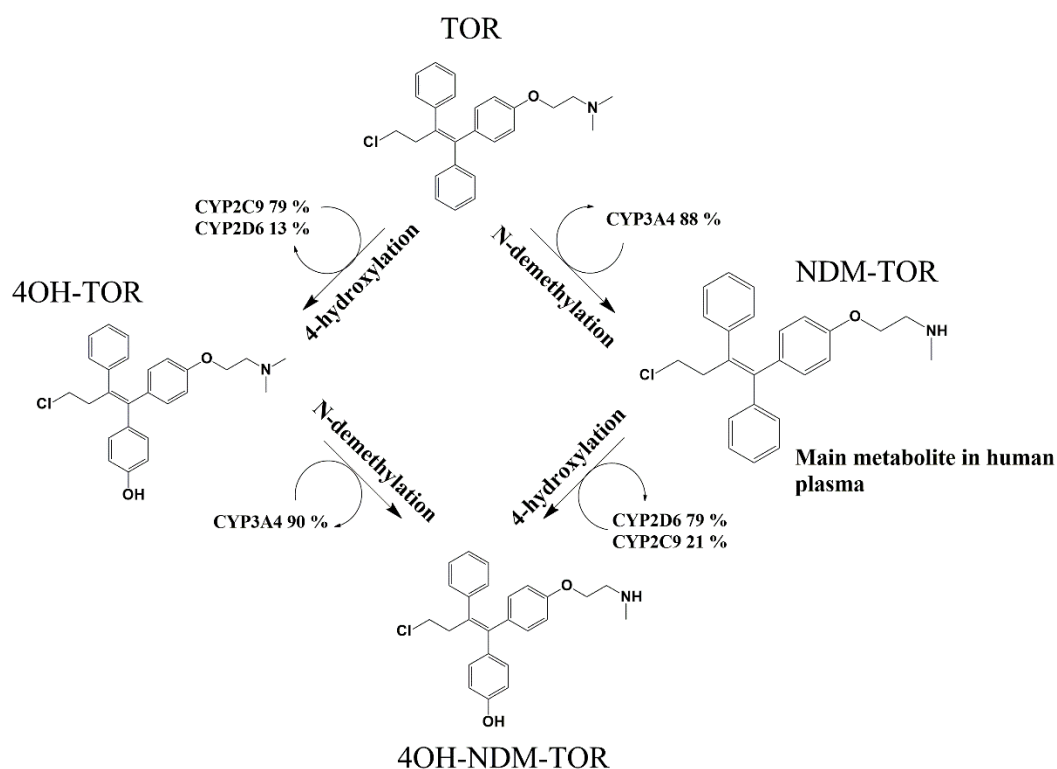


Figure 1.2 The suggested metabolic pathway of Toremifene to form its main metabolites: NDM-TOR, 4OH-TOR and 4OH-NDM-TOR. The figure illustrates the main enzymes involved and the metabolic contribution of each isoform normalized with the relative content of P450 in pooled human liver microsomes in %TNR, presented in the work by Watanabe and co-workers.[35]

The same study showed that both 4OH-TOR and 4OH-NDM-TOR had a much higher potency to inhibit ER+ cancer cell growth. However, based on plasma measurements of toremifene and its metabolites performed in previous research [36] the authors argue that these metabolites are cannot be responsible for the pharmacologic effects since their plasma concentration are low or undetectable. Thus, toremifene itself is responsible for the anticancer effect in vivo. [35,36]

1.1.3 Motivation of the study

Toremifene is to a lower extent than tamoxifen metabolized by the CYP2D6 enzyme and thus may be less influenced by allelic variations in of the CYP2D6 gene or drug-drug interactions. However, CYP2C9 enzyme, which has a bigger role in the toremifene metabolism, also has allelic variations of CYP2C9*2 and CYP2C9*3. To have polymorphic alteration in both the CYP2D6 and CYP2C9 is rare and constitutes less than 1 % of the Greek population.[37] However, in the comparative metabolic study by Watanabe and co-workers [35] the authors

discuss the possibility that decreased functional alleles of both CYP2D6 and CYP2C9 could influence the pharmacokinetics of toremifene amongst the patients carrying them. [35] Whether these polymorphic alterations actually effect the treatment outcome of toremifene therapy amongst the carrying population is still to investigate. However, with rising knowledge of the effects on plasma concentration caused by allelic variations in the cytochrome P450 genes and other metabolic factors such as drug-drug or drug-food interactions, more attention is paid to the possibility of therapeutic drug monitoring (TDM). The possibilities to observe the plasma concentration and moderate the doses individually between patients could optimize the dosing and treatment outcome. In a review by Widmer and co-workers [13] the authors analyze the benefits with therapeutic drug monitoring of anticancer drugs. The review demonstrates that TDM has had clinical benefits in some cases of cancer treatment where concentration-effect relationship has been studied.[13]

Toremifene and tamoxifen could be candidates for such personalized treatments. The methods used for TDM are often liquid chromatography-tandem mass spectrometry (LC-MS/MS), which is quick and efficient but expensive. [13,38,39] Laboratories not equipped with LC-MS/MS apparatus, High-performance liquid chromatography coupled to ultraviolet or fluorescence techniques is also an alternative. [40–42]. However, issues that may arise with these techniques is sampling of potentially significant amounts of blood, shipments to distant laboratory, extensive costs of the potentially expensive equipment, potential delays caused by delivery of results and possibly complex interpretation of data. Thus, technological developments that could facilitate the plasma measurements for TDM are needed.[13]

An enzyme based electrochemical biosensor for the target of toremifene could serve as a quicker, cheaper and more available method to measure plasma concentration, compared to the methods that are currently used. Such biosensor could also facilitate the possibility of research in the field of plasma concentrations relations to treatment outcome. In the study presented in this thesis a biosensor has been constructed. The biosensor was constructed using a gold electrode modified with a combination of CYP2C9 enzyme and copper selenide quantum dots as electron mediators. The purpose was to construct a toremifene biosensor that could detect the concentration status in plasma samples.

1.2 Aims and objectives of the study

The aims of this study is to construct a biosensor for detection of toremifene drug as a proof of concept drug monitoring tool. The biosensor could be used for further development of effective, portable devices to measure plasma concentration of patients during treatment. Furthermore, the aim of the study was to provide a tool for further understanding of the drug and its metabolites. The biosensor is constructed using a gold electrode, cysteamine (Cys), 6-mercaptophexanoic acid capped copper selenide quantum dots (6MHA-CuSe QDs) and CYP2C9 enzyme. Construction of the Au/Cys/6MHACuSe/CYP2C9 biosensor involves following steps:

- I. Formation of self-assembled monolayers (SAMs) of cysteamine on gold electrode surface by utilizing the strong covalent interaction between the gold surface and the thiol group of the cysteamine. This will create the Au/Cys modified electrode.
- II. Synthesis of CuSe QDs capped with 6-mercaptophexanoic acid using aqueous method. This will be followed by immobilization of 6MHACuSe QDs on Au/Cys modified electrode by letting it react chemically for 5 h with free amino groups of the cysteamine in presence of cross-linking agents (EDC/NHS), giving rise to a strong ester bond.
- III. Construction of a biosensor by binding the amino groups of CYP3A4 enzyme with Au/Cys/6MHACuSe surface through the carboxylic acid of the quantum dots.
- IV. Characterisation of Au/Cys/6MHACuSe/CYP2C9 biosensor using cyclic voltammetry (CV), square wave voltammetry (SWV) in presence and absence of toremifene.

1.3 Thesis layout

This thesis consists of 5 chapters:

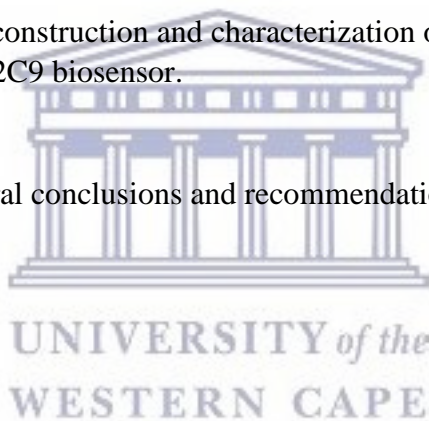
Chapter 1: Provides an introduction to the thesis giving the background of the topic, problem statement, motivations and aims and objectives of the study.

Chapter 2: Contains a detailed literature review on the topic: “The Role of Quantum Dots in Hemolytic Enzyme-Based Electrochemical Biosensors”.

Chapter 3: Describes the synthesis, characterization and electrochemical properties of water soluble copper selenide quantum dots using different capping agents.

Chapter 4: Describes the construction and characterization of the Au/Cys/6MHACuSe/CYP2C9 biosensor.

Chapter 5: Provides general conclusions and recommendations for the work presented.



1.4 References

- [1] R.L. Siegel, K.D. Miller, A. Jemal, *Cancer Statistics*, 2016, *A Cancer J. Clin.* 66 (2016) 7–30. doi:10.3322/caac.21332.
- [2] R.L. Siegel, K.D. Miller, A. Jemal, *Cancer Statistics*, 2017, *A Cancer J. Clin.* 67 (2017) 7–30. doi:10.3322/caac.21387.
- [3] P. Chalasani, J. Kiluk V, *Breast Cancer*, *MedScape*. (2017) 4–6. <http://emedicine.medscape.com/article/1947145-overview>.
- [4] C. Nordqvist, *Breast Cancer: Causes, Symptoms and Treatments*, *Med. News Today*. (2017) 1–15. <http://www.medicalnewstoday.com/articles/37136.php>.
- [5] National Cancer Institute, *What Is Cancer? Differences between Cancer Cells and Normal Cells*, *Natl. Cancer Inst.* (2015) 1–7. <https://www.cancer.gov/about-cancer/understanding/what-is-cancer>.
- [6] The American Cancer Society medical and editorial content team, *Types of Breast Cancer*, *Am. Cancer Soc.* (2016) 1–5. https://www.cancer.org/cancer/breast-cancer/understanding-a-breast-cancer-diagnosis/types-of-breast-cancer.html#written_by.
- [7] G.W. Sledge, E.P. Mamounas, G.N. Hortobagyi, H.J. Burstein, P.J. Goodwin, A.C. Wolff, Past, Present, and Future Challenges in Breast Cancer Treatment, *J. Clin. Oncol.* 32 (2014) 1979–1986. https://www.cancer.org/cancer/breast-cancer/understanding-a-breast-cancer-diagnosis/types-of-breast-cancer.html#written_by.
- [8] A. Prat, B. Adamo, M.C.U. Cheang, C.K. Anders, L.A. Carey, C.M. Perou, *Molecular characterization of basal-like and non-basal-like triple-negative breast cancer*, *Oncologist*. 18 (2013) 123–133.
- [9] C. Davies, H. Pan, J. Godwin, R. Gray, R. Arriagada, V. Raina, M. Abraham, V. Hugo, M. Alencar, A. Badran, X. Bonfill, J. Bradbury, M. Clarke, R. Collins, A. Delmestri, P. Haddad, F. Hou, M. Inbar, H. Khaled, J. Kielanowska, H. Kwan, A. Nicolucci, O. Peralta, F. Pernas, L. Petruzella, T. Pienkowski, B. Rajan, S. Tort, G. Urr, M. Valentini, Y. Wang, R. Peto, A. Tamoxifen, L.A. Shorter, C. Group, *Long-term effects of continuing adjuvant tamoxifen to 10 years versus stopping at 5 years after diagnosis of oestrogen receptor- positive breast cancer: ATLAS, a randomised trial*, *Lancet*. 381 (2013) 805–816. doi:10.1016/S0140.
- [10] Y. Jin, Z. Desta, V. Stearns, B. Ward, H. Ho, K. Lee, T. Skaar, A.M. Storniolo, L. Li, A. Araba, R. Blanchard, A. Nguyen, L. Ullmer, J. Hayden, S. Lemler, R.M. Weinsilboum, J.M. Rae, D.F. Hayes, D.A. Flockhart, *CYP2D6 Genotype, Antidepressant Use, and Tamoxifen Metabolism During Adjuvant Breast Cancer Treatment*, *J. Natl. Cancer Inst.* 97 (2005) 30–39. doi:10.1093/jnci/dji005.
- [11] S. Borges, Z. Desta, L. Li, T.C. Skaar, B.A. Ward, A. Nguyen, Y. Jin, A.M. Storniolo, D.M. Nikoloff, L. Wu, G. Hillman, D.F. Hayes, V. Stearns, D.A. Flockhart, *Quantitative effect of CYP2D6 genotype and inhibitors on tamoxifen metabolism: Implication for optimization of breast cancer treatment*, *Clin. Pharmacol. Ther.* 80 (2006) 61–74. doi:10.1124/jpet.104.065607.
- [12] C.L. Vogel, M.A. Johnston, C. Capers, D. Braccia, *Toremifene for Breast Cancer: A Review of 20 Years of Data*, *Clin. Breast Cancer*. 14 (2014) 1–9. doi:10.1016/j.clbc.2013.10.014.
- [13] N. Widmer, C. Bardin, E. Chatelut, A. Paci, G. Veal, A. Astier, J. Beijnen, D. Leve, *Review of therapeutic drug monitoring of anticancer drugs part two – Targeted therapies*, *Eur. J. Cancer*. 50 (2014) 2020–2036.

- [14] R. Kumar Gara, V. Sundram, S. C. Chauhan, M. Jaggi, Anti-Cancer Potential of a Novel SERM Ormeloxifene, 20 (2014) 4177–4184.
- [15] K. Dahlman-wright, V. Cavailles, S.A. Fuqua, V.C. Jordan, J.A. Katzenellenbogen, K.S. Korach, A. Maggi, M. Muramatsu, M.G. Parker, J.-åke Gustafsson, International Union of Pharmacology . LXIV . Estrogen Receptors, 58 (2006) 773–781. doi:10.1124/pr.58.4.8.773.
- [16] T.R. Ediger, P.G. V Martini, M. Montano, J. Sun, K. Weis, J.A. Katzenellenbogen, Molecular mechanisms of estrogen action : selective ligands and, 74 (2000) 279–285.
- [17] B.S. Komm, S. Mirkin, An overview of current and emerging SERMs, J. Steroid Biochem. Mol. Biol. 143 (2014) 207–222.
- [18] J.H. Pickar, T. Macneil, K. Ohleth, SERMs : Progress and future perspectives, Maturitas. 67 (2010) 129–138. doi:10.1016/j.maturitas.2010.05.009.
- [19] M. Sato, R. Mk, B. Hu, Raloxifene , tamoxifen , nafoxidine , or estrogen effects on reproductive and nonreproductive tissues in ovariectomized rats ., Faseb J. 10 (1996) 1–2.
- [20] S. Mirkin, J.H. Pickar, Selective estrogen receptor modulators (SERMs): A review of clinical data, Maturitas. 80 (2015) 52–57.
- [21] M.E.H. Hammond, D.F. Hayes, M. Dowsett, D.C. Allred, K.L. Hagerty, S. Badve, P.L. Fitzgibbons, G. Francis, N.S. Goldstein, M. Hayes, D.G. Hicks, S. Lester, R. Love, P.B. Mangu, L. Mcshane, K. Miller, C.K. Osborne, S. Paik, J. Perlmutter, A. Rhodes, H. Sasano, J.N. Schwartz, F.C.G. Sweep, S. Taube, E.E. Torlakovic, P. Valenstein, G. Viale, D. Visscher, T. Wheeler, R.B. Williams, J.L. Wittliff, A.C. Wolff, American Society of Clinical Oncology / College of American Pathologists Guideline Recommendations for Immunohistochemical Testing of Estrogen and Progesterone Receptors in Breast Cancer (Unabridged Version), Arch. Pathol. Lab. Med. 134 (2010) e48–e72.
- [22] J. V Pinkerton, S. Thomas, Use of SERMs for treatment in postmenopausal women, J. Steroid Biochem. Mol. Biol. 142 (2014) 142–154.
- [23] L. Kangas, Review of the pharmacological properties of toremifene, J. Steroid Biochem. 36 (1990) 191–195.
- [24] European Medicines Agency, Fareston: EPAR - Scientific discussion, (2005) 1–5.
- [25] NJ Bridgewater, Fareston_ [package insert], Kyowa Kirin Inc. (1997). <http://www.fareston.com/uploads/documents/fareston-pi.pdf>.
- [26] M. Gershanovich, A. Garin, D. Baltina, A. Kurvet, L. Kangas, J. Ellme, A phase III comparison of two toremifene doses to tamoxifen in postmenopausal women with advanced breast cancer, Breast Cancer Res. Treat. 45 (1997) 251–262.
- [27] S. Pyrhonen, R. Valavaara, H. Modig, M. Pawlicki, T. Pienkowski, S. Gundersen, J. Bauer, G. Westman, S. Lundgren, Comparison of toremifene and tamoxifen in post- menopausal patients with advanced breast cancer : a randomized double-blind , the â€™™ nordic â€™™ phase III study, Br. J. Cancer. 76 (1997) 270–277.
- [28] D. Hayes, J. Van Zyl, W. Bezwoda, J. Mailliard, S. Jones, C. Vogel, R. Berris, Randomized comparison of tamoxifen and two separate doses of toremifene in postmenopausal patients with metastatic breast, J. Clin. Oncol. 13 (1995) 1–2. doi:10.1200/JCO.1995.13.10.2556.
- [29] International Breast Cancer Study Group, Original article Toremifene and tamoxifen are equally effective for early-stage breast cancer : first results of International Breast Cancer Study Group Trials 12-93 and 14-93, Ann. Oncol. (2004) 1749–1759. doi:10.1093/annonc/mdh463.
- [30] J.D. Lewis, A.B. Chagpar, E.A. Shaughnessy, J. Nurko, K. McMasters, M.J. Edwards,

- Excellent outcomes with adjuvant toremifene or tamoxifen in early stage breast cancer, *Cancer*. 116 (2010) 2307–2315.
- [31] W.Z. Qiang, D. Ling, Toremifene is an effective and safe alternative to tamoxifen in adjuvant endocrine therapy for breast cancer : results of four randomized trials, *Breast Cancer Res. Treat.* 128 (2011) 625–631. doi:10.1007/s10549-011-1556-5.
- [32] S. Tafazoli, P.J. O'Brien, Peroxidases: A role in the metabolism and side effects of drugs, *Drug Discov. Today*. 10 (2005) 617–625. doi:10.1016/S1359-6446(05)03394-5.
- [33] K. Holli, R. Valavaara, G. Blanco, V. Kataja, P. Hietanen, M. Flander, E. Pukkala, H. Joensuu, Safety and efficacy results of a randomized trial comparing adjuvant toremifene and tamoxifen in postmenopausal patients with node-positive breast cancer, *J. Clin. Oncol.* 18 (2000) 3487–3494.
- [34] R. Gu, W. Jia, Y. Zeng, N. Rao, Y. Hu, S. Li, J. Wu, L. Jin, A comparison of survival outcomes and side effects of toremifene or tamoxifen therapy in premenopausal estrogen and progesterone receptor positive breast cancer patients : a retrospective cohort study, *BMC Cancer*. 12 (2012) 1–10.
- [35] M. Watanabe, N. Watanabe, S. Maruyama, T. Kawashiro, Comparative metabolic study between two selective estrogen receptor modulators , toremifene and tamoxifen , in human liver microsomes *, *Drug Metab. Pharmacokinet.* 30 (2015) 325–333.
- [36] J. Kim, C.C. Coss, C.M. Barrett, M.L. Mohler, C.E. Bohl, C.M. Li, Y. He, J.T. Dalton, Role and pharmacologic significance of cytochrome P-450 2D6 in oxidative metabolism of toremifene and tamoxifen †‡, *Int. J. Cancer*. 132 (2013) 1475–1485. doi:10.1002/ijc.27794.
- [37] K. Arvanitidis, G. Ragia, M. Iordanidou, S. Kyriaki, A. Xanthi, A. Tavidou, V.G. Manolopoulos, Genetic polymorphisms of drug-metabolizing enzymes CYP2D6, CYP2C9, CYP2C19 and CYP3A5 in the Greek population, *Fundam. Clin. Pharmacol.* 21 (2007) 419–426. doi:10.1111/j.1472-8206.2007.00510.x.
- [38] A. Haouala, B. Zanolari, B. Rochat, M. Montemurro, K. Zaman, M.A. Duchosal, H.B. Ris, S. Leyvraz, N. Widmer, L.A. Decosterd, Therapeutic Drug Monitoring of the new targeted anticancer agents imatinib, nilotinib, dasatinib, sunitinib, sorafenib and lapatinib by LC tandem mass spectrometry, *J. Chromatogr. B Anal. Technol. Biomed. Life Sci.* 877 (2009) 1982–1996. doi:10.1016/j.jchromb.2009.04.045.
- [39] S. Bouchet, E. Chauzit, D. Ducint, N. Castaing, M. Canal-Raffin, N. Moore, K. Titier, M. Molimard, Simultaneous determination of nine tyrosine kinase inhibitors by 96-well solid-phase extraction and ultra performance LC/MS-MS, *Clin. Chim. Acta.* 412 (2011) 1060–1067. doi:10.1016/j.cca.2011.02.023.
- [40] N. Widmer, A. Béguin, B. Rochat, T. Buclin, T. Kovacsovics, M.A. Duchosal, S. Leyvraz, A. Rosselet, J. Biollaz, L.A. Decosterd, Determination of imatinib (Gleevec®) in human plasma by solid-phase extraction-liquid chromatography-ultraviolet absorbance detection, *J. Chromatogr. B Anal. Technol. Biomed. Life Sci.* 803 (2004) 285–292. doi:10.1016/j.jchromb.2004.01.006.
- [41] S. Pursche, O.G. Ottmann, G. Ehninger, E. Schleyer, High-performance liquid chromatography method with ultraviolet detection for the quantification of the BCR-ABL inhibitor nilotinib (AMN107) in plasma, urine, culture medium and cell preparations, *J. Chromatogr. B Anal. Technol. Biomed. Life Sci.* 852 (2007) 208–216. doi:10.1016/j.jchromb.2007.01.019.
- [42] E.O. Aranda, J. Esteve-Romero, M. Rambla-Alegre, J. Peris-Vicente, D. Bose, Development of a methodology to quantify tamoxifen and endoxifen in breast cancer patients by micellar liquid chromatography and validation according to the ICH guidelines, *Talanta*. 84 (2011) 314–318. doi:10.1016/j.talanta.2011.01.022.

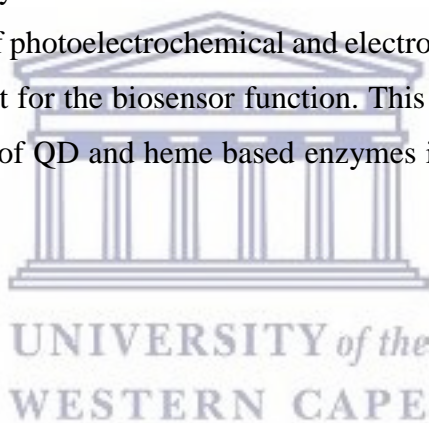
Chapter 2: Literature review - The Role of Quantum Dots in Hemolytic Enzyme-based Electrochemical Biosensors

Summary

The chapter contains a literature review regarding the work published on the role of quantum dots as a component of heme enzyme-based electrochemical biosensors. The chapter gives an introduction to the topic of enzyme based electrochemical biosensor and quantum dots. The chapter also describes the catalytic cycles of cytochrome P450 and peroxidases for substrate oxidation. Lastly, the review summarizes studies on the combination of QD and heme based enzymes in electrochemical biosensors, their structure and function.

Abstract

Electrochemical biosensors has shown promising possibilities as a molecular detection tool, mainly due to their fast response, low cost, high sensitivity and uncomplicated operation for analyte detection. The use of heme based enzymes as a biorecognition element for such constructs has been widely explored with promising results for molecular detection. However, frequent attempts are made to improve sensitivity and selectivity. Thus, the implementation of quantum dots (QDs) in combination with heme based enzymes has recently gained interest in the research world. QDs are semiconductive nanocrystals with 2-10 nm diameter. Due to their specific quantum confinement effect, accredited to their small size, the QDs have shown promising optical and electrochemical properties. In combination with heme based enzymes the quantum dots have shown to provide a stable microenvironment. High maintenance of the biological activity of the enzyme has been shown when immobilized on a QD modified electrode surface. In the case of photoelectrochemical and electrochemiluminescent biosensors, the QDs provide a key element for the biosensor function. This review summarizes a number of studies on the combination of QD and heme based enzymes in electrochemical biosensors, their structure and function.



2.1 Introduction

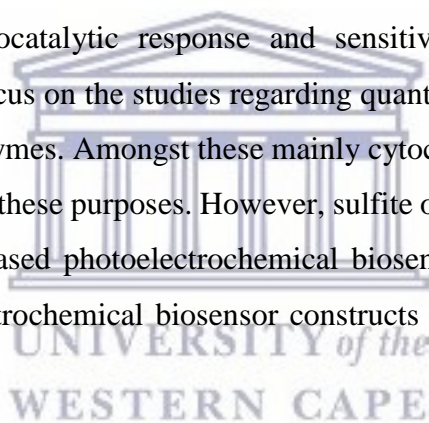
In the latest years, electrochemical biosensors has been developed for various pharmaceutical and clinical applications. One well known example is the glucose biosensor for self-monitoring of blood glucose in diabetic patients. [1–3] Due to a higher interest in personalized treatments, real-time drug monitoring and point-of-care disease diagnostics, there is a need for efficient, cheap and quick biological sensors capable of detecting a certain biological molecule. [2–4] Currently, drug targeting for therapeutic monitoring of anticancer drugs is mostly performed using liquid chromatography-tandem mass spectrometry (LC-MS/MS) [3,5,6] For laboratories unequipped with this technology, High-performance liquid chromatography coupled to ultraviolet or fluorescent techniques can be used. [7–9] However, these techniques have issues caused by expensive equipment, potential need to transport the samples to distant laboratories and complex data interpretation. [3] In contrast, electrochemical biosensors has shown advantages in comparison to the conventional drug-targeting methods, due to their fast response, low expenses, high sensitivity and uncomplicated operation for analyte detection. [10–13]

A biosensor consists of two key elements: the bioreceptor and the transducer. The bioreceptor is a biological molecule capable of identifying the target analyte. Antibodies, enzyme, membranes and cells are some examples of what the receptor can consist of. Whereas the transducer translate the carrying energy from the identifying reaction into an analytical signal. In electrochemical biosensors, the biological reaction between the biosensor and analyte causes a detectable electrical signal. [14,15] The use of enzymes as the bioreceptor components in electrochemical biosensors has shown certain advantages in detection of specific analytes, mainly due to their ability to specifically bind to a substrate but also detect many different analytes. In addition, enzymes are not consumed after the interaction with is target substrate, which enables continuous use of the detector. There are however other disadvantages related to the enzyme being sensitive to multiple factors in the surrounding conditions such as pH, temperature and inhibition caused by certain chemicals. [4] Amongst the various enzyme used for such electrochemical biosensor constructions, heme based enzymes has shown great potential for detection of various substrates. Two families of heme based enzymes that has been widely studies as a bioelectrode component is cytochrome P450s (CYPs) and peroxidases, thus especially horse radish peroxidase. [2,16–21]

Cytochrome P450s is a family of enzymes, all with a critical heme group, that metabolizes many xenobiotic (industrially synthesized compounds) and many commonly used prescription

drugs. [22] Electrochemical biosensor using different CYPs immobilized on the electrode surface has been created for a wide range of applications such as anti-tuberculosis drug monitoring, cocaine detection and metabolic study of bisphenol A. [16–18] The possibility of using CYPs electrochemical biosensor both as drug targeting techniques and for metabolic studies of drugs has given rise to many studies and applications. Frequently, new ways to increase the performance and sensitivity of these sensors are investigated. [21] Like CYPs, peroxidases are heme containing enzymes that plays a big role in drug metabolism. By using hydrogen peroxide (H_2O_2) peroxidases catalyzes oxidation of many different oxidizable xenobiotics.[23] Amongst the peroxidases, horseradish peroxidase (HRP), has been explored in a great amount of biosensor constructs, optical as well as electrochemical. [19,20,24–29]

Recently, the use of quantum dots (QDs) as an electron mediator between the electrode and the heme based enzyme in electrochemical biosensors has been investigated. QDs makes a good material for enzyme immobilization. For such applications, studies have reported promising results with enhanced electrocatalytic response and sensitivity for the target substrate. [10,28,30] This review will focus on the studies regarding quantum dot based electrochemical biosensors on heme based enzymes. Amongst these mainly cytochrome P450s and horseradish peroxidase have been used for these purposes. However, sulfite oxidase has also been explored as a part of a quantum dot based photoelectrochemical biosensor. [10,20,29–33] Table 2.1 shows a summary of the electrochemical biosensor constructs combining quantum dots and heme based enzymes.



| Enzyme | Quantum Dots | Other electrode modification | Electrode material | Results | Reference |
|---------------|---|---|---------------------------|---|-------------------------------|
| CYP3A4 | 3-mercaptopropionic acid capped ZnSe QDs | L-cysteamine self-assembled monolayer | Gold | Reduction peak at -200 mV in presence of 0.33 μ M of 17 β -estradiol. | Ndangili and co-workers [10] |
| CYP3A4 | 3-mercaptopropionic acid capped Ga ₂ Se ₃ QDs | L-cysteine self-assembled monolayer | Gold | Irreversible reduction peak at -220 mV in presence of 17-alpha-ethinyl estradiol | Nxusani and co-workers [30] |
| CYP2C9 | Thioglycolic acid functionalized CdTe QDs | Surface immobilized 3-aminopropyltriethoxysilane | Indium tin oxide | Chatodic photocurrent observed at -200 mV | Xu and co-workers[31] |
| CYP2D6 | 3-mercaptopropionic acid capped CdSe QDs. | Amino-functionalized surface | Indium tin oxide | Photocurrent response at applied potential of -200 mV attributed to catalytic activity of enzyme | Qian and co-workers [32] |
| HRP | CdSe/ZnS QDs | None | Glassy carbon | Reduction peak and oxidation peak detected between -177 and -242 mV with 65 mV peak separation in presence of H ₂ O ₂ | Wang and co-workers [29] |
| HRP | CdSe QDs within a template of mesoporous silica (MS) spheres | None | Indium tin oxide | Enhancement of current response when illuminated with UV in presence of H ₂ O ₂ | Yang and co-workers [34] |
| HRP | CdTe-CdS core-shell QDs | Graphene-gold nanocomposites, gold nanoparticles | Gold | Increased cathodic and anodic current attributed to catalytic activity of enzyme towards H ₂ O ₂ . | Zhiguo and co-workers [20] |
| HRP | Graphene QDs | Chitosan | Glassy carbon | Reduction current with onset potential -320 mV and half-wave potential -455 mV in presence of H ₂ O ₂ | Muthurasu and co-workers [19] |
| HRP | Graphene QDs | Thiol-tethered oligodeoxynucleotide probes, target DNA, aminated indicator probe (NH ₂ -DNA) | Gold | Amperometric current response in presence of target analyte miRNA | Hu and co-workers [28] |
| HRP | ZnS QDs | Ordered mesoporous carbon, Chitosan | Glassy carbon | Detectable electrochemiluminescent response in presence of target analyte glyphosphate | Zhang and co-workers [35] |

| | | | | | |
|---|---|--|------------------|---|--------------------------|
| HRP | Thioglycolic acid capped CdS QDs | Poly(diallyldimethylammonium chloride) Polyclonal goat antimouse IgG (Ab ₂), Mouse IgG (Ag), Polyclonal goat antimouse IgG (labeled with HRP, Ab ₂) Benzo-4-chlorohexadienone | Indium tin oxide | Detectable photocurrent with intensity reversed proportional to concentration of target analyte mouse IgG (Ag). | Zhao and co-workers [36] |
| HRP (In biconjugation with antibodies and Au nanoparticles) | Poly-(diallyldimethylammonium chloride)-graphene-CdSe QDs | Chitosan | Glassy carbon | Electrochemiluminiscent peak at -1.2 V with intensity proportional to the logarithm of the concentration of target analyte Hg ²⁺ . | Cai and co-workers [37] |
| Sulfite oxidase | Polyethylenimine entrapped CdS nanoparticles | 3,3'-Dithiodipropionic acid di(N-hydroxysuccinimide ester) self-assembled monolayer crosslinked with succinimide active ester and branched polyethyleneimine | Indium tin oxide | An increase in oxidation current starting at -250 mV in presence of target analyte sulfite | Zeng and co-workers [33] |

Table 2.1 A summary of the different enzymes, QDs and electrode types used for construction of electrochemical biosensors.



2.2 Redox center of Heme-containing Enzymes

Heme enzymes use the heme group as a cofactor. Heme consists of a ferrous iron (Fe^{II}) in the center of a porphyrin molecule (Figure 2.1). [38]

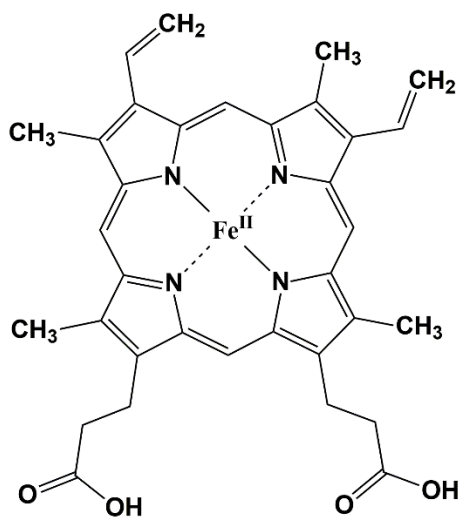


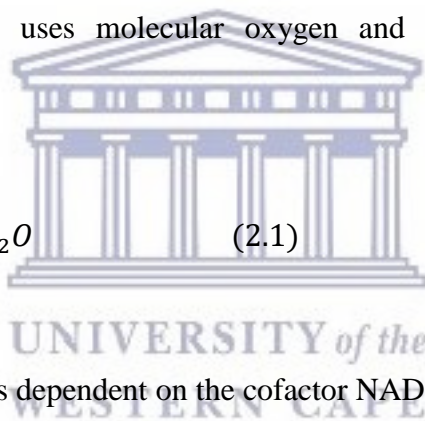
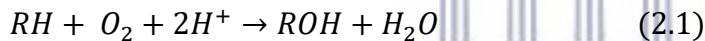
Figure 2.1 The molecular structure of heme.

The amount of enzymes falling under this category is extensive with peroxidases being the most studied in the field. The enzymes can catalyze both reductive and oxidative reactions. Heme enzyme oxidants can thereafter be divided into two categories: oxygenases (that use O_2 to oxidize substrates) and peroxidases (that use H_2O_2 for oxidizing substrates), with the later mentioned being the most usual oxidant since O_2 is not a reactive molecule. The role of the heme group for heme oxygenases is to overcome the kinetic barrier present for reactions between O_2 and the majority of biological molecules. In the case of the peroxidases, the reaction between H_2O_2 and transition metals generate toxic hydroxyl radicals which damages the enzyme. Thus, the active site of the heme enzyme is designed to reduce the formation of these destructive hydroxyl radicals by ensuring domination of an alternative pathway, forming H_2O and a naked O atom instead.[38] Since CYPs and HRP are the most used heme enzymes for quantum dot electrochemical biosensors, the following subchapters will focus on the reaction mechanism of these enzymes.

2.2.1 Monooxygenation reaction of CYP enzymes

The use of CYPs as a biorecognition element has shown good potential thanks to their high specificity in combination with their ability to metabolize a broad range of substances. Endogenous substances such as fatty acids, steroids and prostaglandins acts as CYP substrates. The CYP substrates also includes drugs and toxins. At the same time, CYPs has the ability to metabolize endogenous substances with high specificity, for instance the conversion of steroid hormones. This allows good possibilities for distinction of specific substrates. [16–18,22,39]

The active site of the cytochrome P450 enzyme is the iron containing heme group. Through substrate binding to the active site, the enzyme metabolizes a variety of reactions in vivo such as hydroxylation, epoxidation, N-,S- and O-demethylation. Through these reaction, the CYPs participates in the phase I metabolism of drugs and xenobiotics, allowing second-phase metabolism and excretion from the body through the urine. [21,40] Substrate hydroxylation under CYP catalysis refers to the hydroxylation of a substrate RH by inserting an oxygen atom to form ROH. The reaction uses molecular oxygen and the overall reaction follows Equation 2.1.[22,39]



In vivo, the reaction of CYPs is dependent on the cofactor NAD(P)H that works as an electron donor. In addition, cytochrome P450 reductase (CPR) is needed for transfer of the electrons from NAD(P)H to the CYP enzyme.[21,22] A schematic illustration of the cytochrome P450 catalytic cycle is showed in Figure 2.2.

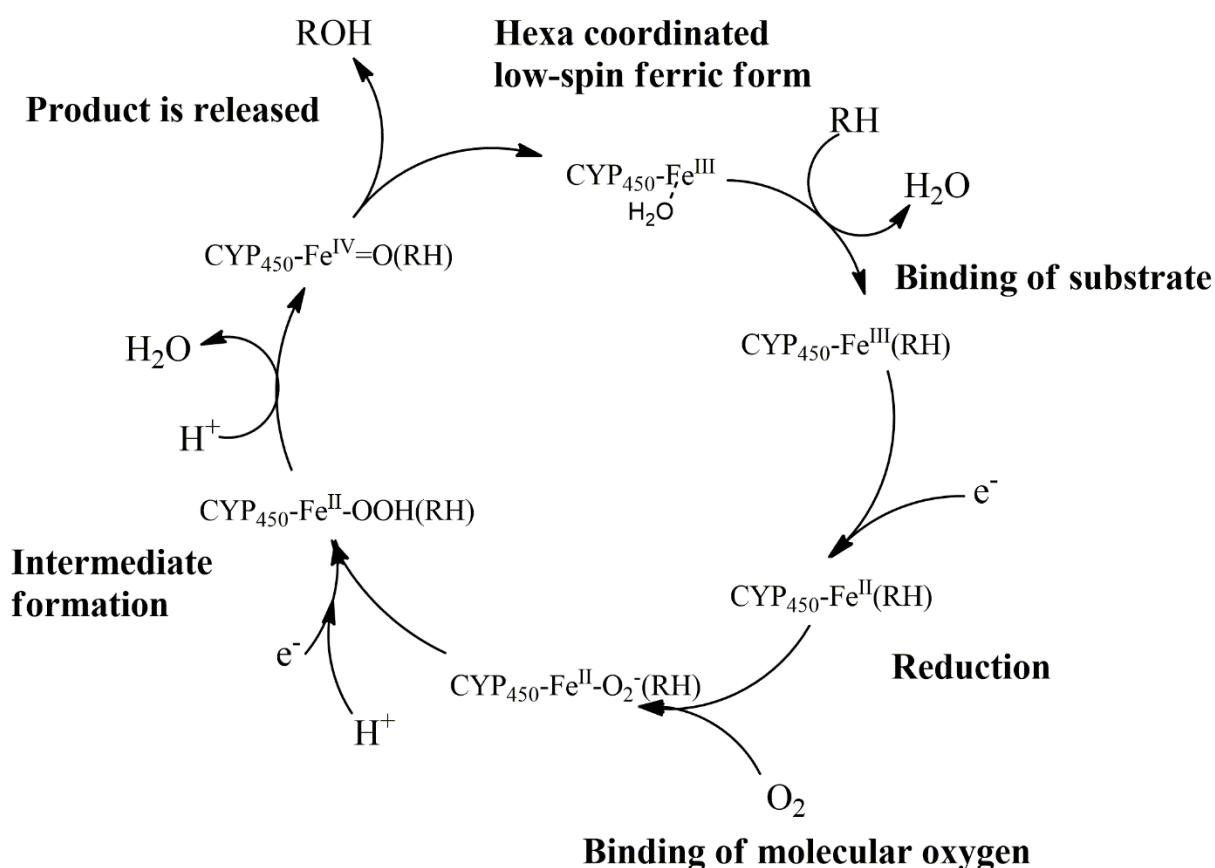


Figure 2.2 The catalytic cycle of cytochrome P450 enzymes for substrate hydroxylation.

The most accepted model for the reaction mechanism of substrate hydroxylation by CYP involves 7 steps. However, the mechanism involves intermediate steps that are still not fully understood. Before binding of substrate for reaction initiation, the CYP is in hexa-coordinated, low-spin ferric form with water serving as the sixth ligand. The cycle starts with the substrate binding to the active site of the enzyme, causing exclusion of the water ligand. This induces a shift to a 5-coordinate high-spin state. In the second step, a positive shift of the redox potential occurs as a consequence of the decreased polarity of the enzyme. This positive shift enables the transfer from one electron from a redox partner to reduce the enzyme from the ferric (Fe^{III}) to the ferrous (Fe^{II}) state. Thirdly, molecular oxygen is bound to the ferrous enzyme to form the $\text{Fe}^{\text{II}}\text{-O}_2$ complex. In step four, an iron-hydroperoxo ($\text{Fe}^{\text{III}}\text{-OOH}$) intermediate is formed by transfer of an electron followed by a proton to the $\text{Fe}^{\text{II}}\text{-O}_2$ complex. In step five, the O-O bond is cleaved. A water molecule and an iron-oxo ferryl ($\text{Fe}^{\text{V}}=\text{O}$) intermediate is released. In the sixth step, the iron-oxo intermediate extracts one hydrogen atom from the substrate, reducing the intermediate to a ferryl species ($\text{Fe}^{\text{IV}}\text{-OH}$) and forming a substrate radical (R^{\cdot}). This is

followed by a radical recombination to form the enzyme-product complex. Alternatively, the complex is formed without the radical forming intermediate step. In the final step, the product ROH is released and the initial low-spin ferric enzyme is reformed. [22,39,41,42]

By immobilizing CYPs on an electrode surface it is possible to eliminate the need for NAD(P)H and CPR as a part of the metabolizing reaction. In this situation, the electrode will serve as the electron donor. When applying a voltage to the electrode with the immobilized CYP enzyme in presence of a CYP substrate, a redox reaction will be triggered. Thus, a current will be generated which will give a direct indication of CYP dependent electrocatalysis. [21,39]

2.2.2 Mechanism of HRP Catalysis

Peroxidases uses H_2O_2 catalyze the one-electron oxidation of a great variation of oxidizable xenobiotics. The overall reaction of oxidation of xenobiotics (XOH) involves the steps described in Equation 2.2 to Equation 2.4.[23] The peroxidase catalytic cycle for xenobiotics oxidation is illustrated in Figure 2.3.

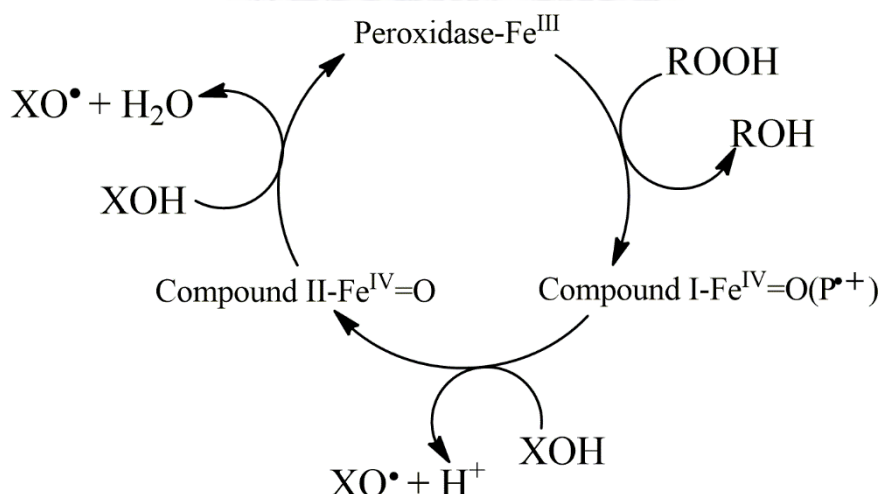
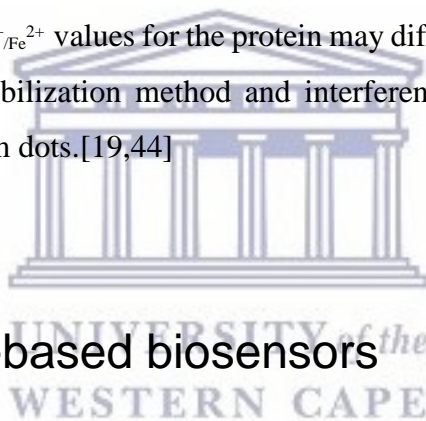


Figure 2.3 Peroxidases catalytic cycle for oxidation of xenobiotics.

In the first step, peroxidases catalyze the oxidation of hydroperoxides that loses two electrons. This causes the formation of the corresponding alcohol of the hydroperoxide and compound I, which is an intermediate with distinct spectral characteristics that are different from the resting enzyme. Studies suggest that in the forming of compound I, an electron is transferred from the iron and a second from the porphyrin ring in the heme group to form a porphyrin π -cation ($P^{\bullet+}$) radical. In some peroxidases, one of the electrons are transferred from an amino acid sidechain rather than the porphyrin group. In the second step, compound I is reduced to compound II by receiving an electron from a substrate molecule which reduces the porphyrin π -cation radical. Compound II is a well-defined $Fe^{IV}=O$ specie. In the last step, a substrate molecule reduces Fe^{IV} back to Fe^{II} in the heme prosthetic group and the resting enzyme is reformed.[23,38,43]

Horseshoe peroxidase is a plant based peroxidase and the electrochemical behavior of this enzyme has been thoroughly studied. The electrochemistry observed when immobilizing HRP on an electrode surface is due to Fe^{III}/Fe^{II} electron transfer reaction occurring on the heme group in the active site.[44] The $E^{\circ}_{Fe^{3+}/Fe^{2+}}$ values for the protein may differ depending on experimental conditions such as pH, immobilization method and interference of other electrode surface modifications such as quantum dots.[19,44]



2.3 Quantum dots-based biosensors

2.3.1 Biocompatible quantum dots

Quantum dots (QDs) are semi-conductive particles with size normally varying from 2-10 nm in diameter and are defined as particles with physical dimension smaller than the exciton Bohr radius [45,46]. Their good photo luminescent and electrochemical properties enables a broad spectra of applications such as light-emitting diodes (LED), photovoltaics, bioimaging and medical diagnostics. [38,47,48]

The optical properties of QDs is due to the excitement of electrons from the valance band to the conduction band. The difference in energy between these two bands are known as the band gap (E_{gap}). Photons are absorbed by semiconductor QDs if the excitation energy exceeds the band gap. When an electron is excited to a higher energy level in the conduction band, a hole is left in the valance band. The electron and its associated hole can be hold together by electrostatic attraction and forms an exciton. The distance between the electron and its hole in an exciton is

called the “Bohr radius of the exciton” and is typically a few nanometers in size. An exciton is free to move in every direction when formed in a bulk material. However, in the situation of a QD, the diameter is reduced to the same order of magnitude as the Bohr radius and the exciton cannot move freely. When the QDs diameter is smaller than the Bohr radius of the exciton, quantum confinement occurs. This causes a transition from continuous to discrete energy levels. The energy levels of the valence and conduction band, within the QD, becomes quantized and the energy values can be directly related to the particle size. The unique optical properties of the QDs is accredited to this quantum confinement effect. [49,50]

One of the most interesting of the QD properties is the possibility to tune their properties by changing the particle size. Especially the wavelength of fluorescence emission.[51] With different absorption techniques it is possible to study the relation between QD particle size and bandgap values. The absorption band shifts to lower energies as the size of the QDs increases. With diameters below the Bohr radius the absorption spectrum shows a fine structure, which is due to the discrete energy levels [49,50]. The lowest detectable peak in the absorption spectra is called “quantum-confinement peak” and illustrates the lowest excited energy state of the semi-conductive nanoparticle. [46]

Surface modifications are often required in order to improve the water solubility of the QDs and obtain biocompatibility. Commonly, the surface of the QD is modified with either polymers, thiol compounds, mercaptopropionic acid compounds or organic groups.[52] Such modifications makes it possible to further link the QDs to other biological molecules such as antibodies, aptamers and enzymes. Through this, the QDs can be further applied for biological, medicinal and biodetecting purposes.[10,33,52–56]

2.3.2 Types of QDs biosensors

The application of QDs in biosensors has been explored in numerous studies. Through covalent attachment of different biorecognition molecules e.g. DNA strands, cells and enzymes QDs can make part of highly sensitive biosensors. The sensors applications ranges from DNA sensing for clinical diagnostics to detection and discrimination of genetically modifies organisms.[57–59] Likewise, QDs in enzyme based electrochemical biosensors has promising possibilities as a biological detection tool. [20,60,61] Different enzymes has been used for these applications. In a recent study Han and co-workers immobilized the enzyme tyrosinase to a CdS quantum dot/chitosan nanocomposite matrix. The CdS QD/Citosane/Tyrosinase mixture was then spread

on a glassy carbon electrode. This created a sensor with high sensitivity to the detection of catechol and a low detection limit of 0.3 nM at a signal-to-noise ratio of 3. [61] More enzymes have been used for electrochemical biosensing utilizing quantum dots, for example glucose dehydrogenase and acetylcholinesterase, with the heme based enzymes representing a big part. With the aim of enhancing current intensity without compromising the stability and biological activity of the enzyme.[10,19,20,28–32][59,62]

2.4 Biosensing with QDs-CYP electrodes

2.4.1 Electrochemical sensors

Many different techniques have been reviewed regarding immobilizing enzymes on the electrode surface, creating a bioelectrode. The use of self-assembled monolayers (SAMs) and nanoparticles has been utilized to fulfill this task. A popular alternative is gold nanoparticles due to its good electron mediating abilities.[21,63,64] Also different forms of graphene nanocomposites have been explored as a part of a CYP electrochemical biosensor. [65,66] The use of different types of QDs as electron mediators in a cytochrome P450 based electrochemical biosensor has been explored in 4 recently published articles. Ndangili and co-workers [10] made a biosensor construct using 3-mercaptopropionic acid (3MPA) capped ZnSe quantum dots conjugated to a gold electrode previously modified with self-assembled L-cysteamine (Cys). Cytochrome P450 3A4 was then conjugated onto the modified electrode to create the final Au/Cys/3MPA-ZnSe/CYP3A4 biotransducer. This was used for detection of 17 β -estradiol (E2) which is an endocrine disrupting compound. The catalytic response of the biosensor was studied in aerobic conditions using cyclic voltammetry (CV) and square wave voltammetry (SWV). The studies were carried out in phosphate buffer of pH 7.4 and with different concentrations of E2. In the presence of 0.55 μ M of E2, a reduction peak was observed at -200 mV. The results were compared to the catalytic response of the biotransducer in absence of quantum dots (Au/Cys/CYP3A4) with and without E2 in the solution. Figure 2.4 shows cyclic voltammograms of these studies carried out at 40 mVs⁻¹ scan rate.[10]

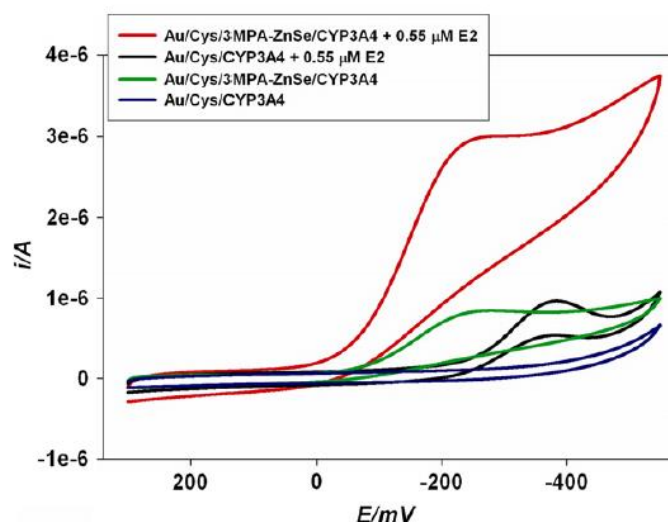


Figure 2.4 Cyclic voltammograms of Au/Cys/CYP3A4, and Au/Cys/3MPA-ZnSe/CYP3A4 with 0.55 μM of E2 (black and red respectively) and without E2 (blue and green), in phosphate buffer of pH 7.4 at 40 mVs^{-1} . (Reprinted from Ndangili and co-workers[10] with permission)

The catalytic response of the Au/Cys/3MPA-ZnSe/CYP3A4 was compared to the response of Au/Cys/CYP3A4 in presence of E2, where a weak reduction peak could be observed at -382 mV. This potential shift was attributed to the quantum dots ability to confine electrons in three dimensions. Thus, the activation energy of the reaction was lowered due to enhancement of the electrochemical reaction. The Michaelis-Menten constant (K_M^{app}) was calculated to 0.15 mM. The authors discuss the low value of K_M^{app} as an indication that the 3MPA-ZnSe QDs were both biocompatible and provided a stable microenvironment for immobilization of CYP3A4. The detection limit for the sensor was determined to 1.03×10^{-10} M which is in the same order of magnitude as the upper limit for naturally occurring levels of E2 measured in bovine plasma or serum (1.47×10^{-10} M). Thus, the biotransducer could be applicable for E2 detection in bovine serum. When storing the transducer for 2 weeks the sensor lost 46.23 % (standard deviation 0.15; n=8) of its previous response. Thus, this electrochemical biosensor is rather considered a “single use biotransducer”.[10]

In another article, Nxusani and co-workers 2012 [30], developed an electrochemical biosensor for detection of 17- α -ethinyl estradiol (17EE). The biosensor construct consisted of 3MPA capped Ga_2Se_3 quantum dots deposited on an L-cysteine modified gold electrode and coupled to genetically engineered CYP3A4. The biosensor response was likewise investigated using CV and SWV in aerobic conditions in 0.1 M phosphate buffer saline (PBS) with pH 7.4. Upon addition of 17EE into the PBS solution, an irreversible reduction peak occurred at a potential of -220 mV. The reduction peak current at a potential of $E_p = -220$ mV increased with increasing concentration of 17EE. The biosensor could detect concentrations of 17EE down to 15×10^{-9} M.

The response of the Au/L-cystein/3MPA- Ga₂Se₃/CYP3A4 biosensor construct was compared to the response of the bare gold electrode, the L-cystein modified electrode and the biosensor construct in absence of the CYP3A4 enzyme (Au/L-cystein/3MPA- Ga₂Se₃). Only Au/L-cystein/3MPA-Ga₂Se₃ gave a slight response in presence of 17EE. Though, there were no control experiments for the response of the biosensor construct without the 3MPA-Ga₂Se₃ quantum dots, which makes it difficult to infer the exact effect of the QDs to the final biosensor construct. [30]

2.4.2 Photoelectrochemical Sensors

A photoelectrochemical sensor was developed in the work presented by Xu and co-workers 2014 [31], with the purpose of creating a light driven drug metabolism system by utilizing the optical properties of quantum dots. In this construct, CdTe QDs functionalized with thioglycolic acid (TGA) were linked to the amino groups of 3-aminopropyltriethoxysilane (APTES) immobilized on an indium tin oxide (ITO) electrode. Thereafter, CYP2C9 enzyme was coupled to the TGA functionalized CdTe QDs by covalent binding of the amino groups of the protein to the carboxylic groups of the TGA.[31] Characterization of photoelectric properties of the QD film, using illumination by a Xe lamp, showed a detectable photocurrent. This is contrary to the simple ITO/APTES electrode under the same applied potential. Thus, the obtained photocurrent was attributed to the generation of electron-hole pair and electron transfer between the TGA-CdTe QDs and the electrode. When CYP2C9 was added to the electrode, there was an increase in cathodic photocurrent upon illumination. The intensity of photocurrent increased with increasing amount of CYP2C9 in relationship to the TGA-CdTe QDs. This indicated that CYP2C9 enzyme accelerated the electron transfer from QDs to CYP2C9. The TGA-CdTe QDs, fixed on the electrode surface, worked as a light-controlled switch for the electron transfer to CYP2C9 in the oxidized state.[31] Consequently, the electrons from the conduction band of the QDs were trapped by the enzyme, whilst the electron holes (generated in the valence band) were being filled through electron transfer from the electrode. Furthermore, the authors evaluated the light-driven drug metabolism on the system, using tolbutamide as the target substrate. The photocurrent increased with increasing concentration of tolbutamide at the applied potential of -200 mV. The photocurrent response plotted against the concentrations of the substrate showed a hyperbolic behavior that could be fitted with Michaelis-Menten equation. K_M^{app} was calculated to be $76.28 \pm 3.59 \mu\text{M}$, which was in agreement with other reports of hydroxylation of tolbutamide with K_M^{app} ranging from 60 to 400 μM . Similar results

were obtained for inhibition studies using sulfaphenoazole as a strong competitive inhibitor for CYP2C9. The photocurrent response of tolbutamide hydroxylation decreased with increasing concentrations of sulfaphenoazole at -200 mV. The authors argue that: the results suggest that the quantum dot functionalized electrode provides a stable bioenvironment for the immobilized enzyme therefore maintaining its biological activity.[31]

A similar photoelectrochemical construct was made by Qian and co-workers 2014.[32] Likewise in this work, the authors used an amino functionalized indium tin oxide electrode. CdTe quantum dots functionalized with 3-mercaptopropionic acid were immobilized on the surface followed by cytochrome P450 2D6 enzyme. This resulted in a photoelectrochemical platform with possibilities of *in-situ* (in reaction) monitoring of light-driven drug metabolism. The CYP2D6/CdTe/NH₂-ITO electrode was studied in PBS pH 7.4. When illuminating the system with a white light source, cathodic photocurrent was observed at applied potentials more negative than 100 mV. Whereas anodic photocurrent was observed at more positive potentials. The induced photocurrent was attributed to the generation of electron-hole pair and the electron transfer between CdTe QDs and the electrode, with the same mechanism as described in the article by Xu and co-workers[31] To investigate the light-driven drug metabolism of the system, tramadol was chosen as substrate. An increase in cathodic photocurrent was observed at applied potential of -200 mV (vs. SCE) upon addition of tramadol to the PBS, in contrast to the control experiment in absence of CYP2D6 were no increase in photocurrent was detected. This increase in photocurrent as a function of increased concentration followed Michaelis-Menten kinetics and K_M^{app} was calculated to be 1.35 μ M, which is lower than the reported value for tramadol metabolized by human microsomes (210 μ M) and for in-solution CYP2D6-dependent tramadol O-demethylation using NADPH as the electron donor (26.2 μ M). Furthermore, inhibition experiments were carried out using quinidine as CYP2D6 inhibitor. The photocurrent decreased gradually with increasing amount of quinidine added to the PBS solution containing a constant tramadol concentration of 2.7 μ M. The results suggested good retained metabolic activity of the CYP2D6 enzyme. The aim of the construct was to create a photoelectrochemical platform with the concept of light-driven drug metabolism for metabolic studies. However, the authors also argue about the potential of utilizing this construct for investigation of drug-drug and drug-enzyme interaction and development of new drugs.[32]

2.5 HRP-QDs bioelectrodes

Horseshoe peroxidase is commonly used in construction of electrochemical biosensors.[27,67–69] However, problems as denaturation can arise when the enzyme is in direct contact with the electrode surface. At the same time, electron transfer between the HRP and electrode is difficult because of the active center being positioned deeply into the three-dimensional structure of the enzyme. Different materials such as self-assembled monolayers, surfactants and nanoparticles have been explored as an electron mediator between the enzyme and electrode.[29,70–72] The use of quantum dots in combination with HRP in electrochemical biosensors has been explored in different varieties.

2.5.1 Peroxide sensors

In 2008, Wang and co-workers [29] reported a H_2O_2 biosensor based on HRP using lipophilic CdSe/ZnS QDs incorporated in a glassy carbon electrode (GCE). The biosensor was characterized using CV in 0.1 M PBS pH 7.0. The authors investigated different methods to incorporate the CdSe/ZnS QDs onto the electrode surface. When the QDs were immobilized using vapor depositions a clear well-defined quasi-reversible peak was observed for the QD/HRP electrode. This was in contrast to when the QDs were directly dropped on the electrode surface. The peak was attributed to the electrochemical activity of the HRP enzyme. The authors discuss that the slow vapor deposition process of the QDs may have contributed to a favorable orientation of the HRP when immobilized on the surface. Thus, the QDs causes enhancement of the electron transfer between the HRP and the enzyme. The oxidation and reduction peaks were observed between -177 and -242 mV respectively, resulting in the formal potential of $E^{\circ'} = -210$ mV. This is close to the -220 mV of the native HRP in solution. Therefore the authors argue that the HRP enzyme has maintained its native structure when immobilized on the CdSe/ZnS QD vapor deposited electrode. When performing CV in presence of H_2O_2 the cathodic peak current intensity increased with increasing concentration of target substrate. The same result was obtained when measuring steady-state current at the potential of -400 mV. From this K_M^{app} was calculated to be 0.152 mM, implying high catalytic activity of the immobilized enzyme. The biosensor construct has a low detection limit of 2.85×10^{-7} M and retained 89% of its initial sensitivity after 1 week of storing. Showing that the QDs not only promoted the electron transfer between HRP and the electrode but also provided a stable microenvironment for the enzyme. However, this result were only seen when the QDs were

immobilized by vapor deposition. Thus, the authors argue that the electrochemical behavior of the enzyme relies on the way the QDs were immobilized on the electrode surface.[29]

Another H₂O₂ detection tool was reported by Yang and co-workers, 2010. [34] In this article a photoelectrochemical H₂O₂ biosensor was developed using HRP together with CdSe QDs in a mesoporous (MS) silica template. The CdSe/MS nanocomposites were immersed on an indium tin oxide sheet. Thereafter, the HRP was immobilized on the CdSe/MS film. The amperometric response of the biosensor to different concentrations of H₂O₂ was investigated in PBS pH 6.8, at applied potential 0.2 V, under UV illumination. The response current was linear to the concentration of H₂O₂ within the range of 0.8-9.8 μM. From the concentration-current relationship, the Michaelis-Menten constant was calculated to 2.72 mM. The HRP/CdSe/MS electrode showed stronger reduction current under UV illumination than in the dark. The authors argue that the results showed that the immobilized HRP retained its catalytic activity on the CdSe/MS immobilized electrode. Further, the CdSe/MS also enhanced the catalytic reduction of H₂O₂. The increased current response under UV illumination was attributed to generation of electron-hole pair in the QDs. Thus, facilitating the reduction processes between the HRP and the electrode.[34]

The sensitivity towards H₂O₂ within the QD based HRP electrochemical biosensors was massively improved in a work published by Zhiguo and co-workers 2011[20]. In this article, the authors created a hydrogen H₂O₂ capable of detecting the substrate at 3.2*10⁻¹¹ M. The biosensor had a wide calibration range of from 1*10⁻¹⁰ M to 1.2*10⁻⁸ M and with a stability of 20 weeks. The constructs were made by sequential covering of a gold electrode with graphene-gold nanocomposite (G-AuNP), CdTe-CdS core-shell quantum dots (CdTe-CdS), gold nanoparticles (AuNPs) and horseradish peroxidase to create a HRP/AuNPs/CdTe-CdS/G-AuNP/GE construct. The biosensor performance towards H₂O₂ detection was investigated in PBS pH 7.0 using CV and differential pulse voltammetry. The authors credited the high sensitivity of the biosensor to the surface architecture of the electrode. The CdTe-CdS, located in the middle, acted as an electron transfer channel between the G-AuNP and AuNPs. Thanks to the CdTe-CdS QDs ability to carry and transfer charge ultrafast, the electron transfer was rapid and efficient. Furthermore, the authors argue that certain arrangements of the CB and VB of the CdTe-CdS QDs created a favoring electron transfer between the QDs and AuNPs or G-AuNP layer.[20]

The most recently published H₂O₂ electrochemical biosensor utilizing QDs in combination with HRP was reported by Muthurasu and co-workers 2014.[19] The construct was made of

graphene quantum dots (GQDs) conjugated with HRP and immobilized on a glassy carbon electrode (GCE). The biosensor response towards H_2O_2 was investigated using CV and chronoamperometry (CA) in PBS pH 7.0. A redox peak corresponding to $\text{Fe}^{\text{III}}/\text{Fe}^{\text{II}}$ redox reaction of the heme group could be observed. Amperometric studies were performed at the applied potential of -445 mV. The results were compared to the response of the bare GCE and GCE with only GQDs on the surface. The reduction current intensity was dramatically increased when introducing the HRP enzyme on the electrode surface. The authors argue that the GQDs facilitate the electron transport as well as provides possibility for favorable orientation of HRP on the electrode surface. The sensor could detect concentrations down to 530.85 nM, which fell within the range of other reported H_2O_2 biosensors. The stability of the biosensor was quite good with a decrease of 97 % of the reduction current after 3 months. Overall, the authors demonstrated a simple construct of a H_2O_2 biosensor with a fair detection limit and good stability.[19]

The use of GQDs in HRP electrochemical biosensors was also explored by Hu and co-workers 2015. [28] An electrochemical biosensor for detection of miRNA was developed using a double-stranded DNA structure. The biosensor consisted of a gold electrode functionalized with different DNA probes. Thereafter, graphene quantum dots were attached to the DNA strands. These GQDs were then used as a platform for noncovalent attachment of HRP to the modified electrode surface. The reaction used H_2O_2 mediated oxidation of 3,3',5,5'-tetramethylbenzidine to amplify the current signal for detection of miRNA-155. The biosensor response was investigated with amperometric detection in 0.01 M PBS pH 7.4 in different concentrations of miRNA. The amperometric current increased with the concentration of miRNA within the impressive range of 1 fM to 100 pM. The sensor showed selectivity towards miRNA-155 compared to miRNA-21 and DNA at 10 pM respectively. Furthermore, it retained 85% of its initial response to 1 pM RNA after one week storing. The authors attributed the good selectivity and stability of the biosensor to the high surface to volume ratio of GQDs and their strong interaction with the enzyme.[28]

2.5.2 Other HRP analytes

The use of HRP to detect other analytes, in alternative to the well explored H_2O_2 as a target substrate, was also investigated by Zhang and co-workers 2015.[35] In this paper, an electrochemiluminescent (ECL) sensor was constructed using ZnS QDs on ordered mesoporous carbon (OMS) together with HRP on a glassy carbon electrode. The aim of the construct was

the detection of glyphosate (Gly). In this article, QDs were synthesized directly on the electrode surface by absorption of Zn^{2+} ions on an OMS and chitosan coated electrode. Thereafter, HRP was introduced together with H_2O_2 and $S_2O_3^{2-}$ to generate H_2S , which bound to the Zn^{2+} and generated ZnS QDs. The ECL response of the system was significantly lower in absence of HRP. The authors argue that the presence of the HRP accelerated the reaction to form the ZnS QDs on the electrode surface. In presence of the target analyte Gly, the ECL signal decreased dramatically. This was due to the fact that Gly inhibited the HRP activity and thus the formation on ZnS QDs. The ECL response of the biosensor decreased proportionally to increasing concentration of Gly. The Michaelis-Menten constant was calculated to be 0.56 mM, by varying the H_2O_2 concentration. Whereas inhibition studies were carried out by varying the Gly concentration in the range of 0.1 nM to 10 mM. Moreover, the sensor showed remarkable sensitivity and could distinguish different Gly concentrations in vegetable juice.[35]

In other studies, HRP and QDs has been combined with antibodies for detection of different substrates. In an article by Zhao and co-workers 2011 [36], a photoelectrochemical immunosensor was created using TGA capped CdS QDs. The QDs were applied for their photoelectrochemical properties rather than enzyme immobilization. The base of the biosensor consisted of a poly(diallyldimethylammonium chloride) (PDDA) ITO electrodes functionalized with CdS QDs. On these electrodes polyclonal goat antimouse IgG (Ab_1) was immobilized. Thereafter, different concentrations of the target antigen analyte mouse IgG (Ag) was dropped on the electrode surface of several modified electrodes. This was followed by incubation with HRP-labeled polyclonal goat antimouse IgG (Ab_2) to create the final CdS- Ab_1 -Ag- Ab_2 -HRP modified electrode. Finally, the electrode was insulated with benzo-4-chlorohexadienone by HRP accelerated oxidation of 4-chloro-1-naphtol. The photoelectrochemical immunoassay of the electrodes, containing different Ag concentrations, was carried out in 0.1 M PBS pH 7.4 containing 0.1 M ascorbic acid. The applied potential was 0 V and the excitation wavelength was 410 nm. The photocurrent response decreased with increasing Ag concentration. The authors suggest that the decrease in photocurrent is due to three factors. Firstly, the formation of Ab_1 -Ag- Ab_2 -HRP immunocomplex provided a steric hindrance and lower the diffusion of electron donor molecules to the CdS QDs layer. Secondly, the formation of the isolating benzo-4-chlorohexadieone layer was accelerated by HRP. The layer crated a barrier for electron transfer at the electrode surface. Again, the CdS QD interaction with the electron donor was suppressed, which reduced the generation of photocurrent. Lastly, HRP absorbs light at 410 nm as well. Thus, the enzyme acted as a competitor for light absorption hence affecting the

photocurrent response of the QD modified electrode. From the biosensor assessment the detection limit was found to be 0.5 pg mL^{-1} . After over 2 weeks of storage, the photocurrent response of the detection of Ag was unchanged, indicating good stability. The biosensor could also distinguish different Ag concentration in real samples of mouse serum, indicating the possibility of practical application for the immunoassay.[36]

In a more recent study, Cai and co-workers 2015 [37], likewise utilized antibodies together with HRP and QD to create an ECL biosensor for the detection of Hg^{2+} . PDDA functionalized graphene (PDDA-GN) was conjugated to TGA modified CdSe QDs and immobilized on a glassy carbon electrode surface. The PDDA-GN-CdSe layer was covered with a chitosan layer and coated with specific antigen. Separately, HRP was bioconjugated with monoclonal antibodies (Ab) and labeled with AuNPs creating Ab-AuNPs-HRP composites. The Ab-AuNPs-HRP composites were introduced to the biosensor system in an incubation solution together with the target analyte Hg^{2+} . The ECL response of the biosensor was investigated using CV with Ag/AgCl reference electrode. Different concentrations of Hg^{2+} was presented in oxygen-saturated Tris-HCl buffer pH 9.0 containing 0.1 KNO_3 and 1.5 mM o-phenylenediamine (OPD). Reductions peaks were observed at -0.72 V and -0.92 V . The -0.72 V reduction peak was attributed to the reduction of dissolved oxygen around the electrode surface to create H_2O_2 . The self-produced H_2O_2 then reacted with electron injected CdSe QDs to create excited QDs at -0.92 V . Subsequently, an emission peak at -1.2 V could be observed. However, in the presence of HRP catalysis, OPD reacted with H_2O_2 . The consumption of H_2O_2 thus quenched the ECL response. The effect was enhanced upon addition of HRP on the electrode surface. In presence of different Hg^{2+} concentrations, the Hg^{2+} competed with the coating antigen for binding of the Ab in the Ab-AuNPs-HRP composites. Higher Hg^{2+} concentration would result in less available Ab-AuNPs-HRP composites binding to the modified electrode surface and their less quenching of the ECL response. Consequently, the ECL response increased with increasing Hg^{2+} concentration. From these studies, the lower limit of detection was calculated to be 0.06 ng mL^{-1} . Moreover, the biosensor showed good selectivity in presence of other metal ions and showed acceptable recovery when applied to waste water samples.[37]

2.6 Other heme-enzyme biosensors

In addition to the CYPs and HRP based QD electrochemical biosensors, the heme containing molybdoenzyme human sulfite oxidase (hSO) has also been used for such constructs. Zeng and co-workers 2015 [33], reported a photoelectrochemical biosensor utilizing hSO for detection of sulfite. The hSO enzyme was immobilized on an ITO electrode functionalized with polyethylenimine-entrapped CdS QDs. The ITO electrode had firstly been covered with a self-assembled monolayer consisting of 3,3'-Dithiopropionic acid di(N-hydroxysuccinimide ester). The biosensor system was investigated using CV in 750 mM Tris-acetate buffer pH 8.4 in the presence of the target substrate sulfite. An increase in catalytic current can be detected with starting point at -250 mV (vs. Ag/Ag Cl reference electrode). As opposed to the system in absence of sulfite. At this pH, K_M^{app} was calculated to be 20 μ M. Even though it is higher than the reported value for hSO, the authors argue that the sulfite has sufficiently fast access to the active site of the enzyme. The effect of light illumination of the biotransducer was also investigated under aerobic conditions. The solution was illuminated with 470 nm light and the applied potential was 0 V. No photocurrent was observed for the enzyme free system. However, when hSO was present on the ITO/CdS QDs a catalytic photocurrent response could be detected in presence of the target analyte. In this article, the authors utilized both the photoelectrochemical properties of the QDs as well as their ability to provide a biologically stable microenvironment for the hSO enzyme.[33]



2.7 Conclusions

The use of QDs in combination with heme enzymes in electrochemical biosensors has been explored in many varieties. The role of the QDs differs depending on the nature of the sensor. In photoelectrochemical and electrochemiluminescent biosensors, the QDs provides a key element for the structure. This is attributed to the ability to absorb and emit light with the formation or recombination of electron-hole pairs. Whereas in amperometric devices the QDs are rather utilized for enzyme immobilization and signal enhancement. In the construct presented the QDs has shown to provide stable microenvironment for the immobilized enzymes with retention of their biological activities. In addition, many have presented remarkable sensitivity and selectivity indicating possibilities for practical applications. Thus, it has been shown that QDs are a promising alternative as an electron mediator between the electrode and enzyme in electrochemical biosensors.

In some cases there are still many combinations of QD and heme enzymes to be explored for further refinement of sensitivity, selectivity and stability. In addition, there are yet many unexplored target analytes that could be detected with such electrochemical constructs. All in all, electrochemical biosensors using QDs provides a good alternative to the detection methods used today thanks to their high sensitivity, fast response and facile operation.



2.8 References

- [1] H. Wang, Y. Zhang, H. Yu, D. Wu, H. Ma, H. Li, B. Du, Q. Wei, Label-free electrochemical immunosensor for prostate-specific antigen based on silver hybridized mesoporous silica nanoparticles, *Anal. Biochem.* 434 (2013) 123–127. doi:10.1016/j.ab.2012.11.012.
- [2] M.M.P.S. Neves, M.B. González-García, C. Delerue-Matos, A. Costa-García, Multiplexed electrochemical immunosensor for detection of celiac disease serological markers, *Sensors Actuators B Chem.* 187 (2013) 33–39. doi:10.1016/j.snb.2012.09.019.
- [3] N. Widmer, C. Bardin, E. Chatelut, A. Paci, G. Veal, A. Astier, J. Beijnen, D. Leve, Review of therapeutic drug monitoring of anticancer drugs part two - Targeted therapies, *J. Cancer.* (2020) 2020–2036.
- [4] P. Singh, S.K. Pandey, J. Singh, S. Srivastava, S. Sachan, S.K. Singh, Biomedical Perspective of Electrochemical Nanobiosensor, *Nano-Micro Lett.* 8 (2016) 193–203. doi:10.1007/s40820-015-0077-x.
- [5] A. Haouala, B. Zanolari, B. Rochat, M. Montemurro, K. Zaman, M.A. Duchosal, H.B. Ris, S. Leyvraz, N. Widmer, L.A. Decosterd, Therapeutic Drug Monitoring of the new targeted anticancer agents imatinib, nilotinib, dasatinib, sunitinib, sorafenib and lapatinib by LC tandem mass spectrometry, *J. Chromatogr. B Anal. Technol. Biomed. Life Sci.* 877 (2009) 1982–1996. doi:10.1016/j.jchromb.2009.04.045.
- [6] S. Bouchet, E. Chauzit, D. Ducint, N. Castaing, M. Canal-Raffin, N. Moore, K. Titier, M. Molimard, Simultaneous determination of nine tyrosine kinase inhibitors by 96-well solid-phase extraction and ultra performance LC/MS-MS, *Clin. Chim. Acta.* 412 (2011) 1060–1067. doi:10.1016/j.cca.2011.02.023.
- [7] N. Widmer, A. Béguin, B. Rochat, T. Buclin, T. Kovacsóvics, M.A. Duchosal, S. Leyvraz, A. Rosselet, J. Biollaz, L.A. Decosterd, Determination of imatinib (Gleevec®) in human plasma by solid-phase extraction-liquid chromatography-ultraviolet absorbance detection, *J. Chromatogr. B Anal. Technol. Biomed. Life Sci.* 803 (2004) 285–292. doi:10.1016/j.jchromb.2004.01.006.
- [8] S. Pursche, O.G. Ottmann, G. Ehninger, E. Schleyer, High-performance liquid chromatography method with ultraviolet detection for the quantification of the BCR-ABL inhibitor nilotinib (AMN107) in plasma, urine, culture medium and cell preparations, *J. Chromatogr. B Anal. Technol. Biomed. Life Sci.* 852 (2007) 208–216. doi:10.1016/j.jchromb.2007.01.019.
- [9] E.O. Aranda, J. Esteve-Romero, M. Rambla-Alegre, J. Peris-Vicente, D. Bose, Development of a methodology to quantify tamoxifen and endoxifen in breast cancer patients by micellar liquid chromatography and validation according to the ICH guidelines, *Talanta.* 84 (2011) 314–318. doi:10.1016/j.talanta.2011.01.022.
- [10] P.M. Ndangili, A.M. Jijana, P.G.L. Baker, E.I. Iwuoha, 3-Mercaptopropionic acid capped ZnSe quantum dot-cytochrome P450 3A4 enzyme biotransducer for 17 β -estradiol, *J. Electroanal. Chem.* 653 (2011) 67–74. doi:10.1016/j.jelechem.2010.12.029.

- [11] X. Chen, L. Ge, B. Guo, M. Yan, N. Hao, L. Xu, Electrochemical immunoassay for procalcitonin antigen detection based on signal amplification strategy of multiple nanocomposites, *Biosens. Bioelectron.* 58 (2014) 48–56. doi:10.1016/j.bios.2014.02.043.
- [12] G. Volpe, G. Fares, F. delli Quadri, R. Draisci, G. Ferretti, C. Marchiafava, D. Moscone, G. Palleschi, A disposable immunosensor for detection of 17 β -estradiol in non-extracted bovine serum, *Anal. Chim. Acta.* 572 (2006) 11–16. doi:10.1016/j.aca.2006.05.008.
- [13] G. Conneely, M. Aherne, H. Lu, G.G. Guilbault, Development of an immunosensor for the detection of testosterone in bovine urine, *Anal. Chim. Acta.* 583 (2007) 153–160. doi:10.1016/j.aca.2006.09.062.
- [14] S.G. and F.I. Adam Hulanicki, Commission on General Aspects of Analytical Chemistry "Chemical Sensors, Int. Union Pure Appl. Chem. 63 (1991) 1247–1250. doi:10.1351/pac199163091247.
- [15] E.B. Bahadir, M.K. Sezgintürk, Electrochemical biosensors for hormone analyses, *Biosens. Bioelectron.* 68 (2015) 62–71. doi:10.1016/j.bios.2014.12.054.
- [16] L. Asturias-Arribas, M.A. Alonso-Lomillo, O. Domínguez-Renedo, M.J. Arcos-Martínez, Electrochemical determination of cocaine using screen-printed cytochrome P450 2B4 based biosensors, *Talanta.* 105 (2013) 131–134. doi:10.1016/j.talanta.2012.11.078.
- [17] P. Sun, Y. Wu, An amperometric biosensor based on human cytochrome P450 2C9 in polyacrylamide hydrogel films for bisphenol A determination, *Sensors Actuators, B Chem.* 178 (2013) 113–118. doi:10.1016/j.snb.2012.12.055.
- [18] R.F. Ajayi, U. Sidwaba, U. Feleni, S.F. Douman, O. Tovide, S. Botha, P. Baker, X.G. Fuku, S. Hamid, T.T. Waryo, S. Vilakazi, R. Tshikhudo, E.I. Iwuoha, Chemically amplified cytochrome P450-2E1 drug metabolism nanobiosensor for rifampicin anti-tuberculosis drug, *Electrochim. Acta.* 128 (2014) 149–155. doi:10.1016/j.electacta.2013.12.147.
- [19] A. Muthurasu, V. Ganesh, Horseradish Peroxidase Enzyme Immobilized Graphene Quantum Dots as Electrochemical Biosensors, *Appl. Biochem. Biotechnol.* 174 (2014) 945–959. doi:10.1007/s12010-014-1019-7.
- [20] G. Zhiguo, Y. Shuping, L. Zajun, S. Xiulan, W. Guangli, F. Yinjun, L. Junkang, An ultrasensitive hydrogen peroxide biosensor based on electrocatalytic synergy of graphene-gold nanocomposite, CdTe-CdS core-shell quantum dots and gold nanoparticles, *Anal. Chim. Acta.* 701 (2011) 75–80. doi:10.1016/j.aca.2011.06.015.
- [21] E. Schneider, D.S. Clark, Cytochrome P450 (CYP) enzymes and the development of CYP biosensors, *Biosens. Bioelectron.* 39 (2013) 1–13. doi:10.1016/j.bios.2012.05.043.
- [22] D.L. Nelson, M.M. Cox, Principles of Biochemistry, Fifth, W.H Freeman and Company, New York, 2008.
- [23] S. Tafazoli, P.J. O'Brien, Peroxidases: A role in the metabolism and side effects of drugs, *Drug Discov. Today.* 10 (2005) 617–625. doi:10.1016/S1359-6446(05)03394-5.
- [24] M. Khan, S. Park, Journal of Colloid and Interface Science Glucose biosensor based on

- GOx / HRP bienzyme at liquid – crystal / aqueous interface, 457 (2015) 281–288.
- [25] F. Pitzalis, M. Monduzzi, A. Salis, Microporous and Mesoporous Materials A bienzymatic biocatalyst constituted by glucose oxidase and Horseradish peroxidase immobilized on ordered mesoporous silica, 241 (2017).
- [26] G. Palazzo, G. Colafemmina, C. Guzzoni Iudice, A. Mallardi, Three immobilized enzymes acting in series in layer by layer assemblies: Exploiting the trehalase-glucose oxidase-horseradish peroxidase cascade reactions for the optical determination of trehalose, *Sensors Actuators, B Chem.* 202 (2014) 217–233. doi:10.1016/j.snb.2014.05.079.
- [27] K. Radhapyari, P. Kotoky, R. Khan, Detection of anticancer drug tamoxifen using biosensor based on polyaniline probe modified with horseradish peroxidase, *Mater. Sci. Eng. C.* 33 (2013) 583–587. doi:10.1016/j.msec.2012.09.021.
- [28] T. Hu, L. Zhang, W. Wen, X. Zhang, S. Wang, Enzyme catalytic amplification of miRNA-155 detection with graphene quantum dot-based electrochemical biosensor, *Biosens. Bioelectron.* 77 (2016) 451–456. doi:10.1016/j.bios.2015.09.068.
- [29] Z. Wang, Q. Xu, H.-Q. Wang, Q. Yang, J.-H. Yu, Y.-D. Zhao, Hydrogen peroxide biosensor based on direct electron transfer of horseradish peroxidase with vapor deposited quantum dots, *Sensors Actuators B Chem.* 138 (2009) 278–282. doi:10.1016/j.snb.2008.12.040.
- [30] E. Nxusani, P.M. Ndangili, R. a. Olowu, a. N. Jijana, T. Waryo, N. Jahed, R.F. Ajayi, P. Baker, E.I. Iwuoha, 3-Mercaptopropionic Acid Capped Ga₂Se₃nanocrystal-CYP3A4 Biosensor for the Determination of 17-Alpha-Ethinyl Estradiol in Water, *Nano Hybrids.* 1 (2012) 1–22. doi:10.4028/www.scientific.net/NH.1.1.
- [31] X. Xu, J. Qian, J. Yu, Y. Zhang, S. Liu, Cytochrome P450 enzyme functionalized-quantum dots as photocatalysts for drug metabolism, *Chem. Commun.* 1 (2014) 7607–7610. doi:10.1039/c4cc01717j.
- [32] J. Qian, W. Zhu, L. Mi, X. Xu, J. Yu, D. Cui, Y. Xue, S. Liu, Nanohybrids of quantum dots and cytochrome P450 for light-driven drug metabolism, *J. Electroanal. Chem.* 733 (2014) 27–32. doi:10.1016/j.jelechem.2014.09.012.
- [33] T. Zeng, S. Leimkühler, J. Koetz, U. Wollenberger, Effective Electrochemistry of Human Sulfite Oxidase Immobilized on Quantum-Dots-Modified Indium Tin Oxide Electrode, *ACS Appl. Mater. Interfaces.* 7 (2015) 21487–21494. doi:10.1021/acsami.5b06665.
- [34] X. Yang, P. Wang, Y. Zhu, C. Li, Photoelectronic properties of horseradish peroxidase-functionalized CdSe/silica mesoporous composite and its sensing towards hydrogen peroxide, *J. Solid State Electrochem.* 15 (2011) 731–736. doi:10.1007/s10008-010-1147-0.
- [35] Q. Zhang, G. Xu, L. Gong, H. Dai, S. Zhang, Y. Li, Y. Lin, An enzyme-assisted electrochemiluminescent biosensor developed on order mesoporous carbons substrate for ultrasensitive glyphosate sensing, *Electrochim. Acta.* 186 (2015) 624–630. doi:10.1016/j.electacta.2015.10.081.
- [36] W.W. Zhao, Z.Y. Ma, P.P. Yu, X.Y. Dong, J.J. Xu, H.Y. Chen, Highly sensitive photoelectrochemical immunoassay with enhanced amplification using horseradish

- peroxidase induced biocatalytic precipitation on a CdS quantum dots multilayer electrode, *Anal. Chem.* 84 (2012) 917–923. doi:10.1021/ac203184g.
- [37] F. Cai, Q. Zhu, K. Zhao, A. Deng, J. Li, Multiple signal amplified electrochemiluminescent immunoassay for Hg²⁺ using graphene-coupled quantum dots and gold nanoparticles-labeled horseradish peroxidase, *Environ. Sci. Technol.* 49 (2015) 5013–5020. doi:10.1021/acs.est.5b00690.
- [38] J.M. Chalovich, E. Eisenberg, Semiconductor Quantum Dots for Bioimaging and Biodiagnostic Applications, *Biophys. Chem.* 257 (2005) 2432–2437. doi:10.1016/j.immuni.2010.12.017.Two-stage.
- [39] N. Bistolas, U. Wollenberger, C. Jung, F.W. Scheller, Cytochrome P450 biosensors - A review, *Biosens. Bioelectron.* 20 (2005) 2408–2423. doi:10.1016/j.bios.2004.11.023.
- [40] B.R. Gates, B.V. Article, A. Akap, C.G. Nap, Cytochrome P450 Enzymes Selected Cytochrome P450 Substrates, 6 (2017) 1–5.
- [41] K. Auclair, Z. Hu, D.M. Little, P.R. Ortiz de Montellano, J.T. Groves, Revisiting the mechanism of P450 enzymes with the radical clocks norcarane and spiro[2,5]octane, *J. Am. Chem. Soc.* 124 (2002) 6020–6027. doi:10.1021/ja025608h.
- [42] G.E. Hrycay, M.S. Bandiera, Monooxygenase, Peroxidase and Peroxygenase Properties and Mechanisms of Cytochrome, Springer, 2015.
- [43] D. Dolphin, a Forman, D.C. Borg, J. Fajer, R.H. Felton, Compounds I of catalase and horse radish peroxidase: pi-cation radicals., *Proc. Natl. Acad. Sci. U. S. A.* 68 (1971) 614–618. doi:10.1073/pnas.68.3.614.
- [44] G. Battistuzzi, M. Bellei, C.A. Bortolotti, M. Sola, Redox properties of heme peroxidases, *Arch. Biochem. Biophys.* 500 (2010) 21–36. doi:10.1016/j.abb.2010.03.002.
- [45] L.I. Medintz, H.T. Uyeda, R.E. Goldman, H. Mattoussi, Quantum dot bioconjugates for imaging, labelling and sensing, *Nat. Mater.* 4 (2005) 435–336. doi:doi:10.1038/nmat1390.
- [46] W.C.W. Chan, D.J. Maxwell, X. Gao, R.E. Bailey, M. Han, S. Nie, Luminescent quantum dots for multiplexed biological detection and imaging, *Curr. Opin. Biotechnol.* 13 (2002) 40–46. doi:10.1016/S0958-1669(02)00282-3.
- [47] O.E. Semonin, J.M. Luther, M.C. Beard, Quantum dots for next- generation photovoltaics, *Mater. Today.* 15 (2012) 508–515. doi:10.1016/S1369-7021(12)70220-1.
- [48] Y.R. Park, J.H. Doh, K. Shin, Y.S. Seo, Y.S. Kim, S.Y. Kim, W.K. Choi, Y.J. Hong, Solution-processed quantum dot light-emitting diodes with PANI:PSS hole-transport interlayers, *Org. Electron. Physics, Mater. Appl.* 19 (2015) 131–139. doi:10.1016/j.orgel.2014.12.030.
- [49] Z. Jun-Jie, L. Jing-Jing, H. Hai-Ping, C. Fang-Fang, Quantum Dots for DNA Biosensing, Springer Heidelberg, London, 2013.
- [50] T.M. Samir, M.M.H. Mansour, S.C. Kazmierczak, H.M.E. Azzazy, Quantum dots: heralding a brighter future for clinical diagnostics., *Nanomedicine (Lond).* 7 (2012) 1755–69. doi:10.2217/nmm.12.147.

- [51] R.E. Bailey, A.M. Smith, S. Nie, Quantum dots in biology and medicine, *Phys. E Low-Dimensional Syst. Nanostructures*. 25 (2004) 1–12. doi:10.1016/j.physe.2004.07.013.
- [52] L.I.U. Xing, L.U.O. Yang, Surface Modifications Technology of Quantum Dots Based Biosensors and Their Medical Applications, *Chinese J. Anal. Chem.* 42 (2014) 1061–1069. doi:10.1016/S1872-2040(14)60753-2.
- [53] Q. Jiang, D. Zhang, Y. Cao, N. Gan, An antibody-free and signal-on type electrochemiluminescence sensor for diethylstilbestrol detection based on magnetic molecularly imprinted polymers-quantum dots labeled aptamer conjugated probes, 789 (2017) 1–8.
- [54] X. Weng, S. Neethirajan, Biosensors and Bioelectronics A micro fluidic biosensor using graphene oxide and aptamer- functionalized quantum dots for peanut allergen detection, 85 (2016) 649–656.
- [55] T. V Torchynska, G. Polupan, L.G.V. Macotela, *biomolecules*, 170 (2017) 309–313.
- [56] L. Pang, H. Cui, Y. Liu, W. Zhong, Anti-VEGF antibody conjugated CdHgTe quantum dots as a fluorescent probe for imaging in living mouse, 173 (2016) 274–278.
- [57] Y. Li, L. Sun, Q. Liu, E. Han, N. Hao, L. Zhang, S. Wang, J. Cai, K. Wang, Photoelectrochemical CaMV35S biosensor for discriminating transgenic from non-transgenic soybean based on SiO₂@CdTe quantum dots core-shell nanoparticles as signal indicators, *Talanta*. 161 (2016) 211–218. doi:10.1016/j.talanta.2016.08.047.
- [58] X. Zhu, G. Wu, N. Lu, X. Yuan, B. Li, A miniaturized electrochemical toxicity biosensor based on graphene oxide quantum dots/carboxylated carbon nanotubes for assessment of priority pollutants, *J. Hazard. Mater.* 324 (2017) 272–280. doi:10.1016/j.jhazmat.2016.10.057.
- [59] B. Ertek, Y. Dilgin, Photoamperometric flow injection analysis of glucose based on dehydrogenase modified quantum dots-carbon nanotube nanocomposite electrode, *Bioelectrochemistry*. 112 (2015) 138–144. doi:10.1016/j.bioelechem.2016.02.008.
- [60] Ö. Saglam, B. Kizilkaya, H. Uysal, Y. Dilgin, Biosensing of glucose in flow injection analysis system based on glucose oxidase-quantum dot modified pencil graphite electrode, *Talanta*. 147 (2016) 315–321. doi:10.1016/j.talanta.2015.09.050.
- [61] E. Han, Y. Yang, Z. He, J. Cai, X. Zhang, X. Dong, Development of tyrosinase biosensor based on quantum dots / chitosan nanocomposite for detection of phenolic compounds, *Anal. Biochem.* 486 (2015) 102–106. doi:10.1016/j.ab.2015.07.001.
- [62] D. Du, W. Chen, J. Cai, J. Zhang, F. Qu, H. Li, Development of acetylcholinesterase biosensor based on CdTe quantum dots modified cysteamine self-assembled monolayers, *J. Electroanal. Chem.* 623 (2008) 81–85. doi:10.1016/j.jelechem.2008.06.020.
- [63] S. Liu, L. Peng, X. Yang, Y. Wu, L. He, Electrochemistry of cytochrome P450 enzyme on nanoparticle-containing membrane-coated electrode and its applications for drug sensing, *Anal. Biochem.* 375 (2008) 209–216. doi:10.1016/j.ab.2007.12.001.
- [64] V. V. Shumyantseva, S. Carrara, V. Bavastrello, D.J. Riley, T. V. Bulko, K.G. Skryabin, A.I. Archakov, C. Nicolini, Direct electron transfer between cytochrome P450_{scc} and gold nanoparticles on screen-printed rhodium-graphite electrodes, *Biosens. Bioelectron.* 21 (2005) 217–222. doi:10.1016/j.bios.2004.10.008.

- [65] J. Lu, Y. Zhang, H. Li, J. Yu, S. Liu, Electrochemically driven drug metabolism via a CYP1A2-UGT1A10 bienzyme confined in a graphene nano-cage, *Chem Commun.* 50 (2014) 13896–13899. doi:10.1039/c4cc06200k.
- [66] D. Cui, L. Mi, X. Xu, J. Lu, J. Qian, S. Liu, Nanocomposites of graphene and cytochrome P450 2D6 isozyme for electrochemical-driven tramadol metabolism, *Langmuir.* 30 (2014) 11833–11840. doi:10.1021/la502699m.
- [67] H. Tavakoli, A. Azam, Bioelectrochemistry Measuring hydrogen peroxide due to water radiolysis using a modified horseradish peroxidase based biosensor as an alternative dosimetry method, 104 (2015) 79–84.
- [68] R. Cui, H. Huang, Z. Yin, D. Gao, J.J. Zhu, Horseradish peroxidase-functionalized gold nanoparticle label for amplified immunoanalysis based on gold nanoparticles/carbon nanotubes hybrids modified biosensor, *Biosens. Bioelectron.* 23 (2008) 1666–1673. doi:10.1016/j.bios.2008.01.034.
- [69] W.-W. Zhao, J.-J. Xu, H.-Y. Chen, Photoelectrochemical enzymatic biosensors, *Biosens. Bioelectron.* (2016) 0–1. doi:10.1016/j.bios.2016.11.009.
- [70] F. Wu, Z. Hu, J. Xu, Y. Tian, L. Wang, Y. Xian, L. Jin, Immobilization of horseradish peroxidase on self-assembled (3-mercaptopropyl)trimethoxysilane film: Characterization, direct electrochemistry, redox thermodynamics and biosensing, *Electrochim. Acta.* 53 (2008) 8238–8244. doi:10.1016/j.electacta.2008.06.031.
- [71] L. Liu, F. Zhao, L. Liu, J. Li, B. Zeng, Improved direct electron transfer and electrocatalytic activity of horseradish peroxidase immobilized on gemini surfactant-polyvinyl alcohol composite film, *Colloids Surfaces B Biointerfaces.* 68 (2009) 93–97. doi:10.1016/j.colsurfb.2008.09.018.
- [72] M. Hasanzadeh, N. Shadjou, M. Eskandani, J. Soleymani, F. Jafari, M. de la Guardia, Dendrimer-encapsulated and cored metal nanoparticles for electrochemical nanobiosensing, *TrAC - Trends Anal. Chem.* 53 (2014) 137–149. doi:10.1016/j.trac.2013.09.015.

Chapter 3: Preparation of water-soluble CuSe QDs

Summary

This chapter describes the synthesis of water-soluble and biocompatible copper selenide quantum dots (CuSe QDs) produced by a simple, inexpensive and reproducible aqueous method capped with 6-mercaptohexanoic acid (6MHA), 3-mercaptopropionic acid (3MPA) or mercaptosuccinic acid (MSA) to improve their stability and solubility. Also, this chapter describes the various chemicals and analytical techniques employed, followed by a detailed experimental procedure based on the synthesis of CuSe QDs. Some techniques used for QDs characterization, such as electrochemical (Cyclic voltammetry), microscopic (HRTEM and HRSEM) and spectroscopic methods (UV-vis absorption and photoluminescence) are also presented in the chapter.

Abstract

Metal-selenide quantum dots (QDs) have shown favorable electrical, optical and optoelectrical properties, making them a suitable alternative for biosensor applications. Amongst these the copper selenide (CuSe) QDs are an attractive alternative for optoelectronic devices. Due to the poor water-solubility of QDs in general, surface modifications are often needed in order to obtain biocompatibility. In the work presented, water-soluble, biocompatible copper selenide quantum dots were synthesized through a quick, facile aqueous route. Three different capping agents: 6-mercaptohexanoic acid (6MHA), 3-mercaptopropionic acid (3MPA) and mercaptosuccinic acid (MSA) were used for the QDs synthesis. The effect of the capping agent on stoichiometry, particle core and hydrodynamic size, stability in aqueous solution, stoichiometry and optical and electrochemical properties was investigated through a number of characterization techniques. X-ray diffraction analysis (XRD) confirmed formation of copper selenide species of non-stoichiometric form Cu_{2-x}Se (for the 6MHA and 3MPA capped CuSe QDs) and $\beta\text{-CuSe}$ stoichiometric form (for the MSA capped CuSe QDs). XRD and high resolution electron microscopy (HRTEM) confirmed that 6MHA capped CuSe QDs had the smallest average particle core size when dried. Whereas small-angle x-ray scattering (SAXS) and dynamic light scattering (DLS) showed MSA capped CuSe QDs had the smallest size in aqueous solution, though with a high ability to aggregate. The capping of CuSe QDs was confirmed by FTIR via the specific COOH, CH₂ and C-S signature bands of 3MPA and 6MHA. The water-soluble nature of the MSA-CuSe QDs pointed towards bonding of the thiol carboxylic acid. However, the MSA bond to the CuSe QDs is probably unstable, leading to lower stability of the QDs in aqueous solution. UV-vis absorption confirmed a large blue shift of the band gap compared to the bulk material for all formed QDs which is attributed to the quantum confinement effect. Photoluminescence (PL) measurements showed that the QDs emit light at 435 nm (6MHA and 3MPA capped CuSe QDs) and 485 nm (MSA capped CuSe QDs). The electrochemical properties investigated through cyclic voltammetry of the formed CuSe QDs makes them a possible alternative as an electron mediator and enzyme mobilizing agent in enzymatic electrochemical biosensors.

3.1 Introduction

Quantum dots (QDs) are semi-conductive nanocrystals with a diameter range of 2-10 nm. More specifically they are defined as particle with physical dimensions smaller than the exciton Bohr radius and are sometimes referred to as large “artificial atoms”.[1–3] Due to their favorable photochemical, electrical and size-tunable optical properties, QDs have been used for multiple applications including light-emitting diodes (LED), photovoltaics and bioimaging and medical diagnostics.[4–7]

Metal-selenide QDs have been studied extensively and shown favorable electrical, optical and optoelectrical properties thanks to their ability to absorb light in the visible region and transferred electrons to large bandgap semiconductors.[8–11] Amongst these, the copper selenide (CuSe) QDs are an attractive alternative for optoelectronic devices.[12,13] Copper selenide is a p-type semiconductor which has been studied for applications such as solar cells, super-ionic conductors, optical filters and cancer therapy.[11,12,14,15] The material can appear in different stoichiometries: CuSe, Cu₂Se, and Cu₃Se₂, to mention a few, non-stoichiometric form (Cu_{2-x}Se) and multiple crystal structures (orthorhombic, hexagonal, tetragonal, cubic etc.).[16] The stoichiometry and phase has shown to have strong influence on the band gap and thermal stability of the material.[17,18] The copper selenide has been well explored as a nanosized material with multiple structures such as platelets, snakes, bipyramids and tubes [19–22] However, in recent years, the synthesis of size-quantized particles of copper selenides has gained interest in the science community.[12,15,23–25] Various routes have been reported on the synthesis of CuSe QDs and many procedures require heating, specialized equipment and/or are time consuming.[13,15,20,23–33] Furthermore, the CuSe QDs often requires organic solvents such as toluene, cyclohexane and chloroform.[13,20,23,26] Therefore they are not biocompatible and not applicable in biosensor fabrication. Recent studies have reported dispersing CuSe QDs in aqueous Rhodamine-B solution for analysis of photocatalytic activity.[7] However, other reported solvents have been water-in-oil emulsion (published by Ingole and co-workers [32]) and nitric acids (studied by Li and co-workers [28]). No reports have been presented regarding improving the CuSe QDs water solubility. Although, Hessel and co-workers reported synthesis of biocompatible, water-soluble CuSe spherical nanocrystals with an average size slightly over the range for QDs (of 16 nm). The CuSe nanocrystals were encapsulated with an amphiphilic polymer which enabled dispersion in aqueous phosphate buffer saline (PBS) at physiological pH 7.40.[14]

Due to the poor water-soluble nature of QDs in general, surface modifications are often required to improve dispersity in water and obtain biocompatibility. These modifications often involves capping the nanocrystal with either polymers, thiol compounds, mercapto propionic acid compounds or organic compounds.[34] The most commonly used capping agents and ligands for CuSe QDs have been focused on the long-chained amines such as (hexadecylamine and oleylamine), phosphoric compounds (tri-n-octylphosphine and 1-dodecylphosphonic acid) and carboxylic acid (oleic and stearic acid). The particles could be dispersed in organic solvents.[12,13,15,20,23,26,27,30] Also the smaller molecule ammonium thiocyanate was explored as capping agent to enable photovoltaic application of CuSe QDs.[13] However, a few thiol ligands have been explored for synthesis of CuSe QDs. Balitski and co-workers [26] reported the use of 1-dodecanethiol for capping of CuSe nanocrystals that was dispersed in toluene. Furthermore, Ingole and co-workers [32] reported the synthesis of 1-hexanethiolate capped CuSe QDs that were synthesized through a water-in-oil micro emulsion technique. In both cases, the authors argue that the thiol group is reacting with the copper cation through electron donation of the unpaired electrons on the sulfur atom.[26,32] On another note, Chen and co-workers reported the utilization of 2-mercaptoethanol as a stabilizing agent for formation of copper selenide nanostructures. [35] Short chained thiol carboxylic acids such as 3-mercaptopropionic acid are commonly used for Cd- and Zn- based QDs and result in water soluble and biocompatible particles.[34] However, these compounds are yet to be explored for capping of CuSe QDs.

In this work a green, room temperature, fast aqueous route is used for synthesizing water soluble copper selenide quantum dots using three different capping agents with different properties. The synthesis method was based on a previous method presented by Ndangili and co-workers [36] for synthesis of 3-mercaptopropionic acid capped ZnSe QDs, with some modifications. For the capping of the CuSe QDs the branched molecule mercaptosuccinic acid (MSA), the shorter linear molecule 3-mercaptopropionic acid (3MPA) and the longer chained linear molecule 6-mercaptophexanoic acid (6MHA) have been explored. The structure of the capping agents is illustrated in Figure 3.1.

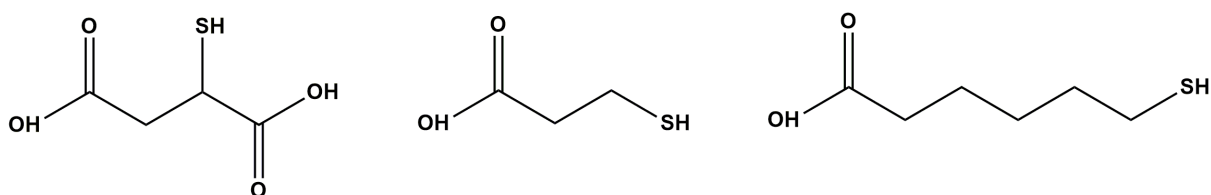


Figure 3.1 Molecular structure of MSA (left), 3MPA (middle) and 6MHA (right).

In the synthesis, the strong S-Cu interaction was utilized. Copper cations (Cu^{2+} and Cu^+) has shown to integrate strongly with thiol compounds (RSH) such as mercaptosuccinic acid. When Cu^{2+} ratio is below 0.5 to the thiol compound RSH in the reaction mixture, a RS-Cu^+ complex is formed.[37] Leaving the carboxylic ends of the capping agents free to integrate with the polar solvent. It is then possible to further conjugate the quantum dots to biological molecules such as enzymes. Enabling the applications of the capped CuSe QDs as a part of an enzymatic biosensor.[34,36,38]



3.2 Experimental

3.2.1 Chemicals

All chemicals used in the experiments were of analytical grade and were used as purchased without further purification. 3-mercaptopropionic acid (3MPA, $\geq 99.0\%$), mercaptosuccinic acid (MSA, $\geq 98.0\%$), 6-mercaptophexanoic acid (90%), copper(II) nitrate hydrate ($\text{Cu}(\text{NO}_3)_2$, 99.999% trace metal basis), selenium powder (99.99% metal basis), sodium borohydride (NaBH_4 , 98%), Sodium hydroxide (NaOH , 99.99% trace metal basis), sodium phosphate dibasic dihydrate (Na_2HPO_4 , $\geq 99.5\%$), sodium phosphate monobasic monohydrate (NaH_2PO_4 , $\geq 99.0\%$) were purchased from Sigma-Aldrich (Cape Town, South Africa). 0.1 M phosphate buffer solution, pH 7.4 was prepared from disodium hydrogen phosphate dibasic and sodium dihydrogen phosphate monobasic using Millipore (18 M Ω /cm) purified through SimPak[®] 1 water purification system (Merck Millipore, Germany).

3.2.2 Instrumentation

X-ray diffraction patterns were collected using a D8 High-Resolution Diffractometer from Bruker, United States. Samples were precipitated through dilution with acetone. The samples were centrifuged and dried to a powder at 50 °C under vacuum prior to analysis. XRD experiment and analysis of compound composition from the XRD pattern was performed by iThemba LABS, Summerset West, South Africa.

Screen printed carbon electrodes (ref. DRP-110) from DropSens, Spain, were used as working electrode to prepare samples for high resolution scanning electron microscope (HRSEM) analysis and energy dispersive spectroscopy (EDS). The analysis was performed using an Auriga Scanning Electron Microscope from Zeiss, Germany. Further analysis was performed using ImageJ software. Samples were sonicated, filtrate through centrifugal filter and drop coated on a carbon screen printed electrode (SPE). The electrodes were allowed to dry overnight. High resolution transmission electron microscopy (HRTEM) and selected area electron diffraction (SAED) together with EDS analysis was performed using Tecnai F20 Field Emission Transmission Electron Microscope from FEI, Oregon, United States. Samples were sonicated for 30 min and mounted on a nickel grid and allowed to dry under lamp. Images were further analyzed in ImageJ software. Small angle x-ray scattering (SAXS) was done using SAXSpace Small- and Wide-Angle Scattering System, from Anton-paar, Austria, using 35 μL

of non-diluted liquid sample. A scattering curve was collected in SAXdrive software. Zero point calibration was performed on the scattering curve using SAXtreat software and background scattering removed using SAXquant software. Thereafter GIFT software was used in order to Fourier transform the scattering curve to pair distance distribution function (PDDF) and size distribution curves. Hydrodynamic size (by number) and zeta potential was investigated by dynamic light scattering (DLS) using Zetasizer Nano ZS from Malvern instruments, UK. Samples were sonicated and filtered through centrifugal filter prior to analysis. Disposable polystyrene cuvettes from SARSTEDT, Germany, was used for particle size measurements. Disposable capillary zeta cell from Malvern Instruments, Germany, was used for zeta potential measurements.

Fourier transform infrared (FTIR) spectroscopy was performed with Perkin Two IR Spectrometer from Perkin Elmer, United States. Samples were precipitated and dried to a powder at 50 °C under vacuum. The dried powder was grinded together with KBR and pressed to a thin pellet prior to analysis. Raman spectroscopy was performed with XploRa PLUS Raman Microscope from Horiba Scientific, Japan. Samples were drop coated on glass plates and allowed to dry. Ultraviolet-visible (UV-vis) absorption measurements were performed using a Nicolet Evolution 100 UV-visible spectrometer from Thermo Electron, UK. 15 µL of the sample was diluted with 800 µL distilled H₂O in a quartz cuvette. Photoluminescence (PL) measurement was done with Fluorolog-3 Spectrofluorometer from Horiba, Japan. 37 µL of the sample was diluted with 2963 µL distilled H₂O in a quartz cuvette.

Cyclic voltammetry (CV) was performed using BAS100W integrated and Automated Electrochemical Work Station from Bio Analytical Systems, Lafayette, USA. A three electrode setup was used in a 10 mL electrochemical cell. A gold electrode (surface area = 0.0201 cm²) from BAS was used as working electrode, a platinum wire from Sigma Aldrich served as the counter electrode and a Ag/AgCl (3 M NaCl) from BAS was used as the reference electrode.

3.2.3 Synthesis of 6-mercaptohexanoic acid, 3-mercaptopropionic acid and mercaptosuccinic acid capped CuSe quantum dots

Elemental selenium powder was reduced using NaBH₄. The reduction reaction was carried out as follows: 7.9 mg selenium powder was added together with 7.6 mg NaBH₄ in a round bottom flask and diluted with 10 mL distilled water. Mixture was allowed to react under N₂(g) saturation with stirring until solution turned bright orange. A 10 mL Se²⁻ were prepared separately for each synthesis.

Separately, a $\text{Cu}(\text{NO}_3)_2$ and capping agent solution was prepared as follows: 38 Mg $\text{Cu}(\text{NO}_3)_2$ powder was added to a round bottom flask. 240 g of mercaptosuccinic acid (MSA) was added to the round bottom flask for synthesis of MSA capped CuSe QDs. For 3MPA and 6MHA capped CuSe QDs 140 μL of 3MPA and 306 μL of 6MHA was added respectively. The mixture was diluted to 10 mL with distilled water and pH adjusted to pH 11.8 with 2 M NaOH. The solution was saturated with $\text{N}_2(\text{g})$ for 40 min under stirring.

The QDs synthesis reaction was initialized by dropwise adding the total volume of Se^{2-} solution to the $\text{Cu}(\text{NO}_3)_2$ and capping agent solution. This created the final ratio of $\text{Se}^{2-}:\text{Cu}^{2+}:\text{Capping agent}$ to be 1:2:8 in the reaction mixture. The reaction was allowed to react under stirring in $\text{N}_2(\text{g})$ saturated environment. After 15 min a dark brown/black solution has formed and the reaction was quenched in $-20\text{ }^\circ\text{C}$ for 20 min. Solutions were bottled and kept in $-20\text{ }^\circ\text{C}$ (MSACuSe QDs) or $4\text{ }^\circ\text{C}$ (6MHACuSe and 3MPACuSe QDs).

3.2.4 Preparation of modified electrode

The quantum dots were drop-coated on the gold electrode surface and dried in room temperature in dark. Analyzed with BASW software. Before electrode modification the electrodes were polished with alumina micro polish and polishing pads (Buehler, USA). For precursor studies: 1 mL of the precursors (prepared with the same concentrations as precursors solutions described in synthesis) were diluted with 3 mL of 0.1 M phosphate buffer (pH 7.40). All experiments were performed in phosphate buffer saturated with $\text{Ar}(\text{g})$ for 15 min.

3.3 Results and discussion

3.3.1 Characterization

3.3.1.1 Chemical composition and crystal structure

Chemical composition and stoichiometry of the CuSe QDs and crystallinity was evaluated through x-ray diffraction (XRD). The crystal structure (face-centered cubic) was confirmed through selected area electron diffraction (SAED). Powder X-ray diffraction patterns for the CuSe QDs capped with 6MHA, 3MPA and MSA are illustrated in Figure 3.2 together with the SAED spectra for corresponding sample.

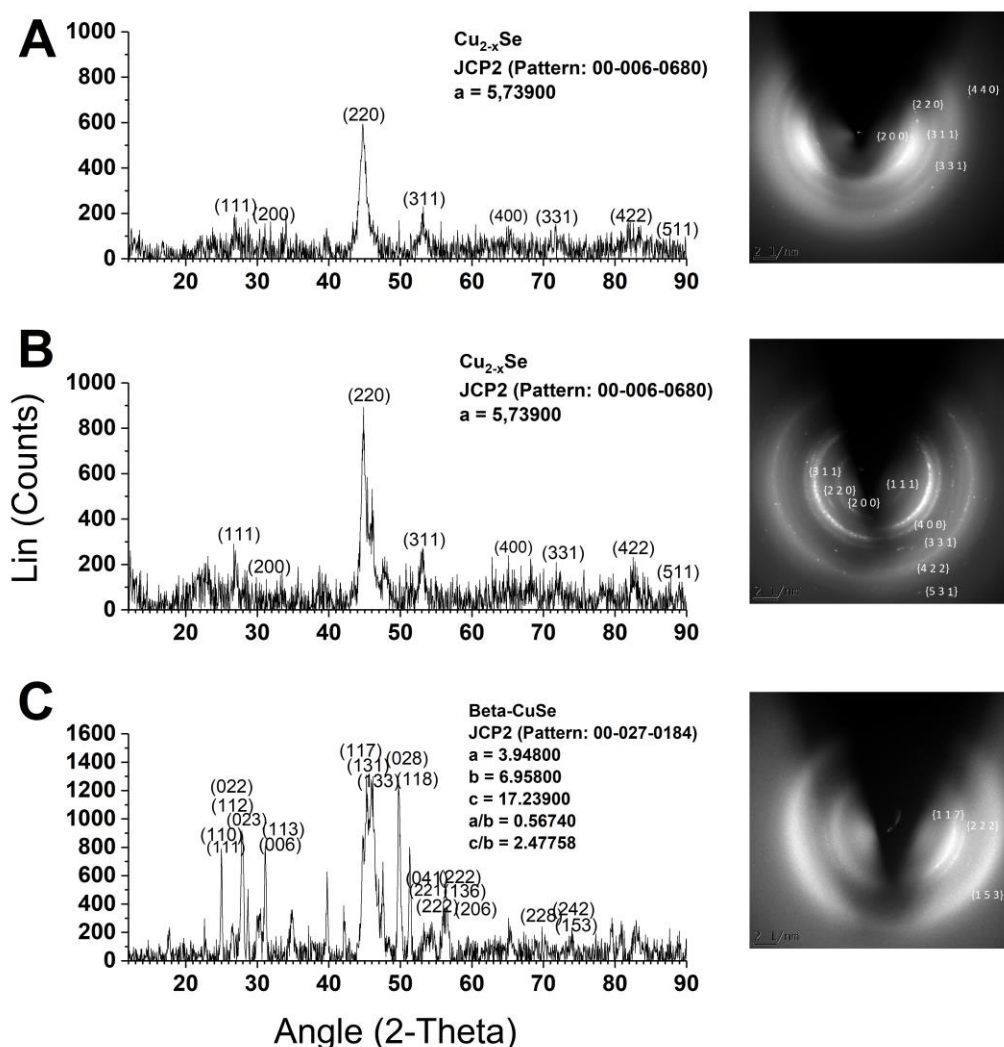


Figure 3.2 The X-ray diffractograms (left) and SAED spectra (right) of A) 6MHACuSe QDs B) 3MPACuSe QDs and C) MSCuSe QDs.

The x-ray diffraction pattern for the 6MHACuSe QDs (Figure 3.2 A) shows characteristic features corresponding to (111), (200), (220), (311), (400), (331), (422), (511) planes which is in good agreement with the JCPDS (Join Committee on Powder Diffraction standards) card no. 00-006-0680, of Cu_{2-x}Se with face-centered cubic structure. The selected area diffraction (SAED) pattern shows discontinuous rings with bright spots, indicating that the nanoparticles formed are crystalline. The fact that some rings appear in higher intensities (220) indicates that the QDs have a certain preferred orientations of the Cu_{2-x}Se planes in contrast to random orientation.[39,40] By measuring the radii of the rings, the d-spacing of the SAED pattern was investigated using Equation 3.1.[41]

$$d = \frac{\lambda L}{R} \quad (3.1)$$

Where R is the radii of a ring, measured as half the distance between to opposite laying bright spots in the SAED pattern, d is the d-spacing, λ is the electron wavelength and L is the camera length.[41] Through this, d-spacing were found corresponding to (200), (220), (311), (331) and (440) of face-centered cubic structure, confirming the results from the XRD pattern.

Similar results were obtained for the x-ray diffraction pattern of 3MPACuSe QDs (Figure 3.2 B) where the same (111), (200), (220), (311), (400), (331), (422), (511) planes could be identified as Cu_{2-x}Se with face-centered cubic structure. There is also diffraction peaks in the XRD pattern indicating presence of small portions of copper selenide in the stoichiometric form of CuSe (JCPDS card no. 00-026-0556) in hexagonal structure, causing the slight difference between the XRD pattern obtained for 6MHACuSe and 3MPACuSe QDs. The d-spacing of the corresponding SAED pattern revealed planes corresponding to (111), (200), (220), (311), (400), (422) and (531) planes of face-centered cubic structure.

In comparison, MSACuSe QDs (Figure 3.2 C) the XRD pattern reveals a different stoichiometry in the copper selenide nanocrystals. The diffraction pattern showed features corresponding to (110), (111), (022), (112), (023), (113), (006), (117), (131), (200), (133), (028), (118), (041), (221), (222), (136), (206), (228), (242), (153) planes, which in accordance with the pattern for $\beta\text{-CuSe}$ (JPSDC card no. 00-027-0184) base-centered orthorhombic structure. The pattern also revealed diffraction peaks caused by small fractions of another stoichiometric form Cu_3Se_2 (JCPDS, card no. 00-027-0184). Showing that the use of the

branched thiol carboxylic acid as capping agent resulted in other stoichiometric forms of the copper selenide compared to when linear capping agents were used. Furthermore, the d-spacing values obtained from the SAED pattern corresponded to the (112), (222) and (153) in base-centered orthorhombic structure.

The broadening of the peaks in the XRD pattern in comparison to the bulk material is caused by the small size of the QDs. Through Scherrer formula (Equation 3.2) it is possible to get an estimation of the particle size.[24]

$$A = \frac{0.94\lambda}{\beta \cos(\theta)} \quad (3.2)$$

Where A corresponds to the average crystallite size, β is the full-widths-at-half-maximum (FWHM) of the diffraction peaks, θ is the angle of diffraction and λ signifies the wavelength used for the X-ray irradiation (1.5406 Å). The average crystallite size was calculated from multiple diffraction angles θ and the average particle size was calculated to be 9.8, 10.3 and 22.1 nm for 6MHACuSe, 3MPACuSe and MSACuSe QDs respectively. In the sample prepared for XRD analysis, the MSACuSe nanocrystals diameter fall outside the range of quantum dots. The nanoparticles were precipitated with acetone, centrifuged and dried prior to XRD analysis. There is a possibility that the mercaptosuccinic acid capping agent detached when the particles were precipitated in acetone, causing agglomeration of the QDs and thus the high average particle size obtained.[34] The result from the synthesis using the MSA as capping agent differed from the synthesis where 6MHA and 3MPA were used. Indicating the choice of capping agent can have effect of the stoichiometry and the stability of the QDs. Nevertheless, the SAED and the x-ray diffraction patterns shows that crystalline nanoscale copper selenide species have been successfully formed in the synthesis.

3.3.1.2 Particle size, morphology and crystallinity

Particle size, morphology and further assessment of crystallinity was evaluated using high resolution electron microscopy (HRTEM) and high resolution scanning electron microscopy (HRSEM) together with energy dispersive x-ray spectroscopy (EDS) to confirm the chemical composition. HRTEM studies were performed on a nickel grid where samples were sonicated,

drop coated and allowed to dry under lamp. Results from HRTEM studies are shown in Figure 3.3 to Figure 3.5.

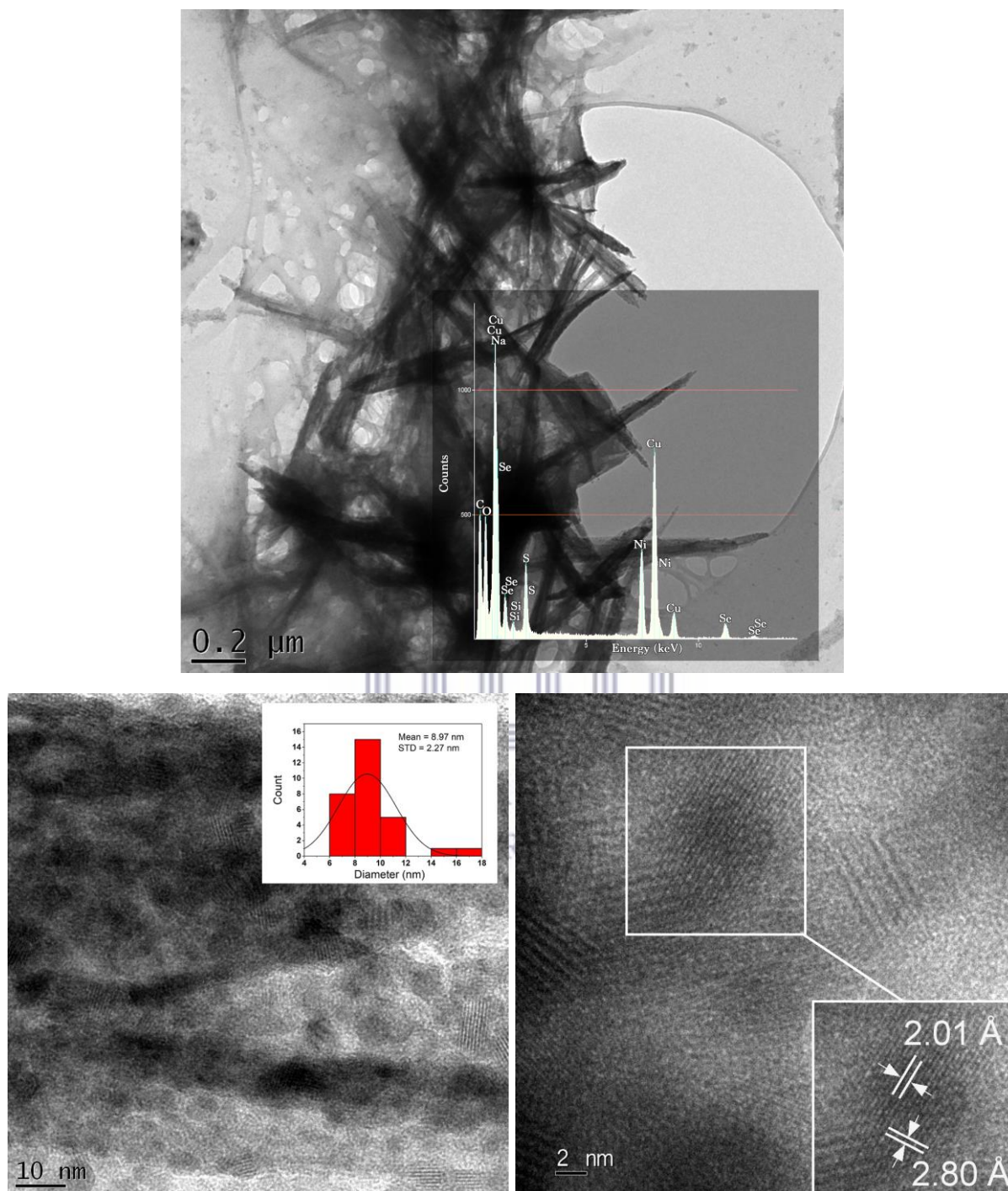


Figure 3.3 HRTEM images of 6MHACuSe QDs at magnitude of 0.20 μm (top), 10 nm (bottom left) and 2 nm (bottom right). Together with EDS graph (top), size distribution histogram (bottom left) and illustration of lattice fringes measures (bottom right).

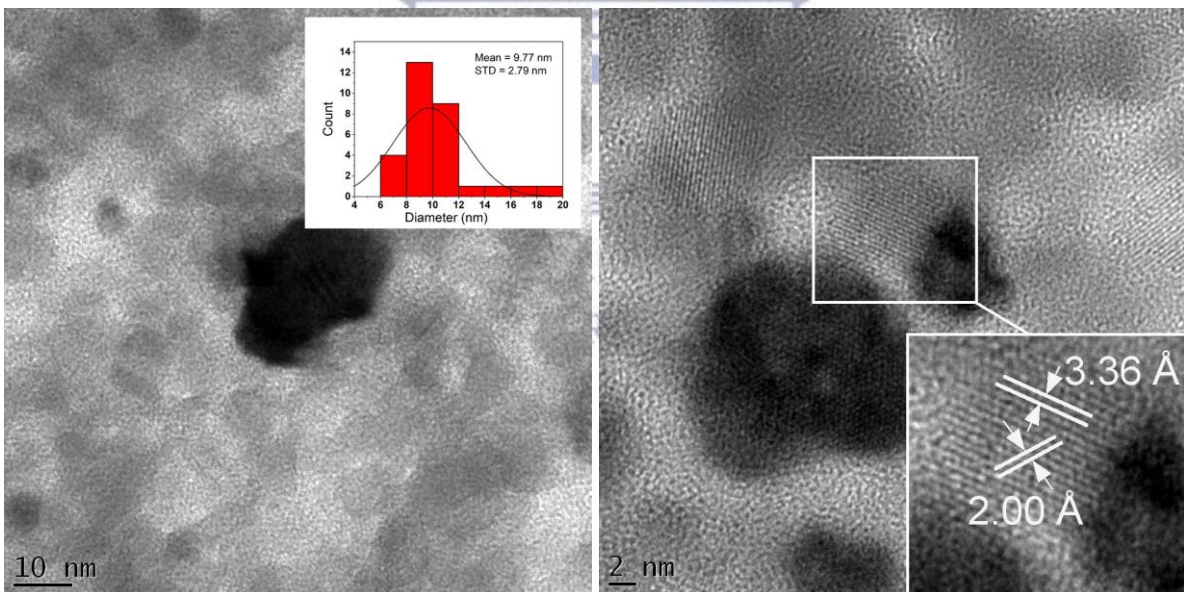
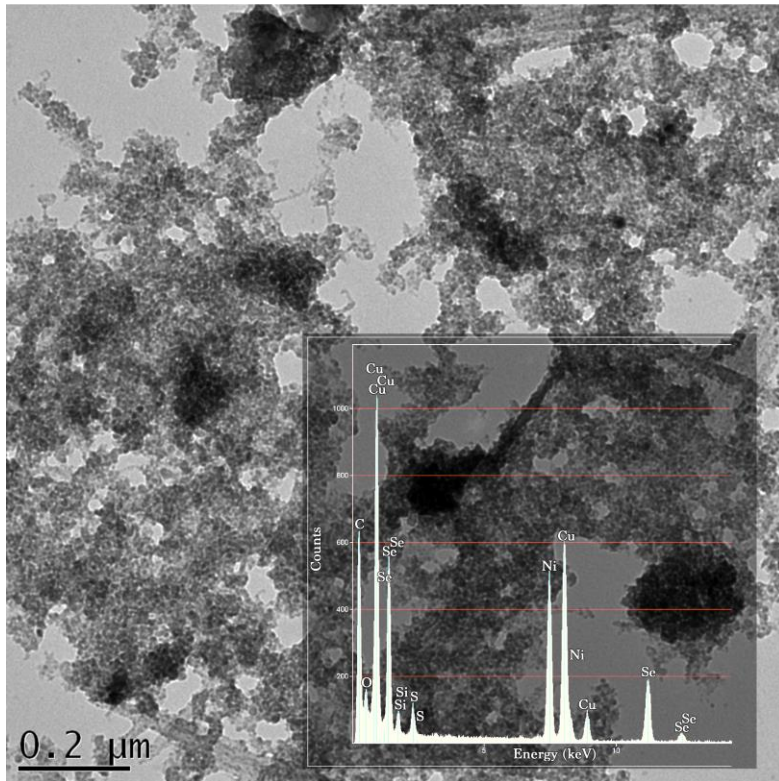


Figure 3.4 HRTEM images of 3MPACuSe QDs at magnitude of 0.20 μm (top), 10 nm (bottom left) and 2 nm (bottom right). Together with EDS graph (top), size distribution histogram (bottom left) and illustration of lattice fringes measures (bottom right).

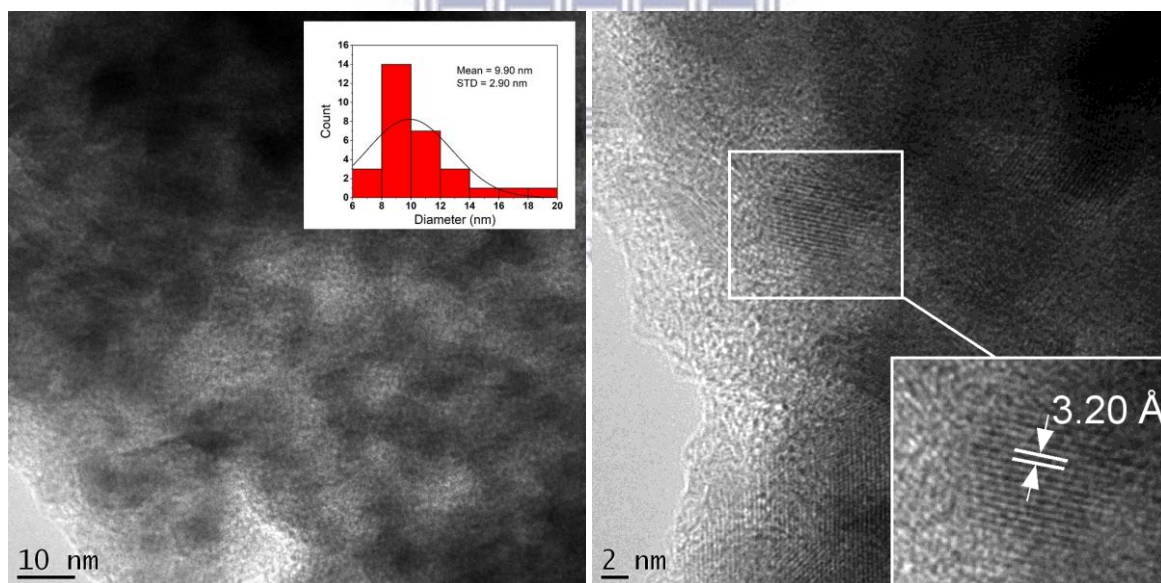
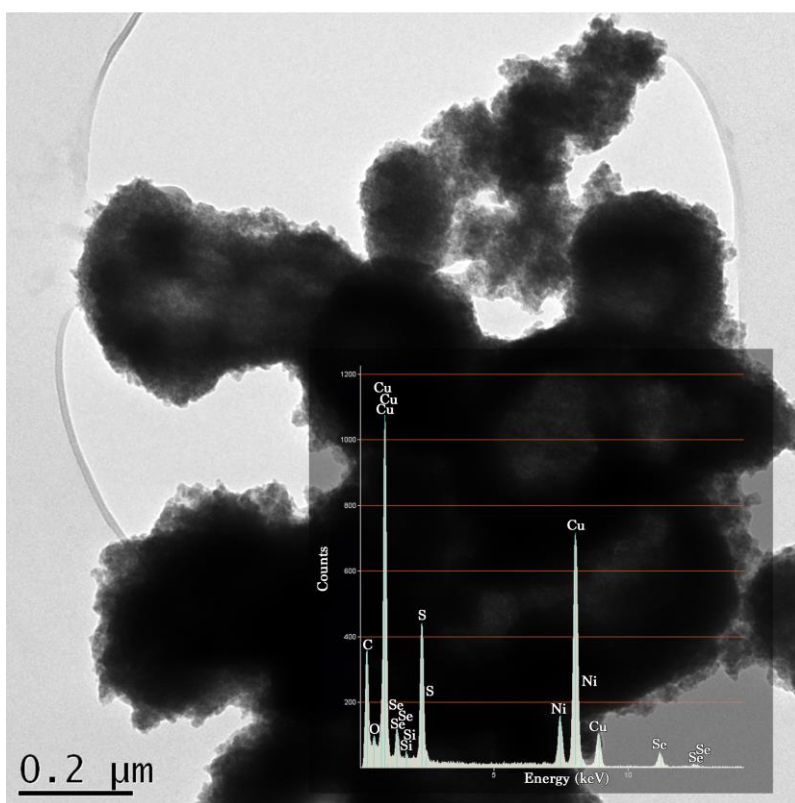


Figure 3.5 HRTEM images of MSACuSe QDs at magnitude of 0.20 μm (top), 10 nm (bottom left) and 2 nm (bottom right). Together with EDS graph (top), size distribution histogram (bottom left) and illustration of lattice fringes measures (bottom right).

In Figure 3.3 to Figure 3.5 it is possible to see that spherical particles have been formed with a diameter within the nanorange. Table 3.1 shows a summary of the particle sizes and the size range. In accordance with the XRD spectra, the 6MHACuSe (Figure 3.3) had the smallest particle size. The average particle size (calculated from a sample number of $N = 30$ particles)

was found to be 8.97 ± 2.27 nm in diameter. The lattice fringes visible in the HRTEM indicates good crystallinity. The distance between the fringes represents the inter-planar spacing (d-spacing). In the case of the 6MHACuSe QDs, lattice fringes of size 3.35, 2.80 and 2.01 Å could be measured and could be connected to the (111), (220) and (200) planes of Cu_{2-x}Se face-centered cubic structure. 3MPACuSe (Figure 3.4) has an average particle size of 9.77 ± 2.79 nm ($N = 30$). The observable lattice fringes had sizes of: 3.36, 2.55 and 2.00 Å which was attributed to (111), (220) and (200) planes of the Cu_{2-x}Se face-centered cubic structure. MSACuSe QDs gave the largest average particle size with 9.90 ± 4.35 nm ($N = 30$). Lattice fringes of sizes: 3.37, 3.20, 2.80, 2.15, 1.70 and 1.60 Å were measured and indexed to (111), (022), (006), (117), (221) and (206) planes of β -CuSe base-centered orthorhombic structure. Furthermore, in Figure 3.5 it is observable that the MSACuSe QDs have a tendency to form lumps on the nickel grid. The results indicate that the MSA capped CuSe QDs has a sensitivity towards drying. A similar problem was encountered by Ingole and co-workers [32] for 1-hexanethiolated capped Cu_{2-x}Se QDs, which occurred too heavily agglomerate on the surface of the TEM grid, making analysis of the particle size impossible.

| Nanoparticle | Average particle diameter (nm) | Particle size range (nm) |
|--------------|--------------------------------|--------------------------|
| 6MHACuSe | $8.97 (\pm 2.27)$ | 5.75 – 16.55 |
| 3MPACuSe | $9.77 (\pm 2.79)$ | 6.23 – 18.33 |
| MSACuSe | $9.90 (\pm 4.35)$ | 6.75 – 18.57 |

Table 3.1 Average particle diameter and particle size range for the 6MHACuSe, 3MPACuSe and MSACuSe QDs.

HRSEM analysis was performed on carbon SPE where the samples were drop coated and allowed to dry overnight. The results from the HRSEM together with corresponding the EDS analysis are shown in Figure 3.6 to Figure 3.8.

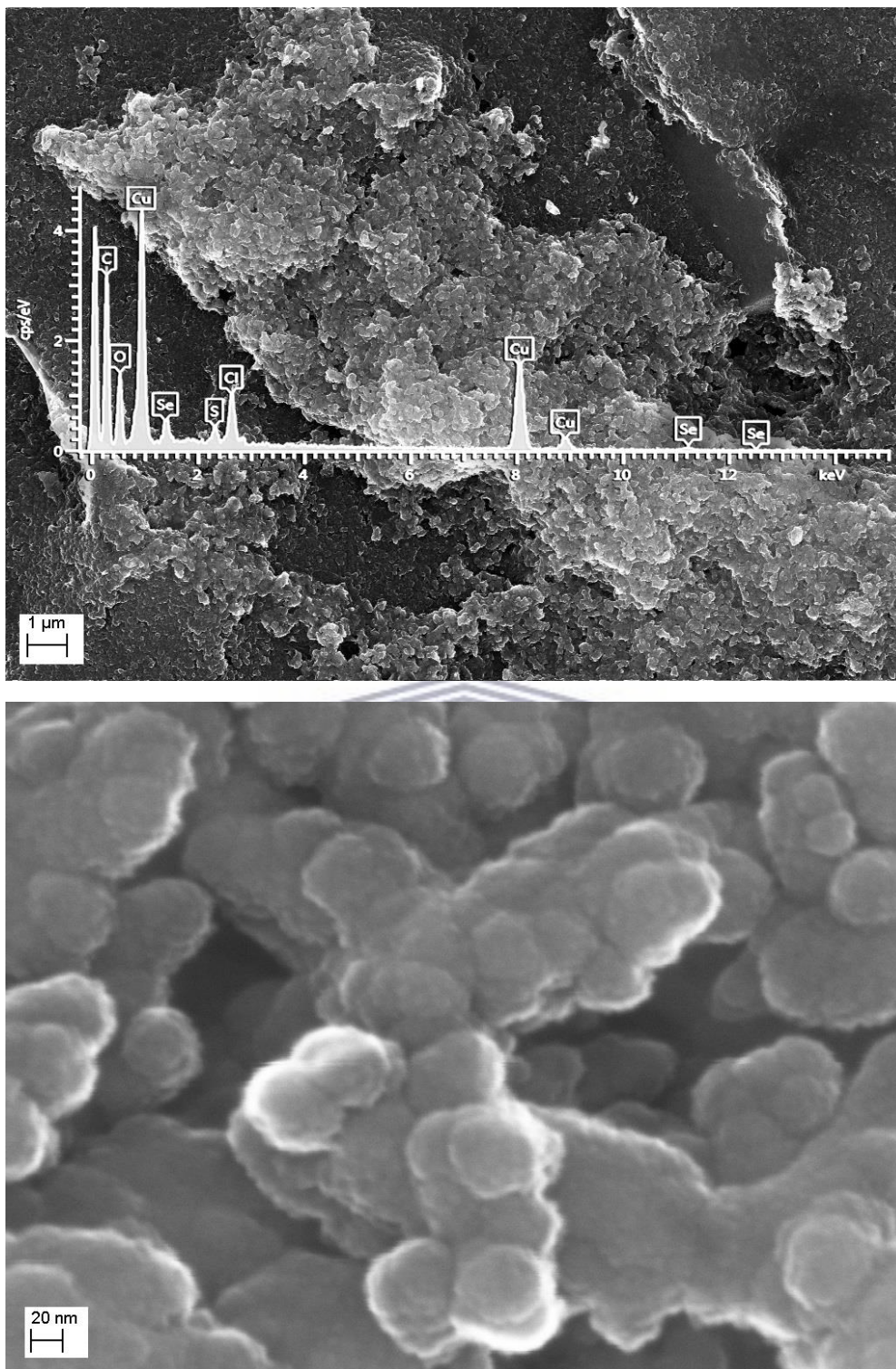


Figure 3.6 HRSEM of 6MHACuSe on carbon SPE at magnitude of 1 μm (top) and 20 nm (bottom). EDS spectra is shown in top figure.

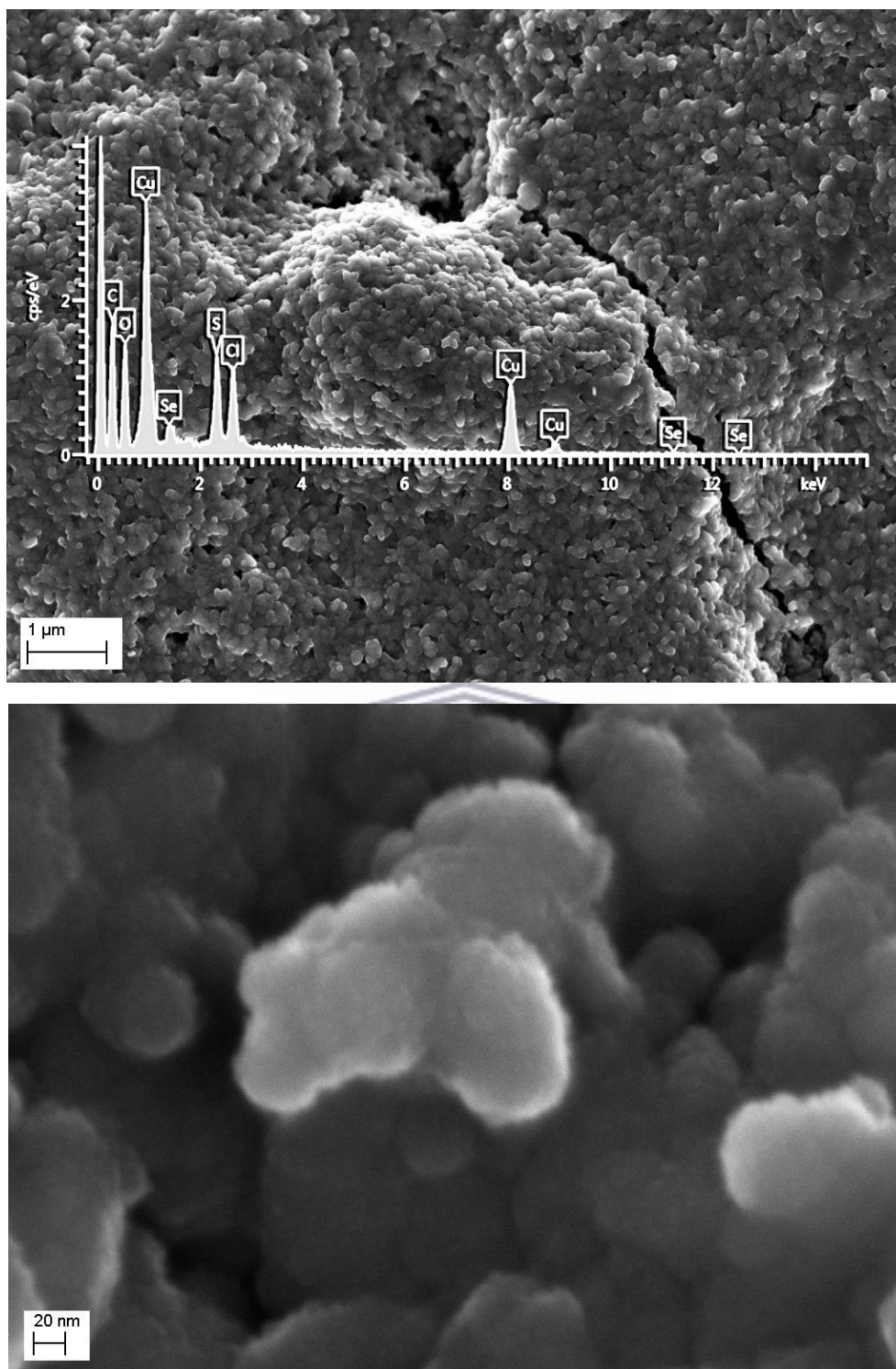


Figure 3.7 HRSEM of 3MPACuSe on carbon SPE at magnitude of 1 μm (top) and 20 nm (bottom). EDS spectra is shown in top figure.

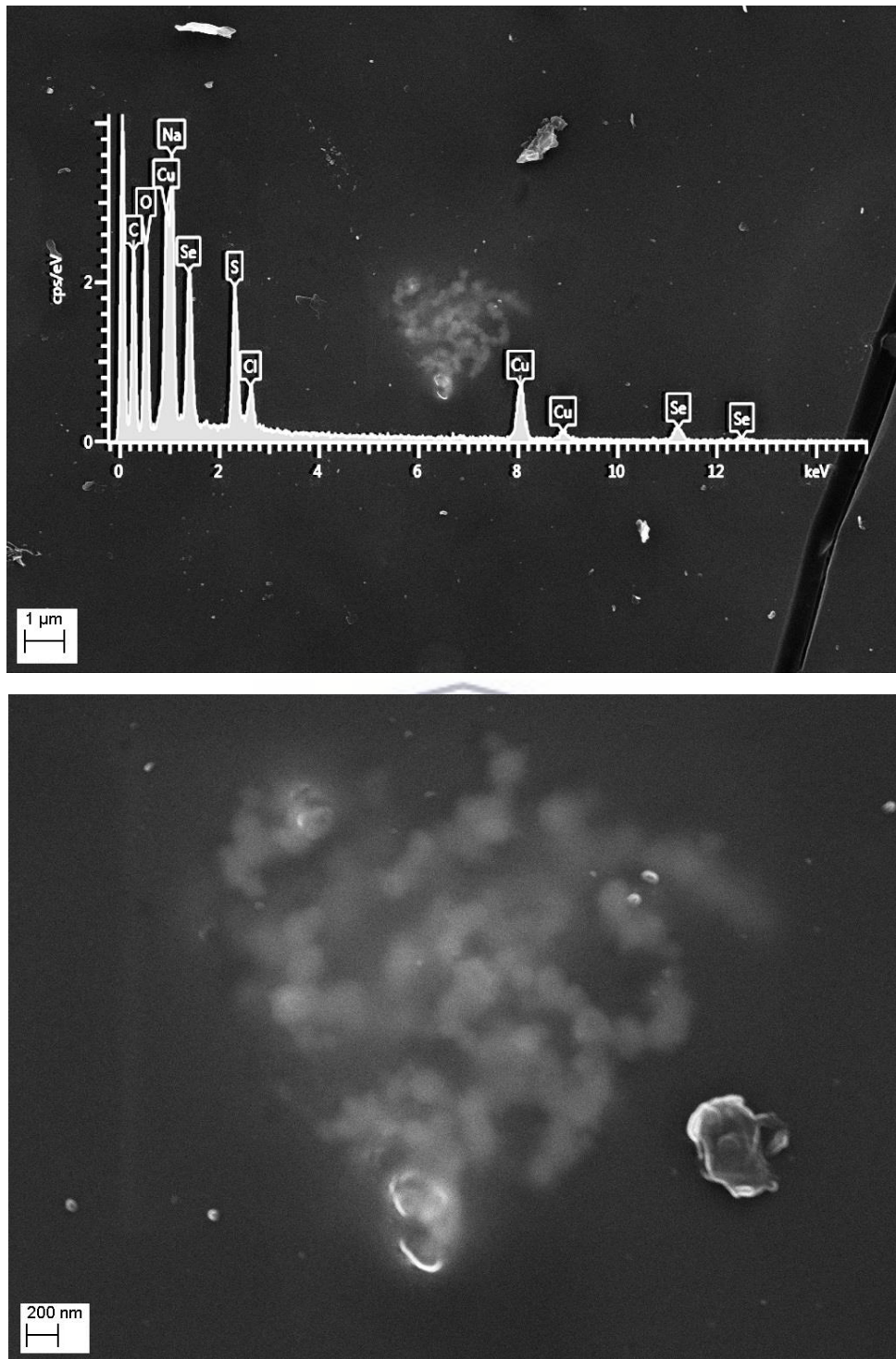
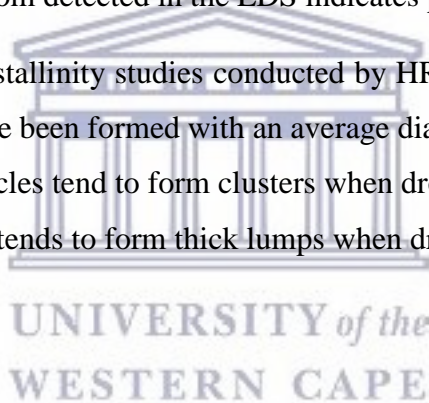


Figure 3.8 HRSEM of MSACuSe on carbon SPE at magnitude of 1 µm (top) and 20 nm (bottom). EDS spectra is shown in top figure.

The behavior of 6MHACuSe QDs on a carbon SPE (Figure 3.6) exhibited agglomerated spherical bubbles with collection of different sizes approximately 20 nm. The high abundance of copper in relation to selenium is in accordance with the stoichiometry stated by the XRD analysis (Cu_{2-x}Se). The S atoms detected in the EDS indicates presence of the capping agent (6MHA). The 3MPACuSe QDs (Figure 3.7) exhibit very similar properties as the 6MHACuSe QDs on a carbon SPE. The particles arrange in bigger clusters and the EDS confirms copper rich selenide species. Again in accordance to stoichiometry given in the XRD (Cu_{2-x}Se). Also in this case, the S atom indicate presence of the capping agent. The MSACuSe QDs (Figure 3.8) tends to cluster in bigger lumps on the carbon SPE compared to the 6MHA- and 3MPACuSe QDs. This makes it hard to get good resolution at lower magnitudes than 200 nm. However, EDS reveals a higher copper/selenium ratio compared to the other QDs. Still in agreement with the stoichiometry in the XRD for the MSACuSe QDs which was ($\beta\text{-CuSe}$). Also here, presence of the S atom detected in the EDS indicates presence of the capping agent.

The size, morphology and crystallinity studies conducted by HRTEM and HRSEM, indicates that spherical nanocrystals have been formed with an average diameter within the quantum dot size range (<10 nm). The particles tend to form clusters when drop coated on a carbon SPE. In particular the MSACuSe QDs tends to form thick lumps when dried.



3.3.1.3 Particle size, dispersion and stability in aqueous media

The particle size and size dispersion in aqueous media was investigated using small-angle x-ray scattering (SAXS) and dynamic light scattering (DLS). Furthermore, information regarding the stability of the nanoparticles in aqueous media (tendency to agglomerate) could also be obtained through these techniques. The results from the SAXS analysis was Fourier transformed using GIFT software, into a pair distance distribution function (PDDF) by volume and size distribution by number function $N_N(r)$. The results are shown in Figure 3.9 to Figure 3.11.

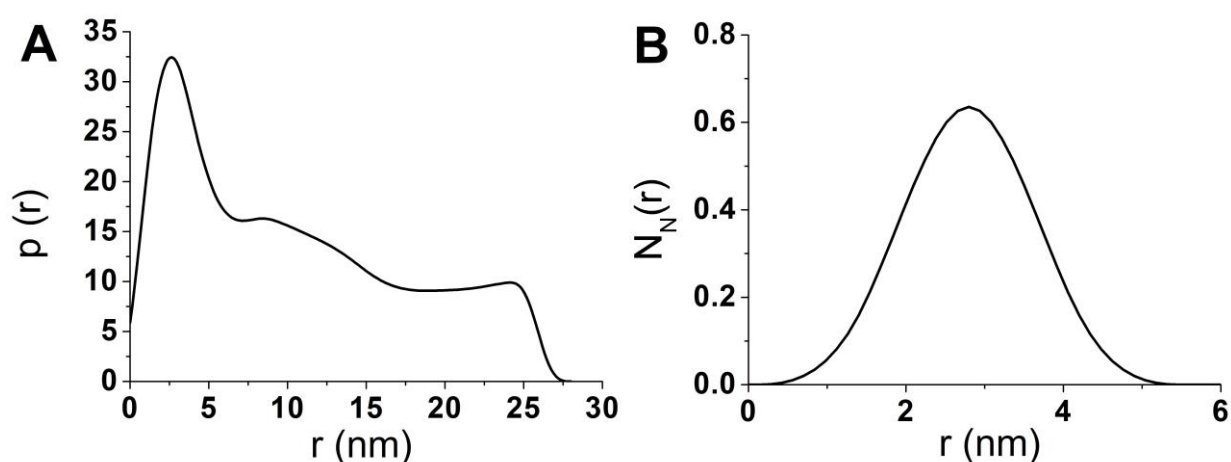


Figure 3.9 Representation of SAXS data for 6MHACuSe QDs in form of A) PDDF and B) particle radius (r) distributed by number of particles.

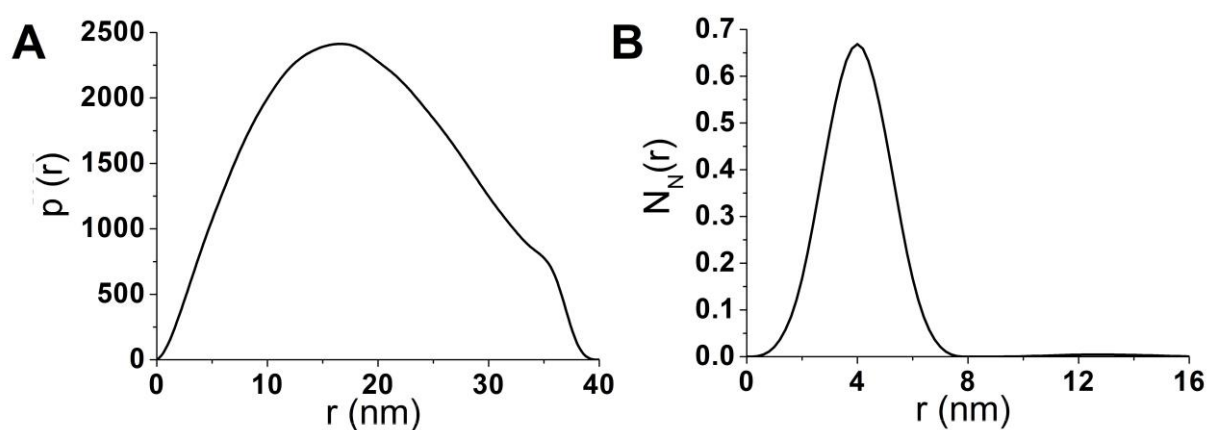


Figure 3.10 Representation of SAXS data for 3MPACuSe QDs in form of A) PDDF and B) particle radius (r) distributed by number of particles.

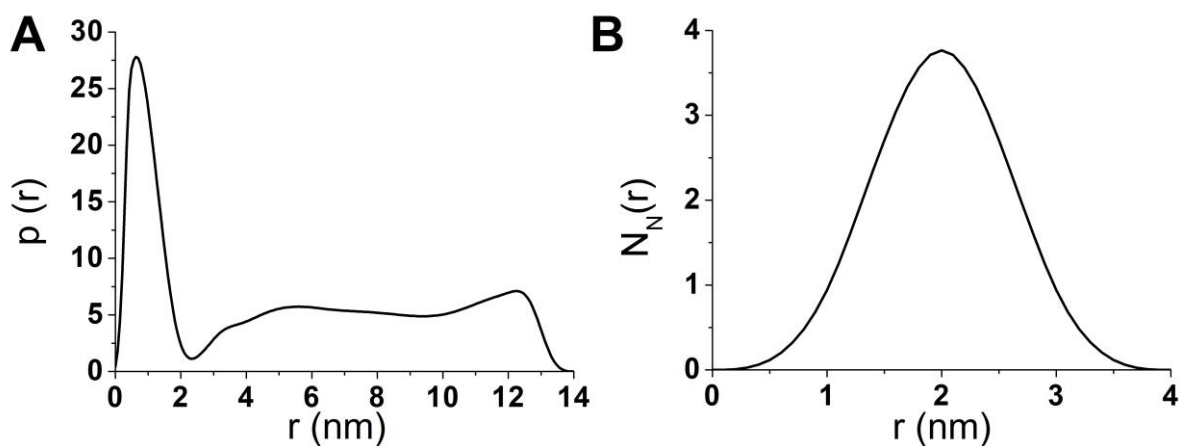


Figure 3.11 Representation of SAXS data for MSACuSe QDs in form of A) PDDF and B) particle radius (r) distributed by number of particles.

From Figure 3.9 B, it is possible to see that the 6MHACuSe QDs had an average radius of 2.8 nm giving an average diameter of 5.6 nm when diluted in aqueous media. By examining where the PDDF approaches zero ($p(r) = 0$) it is possible to extrapolate the largest particle size detected in the SAXS measurement. In Figure 3.9 A, the PDDF curve shows that the largest particles detected have a radius of 27.5 nm. Furthermore, the unregular shape of the PDDF curve indicates that there are aggregates of smaller particles sticking together in the sample. The aggregates formed particles with larger radius.[42,43] However, as the size distribution curve indicates (Figure 3.9B), the amount of particles having a large diameter is very small. Indicating that the majority of the nanocrystals formed have a diameter that falls within the range of quantum dots in aqueous media. The 3MPACuSe QDs (Figure 3.10 B) have an average particle size of 8 nm in diameter (4 nm radius) in aqueous media. Also here, the PDDF curve (figure 3.10 A) shows that the largest detected particle has the radius of 40 nm. Some irregularity towards the higher radius sizes indicates that also here aggregates has been formed of smaller particles.[42,43] However, as in the situation for the 6MHACuSe QDs, the majority of particles within the solution has an diameter below 10 nm. In the case of the MSACuSe QDs (Figure 3.11 B) the most abundant size within the particles is 4 nm in diameter when dispersed in aqueous solution. The PDDF (Figure 3.11 A) indicates aggregates and presence of larger particles of 14 nm radius.[42,43] However, also in this situation, the amount of larger particles is very low.

In addition, dynamic light scattering (DLS) was used for estimation of particle size, dispersity and stability in aqueous solution by analyzing average hydrodynamic size and zeta potential. The experiments were carried out using a zetasizer nano. The results were listed in Table 3.2 together with a summary of the average particle sizes detected using SAXS.

| Particles | Average particle diameter in solution (nm) | Average hydrodynamic diameter (nm) | Zeta potential (mV) | PDI |
|--------------|--|------------------------------------|---------------------|-------|
| 6MHACuSe QDs | 5.6 | 78.8 | -47.3 | 0.134 |
| 3MPACuSe QDs | 8 | 105.7 | -41.6 | 0.221 |
| MSACuSe QDs | 4 | 50.8 | -31.1 | 0.469 |

Table 3.2 Average particles diameter in solution (measured with SAXS), average hydrodynamic size (measured with zetasizer), Zeta potential and polydispersity index (PDI) from zetasizer..

As shown in Table 3.2, the average hydrodynamic diameter is multiple times higher compared to the diameters measured by SAXS. The polydispersity index (PDI) gives information about homogeneity of the size distribution of the particles. The PDI for the 6MHACuSe and 3MPACuSe are < 0.3 , indicating a narrow size distribution for the nanoparticles. Whereas the MSACuSe QDs have a quite high PDI value (0.469) which points to that larger aggregates of particles are forming.[44,45] The hydrodynamic size signifies “the size of a hard sphere that diffuses in the same fashion as that of the particle being measured”. [46] Giving that, the hydrodynamic size includes not only the core size of the particle but also surrounding capping agent, surfactants and unbound starting material and solvent molecules. DLS has shown to be more accurate for soft materials such as proteins. In contrast to more dense material such as metallic nanocrystals.[47] Thus, it is not surprising that the hydrodynamic diameter is bigger than the core diameter. Similar effects have been reported for other capped copper selenide nanocrystals and other nanoparticles.[14,47–49]

The zeta potential in all cases is < -30 mV, indicating potential stability of the colloidal system (< -30 mV). A large average positive ($> +30$ mV) or negative (< -30 mV) zeta potential within the particles in suspension means that they will tend to repel each other in the solution and there is no tendency to form clumps or masses.[50] In the case of the CuSe QDs, all capping agents seemed to give potentially stable nanoparticles with large negative zeta potential value. Although the high PDI value from the zetasizer and the shape of the PDDF curve indicates that there is some agglomeration occurring in the sample. Especially for MSACuSe, QDs which had a PDI of 0.469.

3.3.1.4 Molecular bonding of capping agent assessment

Further characterization by solid FTIR was performed to evaluate structural properties of the QDs. The samples were precipitated and dried prior to analysis. The results were compared with the solid FTIR of MSA powder and the results are shown in Figure 3.12.

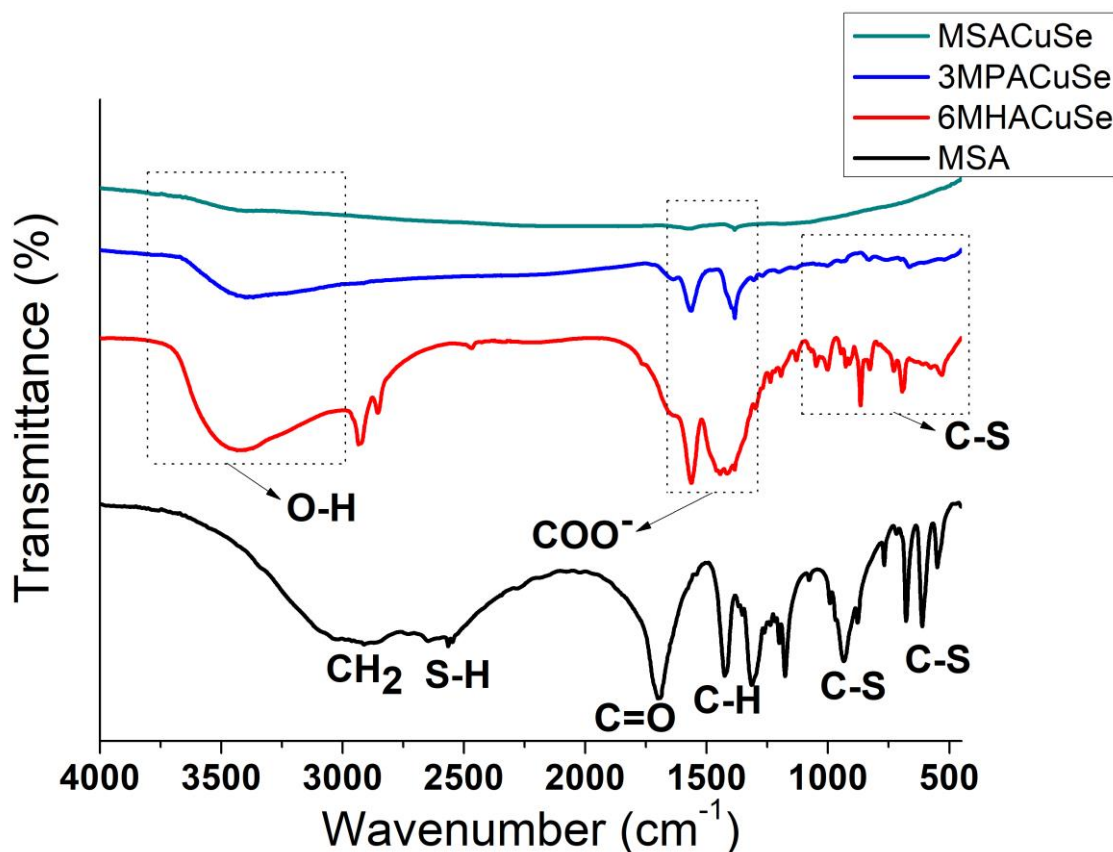


Figure 3.12 The FTIR spectra of MSACuSe QDs (green line), 3MPACuSe QDs (blue line) and 6MHACuSe QDs (red line).

The broad absorption bands around 3400 cm^{-1} was observed for all three QDs, which was attributed to the OH stretching vibrations of absorbed water molecules.[51,52] In the case of the pure MSA, SH stretches could be detected around $2550\text{--}2600\text{ cm}^{-1}$. [53] These stretches disappeared for all spectrum of the QDs, indicating successful deprotonation of the SH group and points towards reaction between the sulfur and the copper ion. Likewise, in all cases there were absorbance bands observed around $1430\text{--}1560\text{ cm}^{-1}$. These were attributed to stretching vibrations of the carboxylic acid groups. Indicating absorbance of the carboxylic capping agents on the QDs surfaces. [51,52] However, in the case of MSACuSe QDs, these absorbance peaks are small in comparison to the 3MPACuSe and 6MHACuSe QDs. Suggesting that the presence of capping agent is lower. Furthermore, stretching vibrations at $500\text{--}1000\text{ cm}^{-1}$ attributed to C-S stretching are seen in the case of 6MHACuSe and 3MPACuSe QDs. Which also points towards successful binding of the 6MHA and 3MPA capping agents on the CuSe QDs

surface.[51] However, these peaks are not observed in the case of MSACuSe QDs. Further indicating that the MSA capping agent detaches in the participation and drying process, which could contribute to the sensitivity of drying for the MSACuSe QDs. Perhaps also contributing to the higher ability to agglomerate in aqueous media.

3.3.2 Optical Properties

3.3.2.1 UV-vis absorbance and optical band gap

In order to investigate the optical properties of the synthesized QDs, room temperature UV-visible absorption measurements were made. From the absorption spectra, the direct and indirect band gap was determined by Tauc-relation (Equation 3.3).[54]

$$\alpha h\nu = A(h\nu - E_g)^n \quad (3.3)$$

Where α is the absorption coefficient, h is Planck constant, ν is the frequency, A is a constant, E_g is the energy band gap and $n = 2$ for indirect and $n=1/2$ for direct allowed electron transitions. The direct band gap energy (E_{gd}) was obtained by plotting $(\alpha h\nu)^2$ against $h\nu$ and extrapolate the linear portion of the curve $(\alpha h\nu)^2 = 0$. The indirect band gap energy (E_{gi}) was determined from $(\alpha h\nu)^{1/2}$ against $h\nu$ and extrapolation of $(\alpha h\nu)^{1/2} = 0$ from the linear region.[54] The results are shown in Figure 3.14, Figure 3.16 and Figure 3.18 for the 6MHACuSe, 3MPACuSe and MSACuSe QDs respectively. The calculated band gap values together with the wavelength for the absorption maxima's (λ_{max}) were listed in Table 3.3.

| Particles | λ_{max} (nm) | E_{gd} (eV) | E_{gi} (eV) |
|--------------|----------------------|---------------|---------------|
| 6MHACuSe QDs | 435 | 2.44 | 1.77 |
| 3MPACuSe QDs | 400 | 2.98 | 1.79 |
| MSACuSe QDs | 340 | 3.26 | 2.83 |

Table 3.3 The wavelength of the absorption maxima (λ_{max}) for the 6MHACuSe, 3MPACuSe and MSACuSe QDs absorption bands and the direct (E_{gd}) and indirect (E_{gi}) band gap values.

The absorption spectra for 6MHACuSe QDs is illustrated in Figure 3.13 together with the absorption spectra for the precursors used in the synthesis, and Figure 3.14 together with corresponding direct and indirect band gap plots.

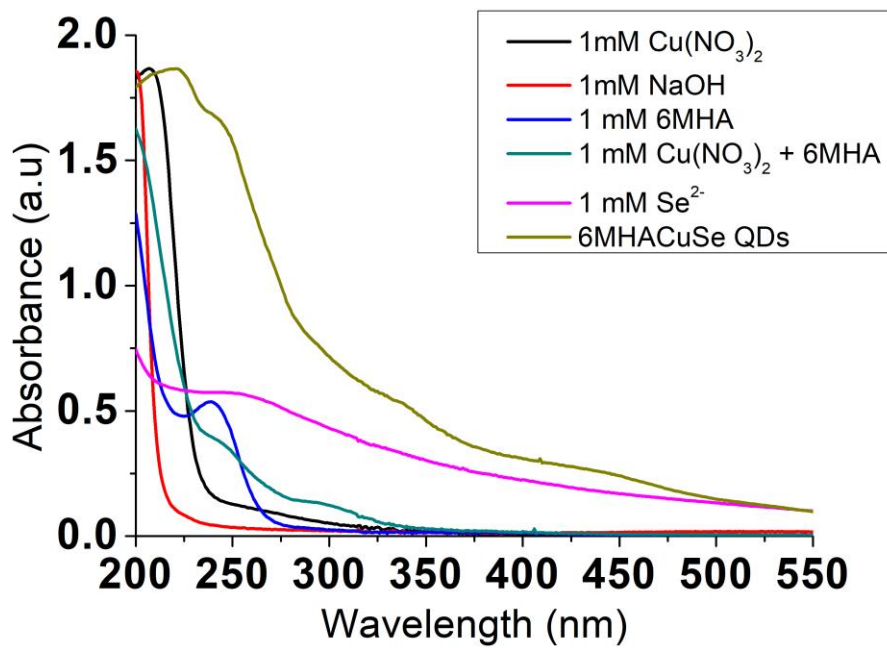


Figure 3.13 Absorbance spectra of 6MHACuSe QDs (green line) and 1 mM aqueous solutions of Cu(NO₃)₂ (black line), NaOH (red line), 6MHA (deep blue line), Cu(NO₃)₂ and 6MHA mixture (light blue line), Se²⁻ (pink line).

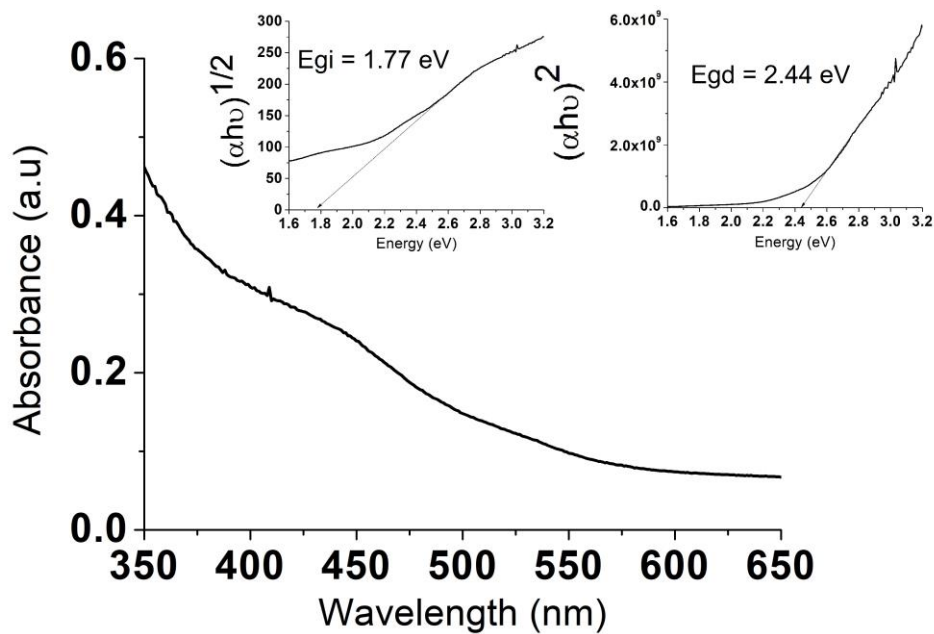


Figure 3.14 6MHACuSe QDs absorption band with left insert corresponding to the direct band gap plot and right insert corresponding to the indirect band gap plot.

The absorption spectra for the 6MHACuSe QDs (Figure 3.13) shows absorption bands at 220, 245, 330 and 435 nm, respectively. Through analyzing the absorption spectra of the precursors, the bands at 220 and 245 nm could be assigned to the transitions caused by $\text{Cu}(\text{NO}_3)_2$ and 6MHA precursors respectively. In the precursor mixture of $\text{Cu}(\text{NO}_3)_2$ and 6MHA, an absorption band appeared at 300 nm. This band can be explained by the ligand to metal charge transfer (LMCT) transition from $\text{S}(\sigma) \rightarrow \text{Cu}^{2+}$, between the copper and the sulfur atom from the capping agent.[55–58] Therefore, the band at 330 nm in the 6MHACuSe QDs could be assigned as the LMCT between the copper in the QDs and the capping agent, with a slight shift towards lower energies. Lastly, the band at 435 nm only appears for the 6MHACuSe QDs mixture and could be assigned as the absorption of the actual quantum dots formed. The 6MHACuSe QDs had a direct band gap $E_{gd} = 2.44$ eV and an indirect band gap $E_{gi} = 1.77$ eV. The band gap of the bulk copper selenide is not well defined because of its many stoichiometric form. Values has been reported of direct band gap energies of 2.1-2.3 eV and indirect band gap energies of 1.2-1.4 eV.[14,59] The blue shift of the band gap from the bulk material is caused by the quantum confinement effect on the nanoparticles. The optical properties of QDs is due to the excitement of electrons from the valance band to the conduction band, with the energy difference being known as the band gap energy. [3] When the electron is excited from the conduction band to the valence band, a hole is left in the valence band. The electron and its associated hole can be hold together by electrostatic attraction, forming an exciton. The distance between the electron and associated hole is known as exciton Bohr radius. When the QDs diameter is smaller than the exciton Bohr radius, quantum confinement occurs causing a transition from continuous to discrete energy levels. The energy levels of the valence and conduction band within the QD becomes quantized and the energy values can be directly related to the particle size.[60,61]

Figure 3.15 illustrates the absorption spectra obtained for 3MHACuSe QDs together with the absorption spectra for the precursors used in the synthesis. Figure 3.16 shows the 3MPACuSe QDs absorption spectra together with corresponding direct and indirect band gap plots.

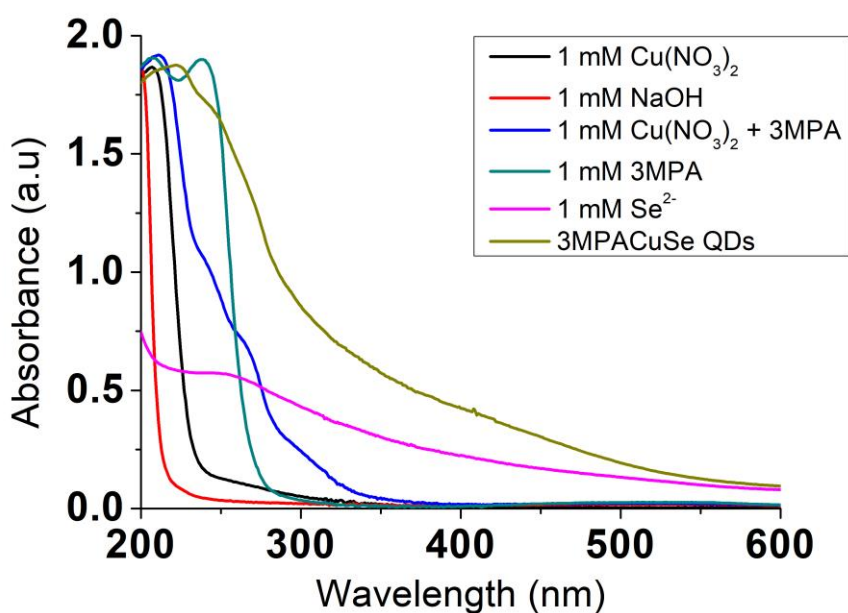


Figure 3.15 Absorbance spectra of 3MPACuSe QDs (green line) and 1 mM aqueous solutions of Cu(NO₃)₂ (black line), NaOH (red line), Cu(NO₃)₂ and 3MPA mixture (deep blue line), 3MPA (light blue line), Se²⁻ (pink line).

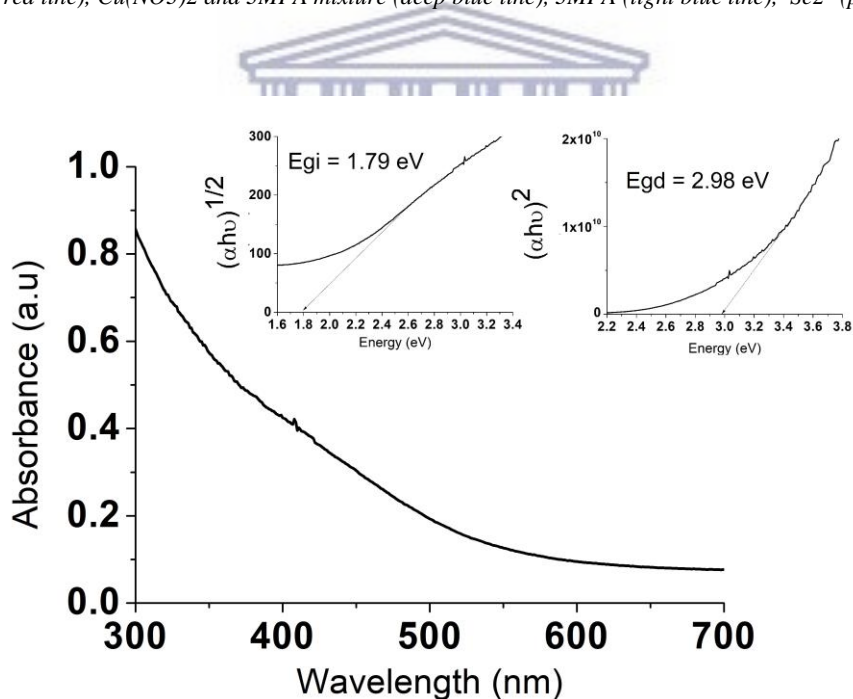


Figure 3.16 3MPACuSe QDs absorption band with left insert corresponding to the direct band gap plot and right insert corresponding to the indirect band gap plot.

In the absorption spectra for 3MPACuSe QDs (Figure 3.15) bands between 225-280 nm could likewise be assigned to transitions caused by the Cu(NO₃)₂ and 3MPA precursors. A weak band at 320 nm could be attributed to the LMCT between the copper and 3MPA capping agent. The band at 400 nm was attributed to the formed 3MPACuSe QDs. The band gaps were calculated to $E_{gd} = 2.98$ eV and $E_{gi} = 1.79$ eV. This shows a blue shift from the bulk material.[14]

The absorption spectra for the MSACuSe QDs were illustrated in Figure 3.17, together with the absorption spectra for the precursors used in the synthesis. Figure 3.18 illustrates the MSACuSe QDs absorption spectra and corresponding band gap plots.

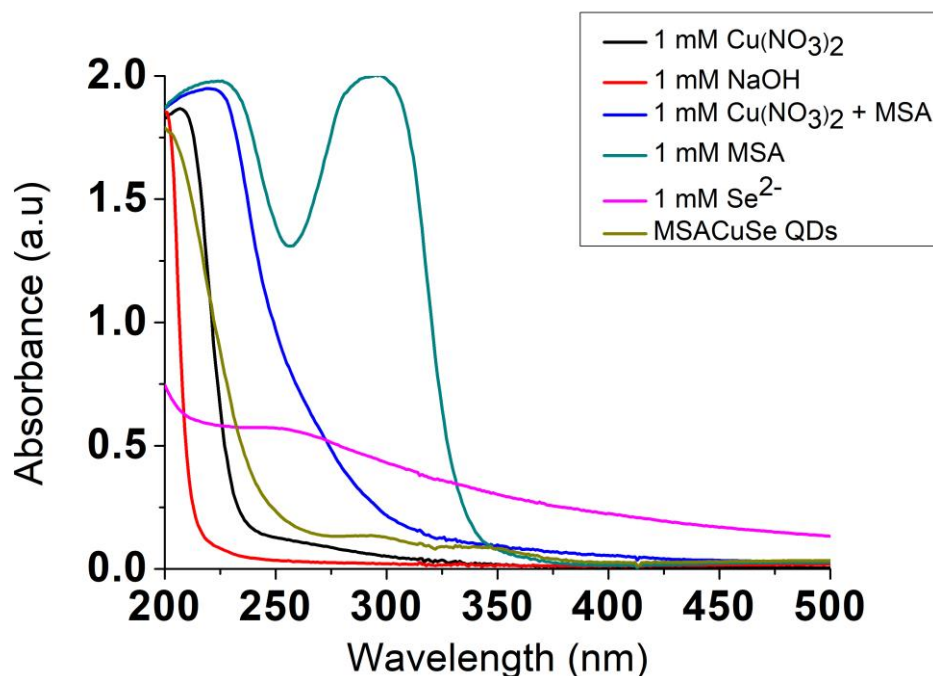


Figure 3.17 Absorbance spectra of MSACuSe QDs (green line) and 1 mM aqueous solutions of $\text{Cu}(\text{NO}_3)_2$ (black line), NaOH (red line), $\text{Cu}(\text{NO}_3)_2$ and MSA mixture (deep blue line), MSA (light blue line), Se^{2-} (pink line).

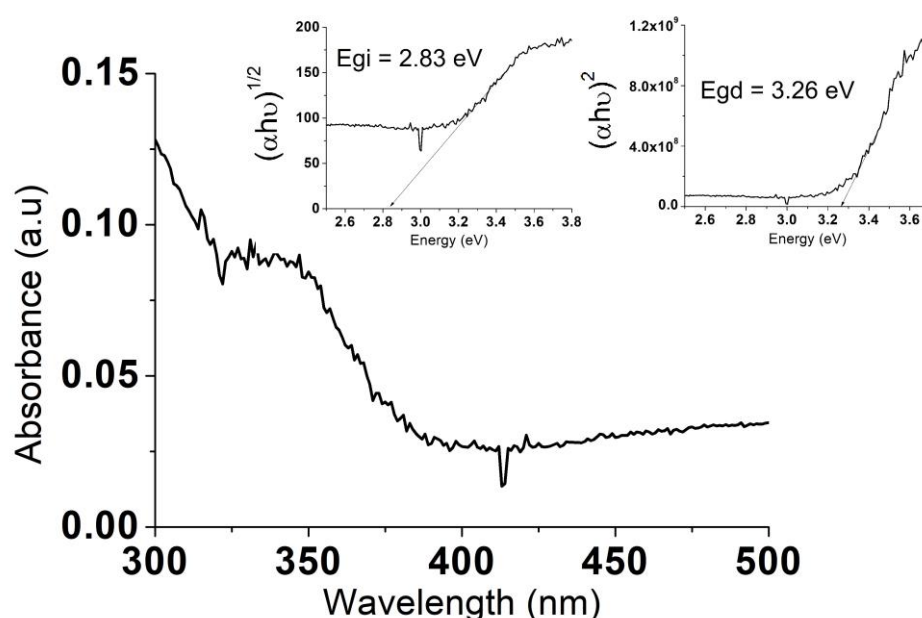


Figure 3.18 MSACuSe QDs absorption band with left insert corresponding to the direct band gap plot and right insert corresponding to the indirect band gap plot.

Also for the MSACuSe QDs (Figure 3.17) a rather distinct absorption band at 290 nm could be detected, assigned to the LMCT between the copper and MSA capping agent. Furthermore, the

absorption band at 340 nm was assigned to the formation of MSACuSe QDs. The band gaps were calculated to $E_{gd} = 3.26$ and $E_{gi} = 2.83$. The big blue shift from the MSACuSe QDs compared to the 6MHACuSe and 3MPACuSe QDs could be explained by two factors. Firstly, the stoichiometry differ for the MSACuSe QDs which mainly consisted of β -CuSe. The optical properties of the material have shown to slightly vary with the stoichiometry.[59] Secondly, the MSACuSe QDs were shown to have the lowest particle diameter when dispersed in aqueous media. The particle size affects the band gap to shift towards higher energy values, which would explain the difference in band gap values.[60,61] Further confirming the results from the SAXS and DLS measurements.

3.3.2.2 Photoluminescence

The photoluminescent properties of the CuSe QDs were investigated by exciting the sample with light of 398 nm. The emission spectra together with corresponding excitation spectra for the QDs are shown in Figure 3.19 to Figure 3.21.

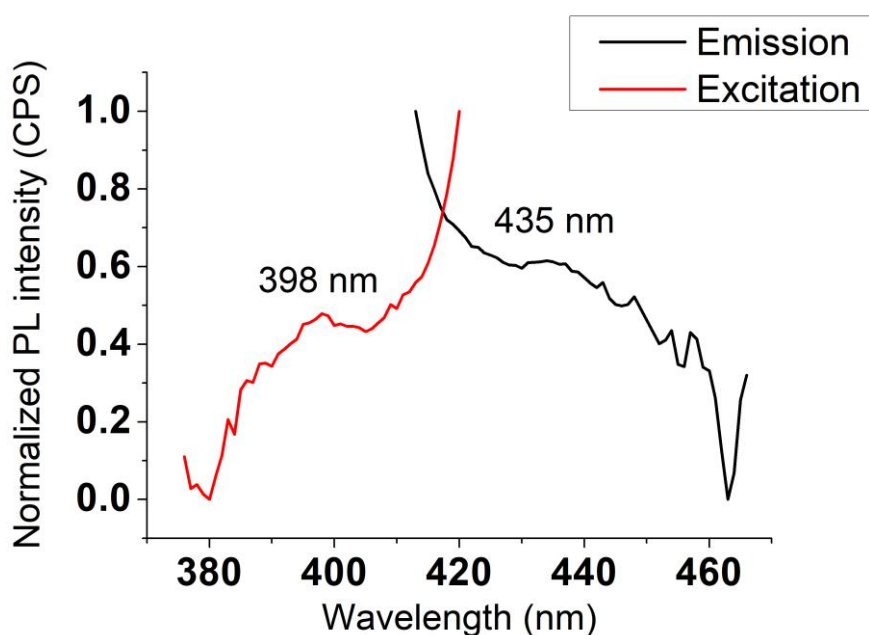


Figure 3.19 The excitation spectra (red line) and the emission spectra (black line) of 6MHACuSe QDs.

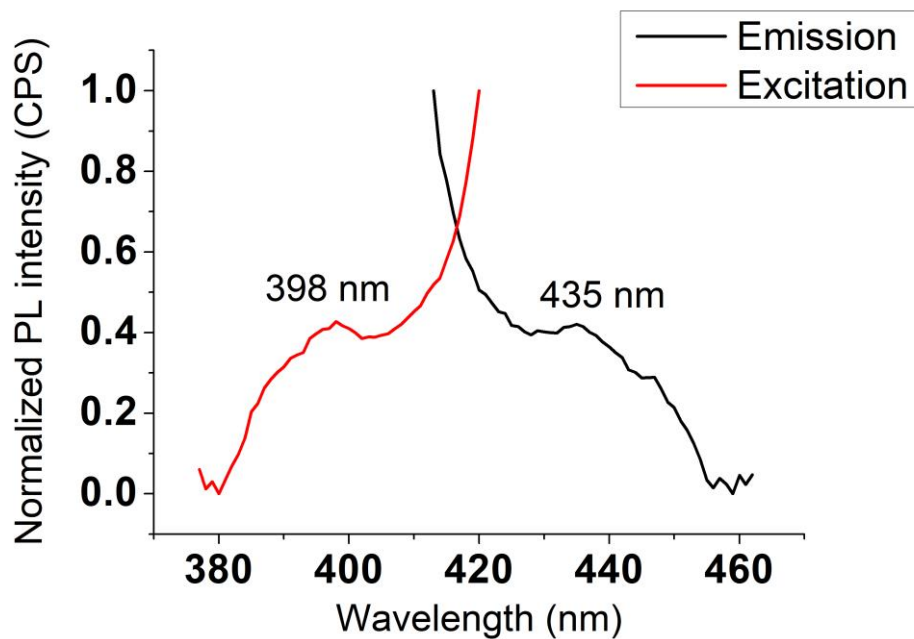


Figure 3.20 The excitation spectra (red line) and the emission spectra (black line) of 3MPACuSe QDs.

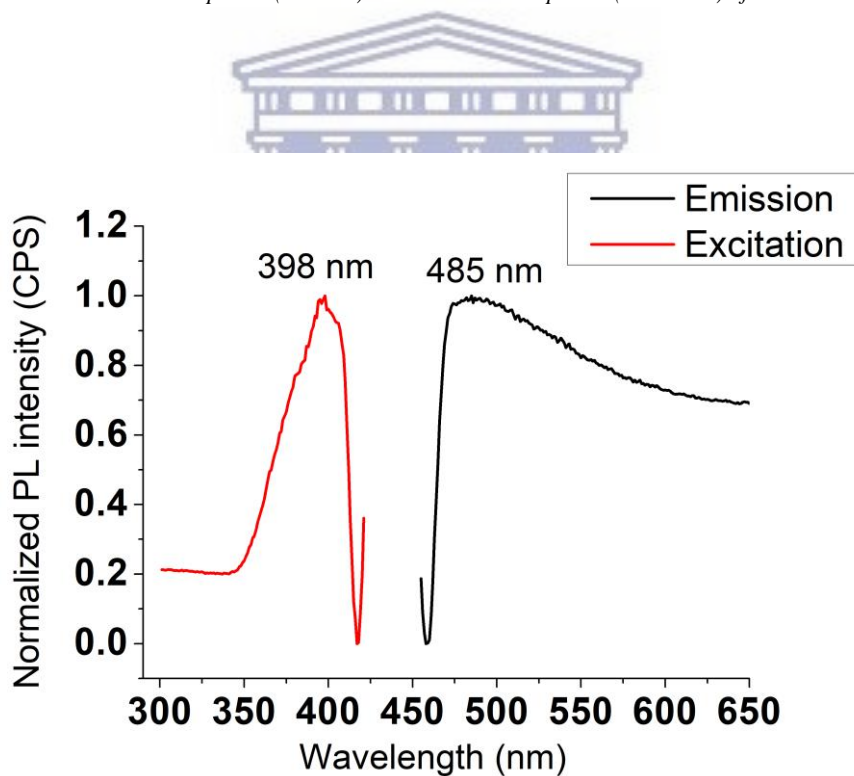


Figure 3.21 The excitation spectra (red line) and the emission spectra (black line) of MSACuSe QDs.

In the emission spectra of 6MHACuSe (Figure 3.19) and 3MPACuSe (Figure 3.20) QDs a weak emission peak could be detected at 435 nm. Whereas in the case of the MSACuSe QDs (Figure 3.21) an emission peak at 485 nm. The bands arise from electronic transitions within the electronic band gap of the CuSe QDs exciton. The emission wavelength is consistent with

earlier obtained emission wavelengths for CuSe QDs and nanocrystals.[13,24,33] The measurements shows that the synthesized QDs are capable of emitting light of wavelengths in the visible region. The low intensity of the fluorescence peaks can be explained by quenching of the capping agent on the surface. Trung and co-workers showed that CdSe/ZnS QDs, capped with the thiol consisting molecule cysteamine, had a reduced fluorescence intensity compared to uncapped QDs.[62] In a review article by Xing and co-workers, the authors discussed the generally lower fluorescence emission intensity amongst water soluble QDs. Though with the advantage of the QDs being biocompatible.[34]



3.3.3 Electrochemical properties

The electrochemical behavior of the CuSe QDs when immobilized on a bare gold (Au) electrode was investigated using cyclic voltammetry at scan rates (v) varying from 10-100 mV s^{-1} . All the experiments were carried out in 0.1 M phosphate buffer (pH 7.40) with a potential window of -800 – 800 mV starting with an anodic sweep from -800 mV. The resulting cyclic voltammograms are illustrated in Figure 3.22 to Figure 3.27.

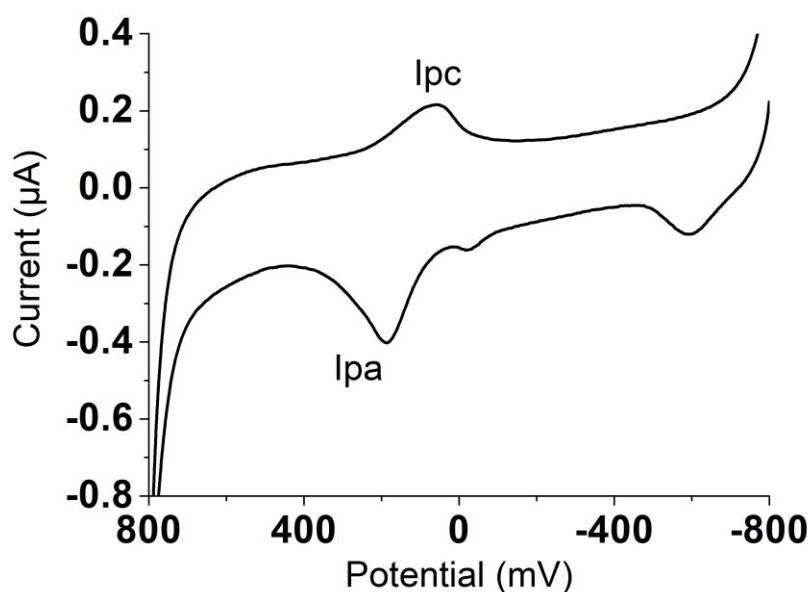


Figure 3.22 The cyclic voltammograms of 6MHACuSe QDs immobilized on a bare Au electrode at 25 mVs^{-1} .

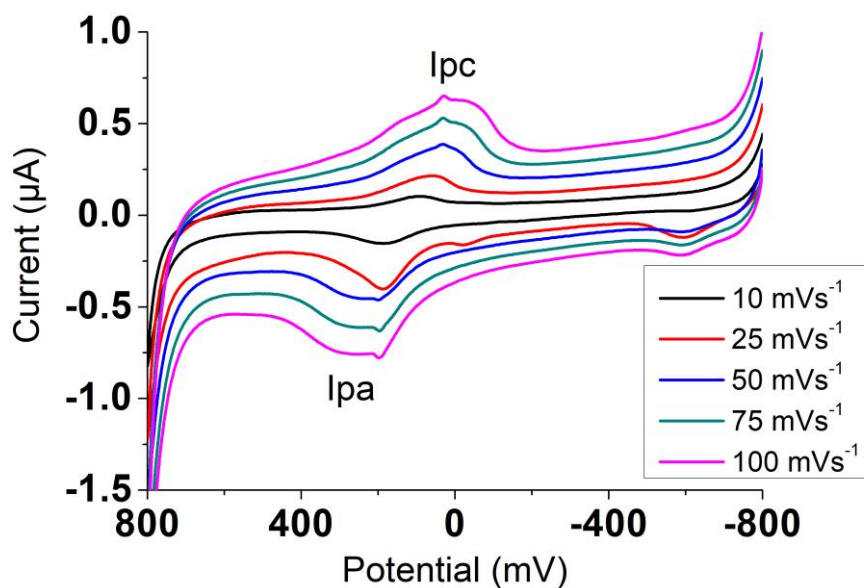


Figure 3.23 The cyclic voltammograms of 6MHACuSe QDs immobilized on a bare Au at multiple scan rates varying from 10-100 mVs^{-1} .

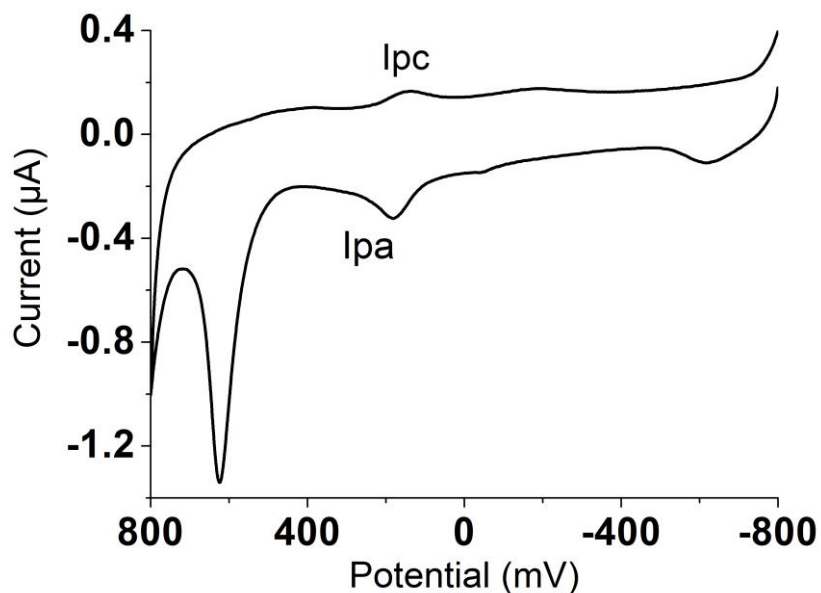


Figure 3.24 The cyclic voltammograms of 3MPACuSe QDs immobilized on a bare Au electrode at 25 mVs^{-1} .

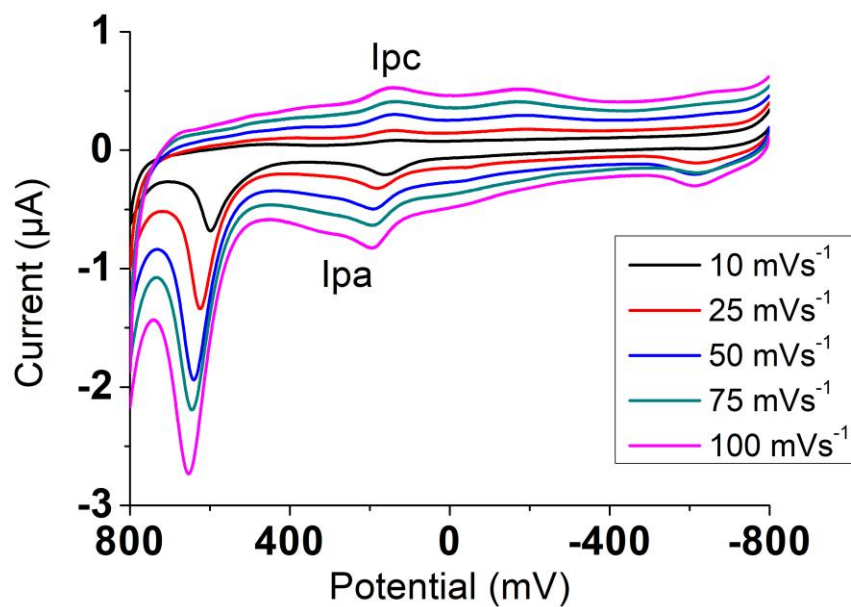


Figure 3.25 The cyclic voltammograms of 3MPACuSe QDs immobilized on a bare Au electrode at multiple scan rates varying from 10 - 100 mVs^{-1} .

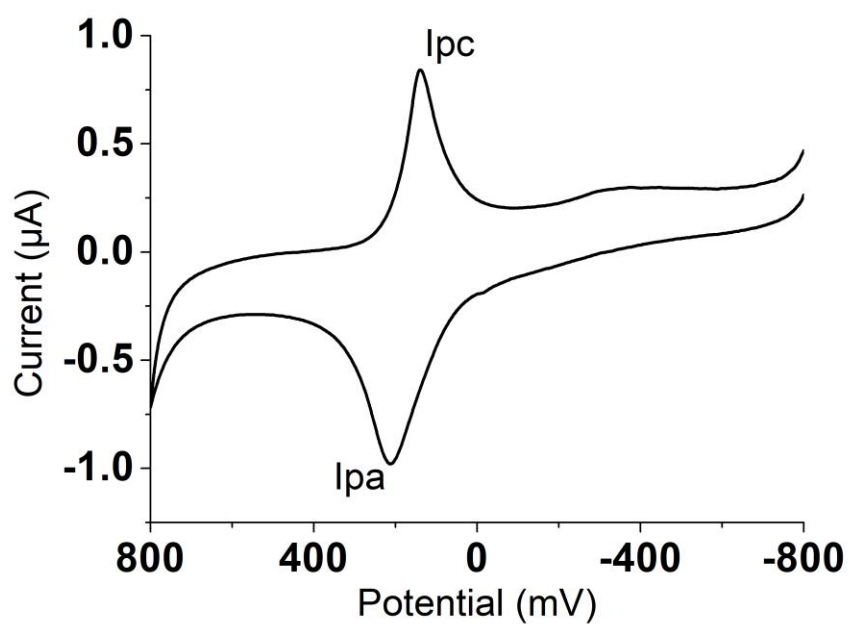


Figure 3.26 The cyclic voltammograms of MSACuSe QDs immobilized on a bare Au electrode at 25 mVs^{-1} .

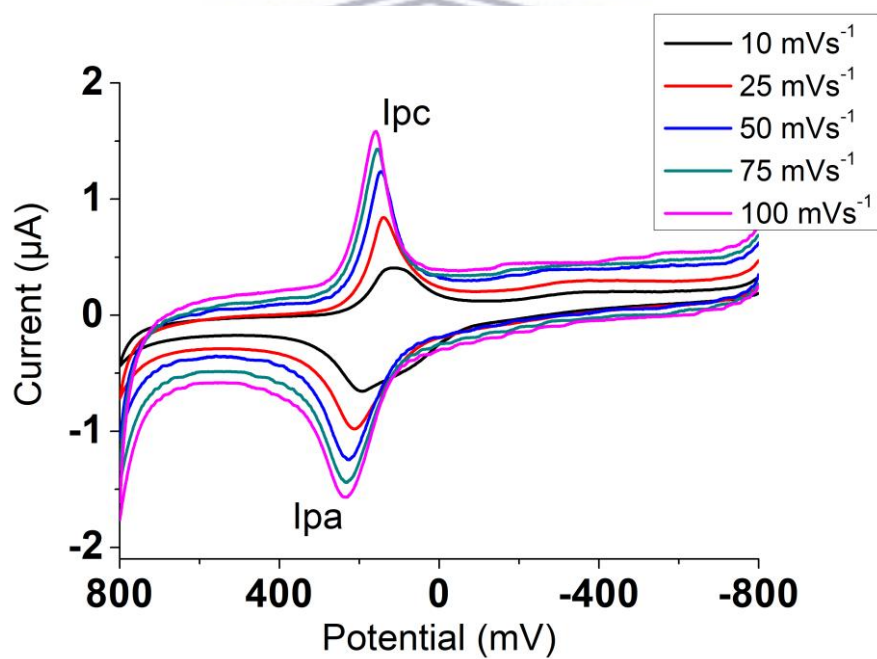
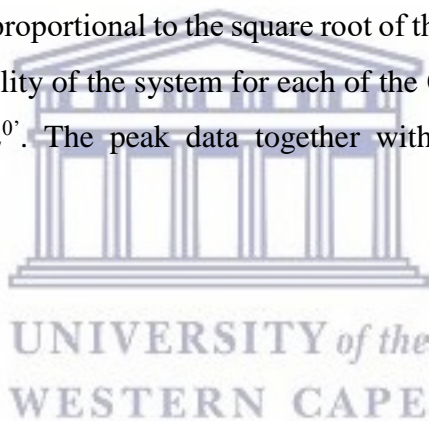


Figure 3.27 The cyclic voltammograms of MSACuSe QDs immobilized on a bare Au electrode at multiple scan rates varying from $10\text{-}100 \text{ mVs}^{-1}$.

In Figure 3.22 to Figure 3.27 it is possible to see that the quantum dots exhibit oxidation (I_{pa}) and reduction (I_{pc}) peak currents that are connected through a redox reaction. The I_{pa} and I_{pc} occur at oxidation potentials (E_{pa}) within the range 229 -160 mV and reduction potentials (E_{pc}) within the range of 159-30 mV. For reversible systems it is possible to estimate the number of electrons involved in the transfer through Equation 3.4.[63]

$$\Delta E = \frac{59}{n} \quad (3.4)$$

Where n represents the number of electrons and $\Delta E = E_{pa} - E_{pc}$. The system is considered completely reversible if the absolute value of the ratios between $I_{pc}/I_{pa} = 1$, $\Delta E = 59$ mV, $E^{0'}$ (the formal potential) is positions midway between E_{pa} and E_{pc} ($E^{0'} = (E_{pa} + E_{pc})/2$) and independent of scan rate, I_p is proportional to the square root of the scan rate ($v^{1/2}$) and Equation 3.4 is applicable. The reversibility of the system for each of the QDs was investigated through calculation of I_{pc}/I_{pa} , ΔE , $E^{0'}$. The peak data together with the calculated factors were summarized in Table 3.4.[63]



| 6MHACuSe QDs | | | | | | | | |
|---------------------------|----------------------|----------------------|----------------------|----------------------|---------|---------------------|----------------------------------|------|
| v (mV s ⁻¹) | I _{pa} (μA) | I _{pc} (μA) | E _{pa} (mV) | E _{pc} (mV) | ΔE (mV) | E ⁰ (mV) | I _{pc} /I _{pa} | n |
| 10 | -0.08119 | 0.07195 | 178 | 96 | 82 | 137 | 0.89 | NA* |
| 25 | -0.2487 | 0.1079 | 188 | 62 | 126 | 125 | 0.43 | |
| 40 | -0.1743 | 0.1266 | 193 | 38 | 155 | 115.5 | 0.73 | |
| 50 | -0.1946 | 0.1371 | 199 | 33 | 166 | 116 | 0.70 | |
| 60 | -0.2232 | 0.1482 | 197 | 34 | 163 | 115.5 | 0.66 | |
| 75 | -0.2744 | 0.166 | 196 | 31 | 165 | 113.5 | 0.60 | |
| 90 | -0.3065 | 0.1589 | 195 | 32 | 163 | 113.5 | 0.52 | |
| 100 | -0.3289 | 0.1561 | 198 | 30 | 168 | 114 | 0.47 | |
| 3MPACuSe QDs | | | | | | | | |
| 10 | -0.1136 | 0.04442 | 159 | 131 | 28 | 145 | 0.39 | NA* |
| 25 | -0.1625 | 0.0666 | 180 | 134 | 46 | 157 | 0.41 | |
| 40 | -0.1039 | 0.0839 | 185 | 137 | 48 | 161 | 0.81 | |
| 50 | -0.1701 | 0.1033 | 190 | 137 | 53 | 163.5 | 0.61 | |
| 60 | -0.152 | 0.1008 | 183 | 133 | 50 | 158 | 0.66 | |
| 75 | -0.1863 | 0.09034 | 189 | 144 | 45 | 166.5 | 0.48 | |
| 90 | -0.2141 | 0.09487 | 190 | 146 | 44 | 168 | 0.44 | |
| 100 | -0.2243 | 0.1085 | 192 | 149 | 43 | 170.5 | 0.48 | |
| MSACuSe QDs | | | | | | | | |
| 10 | -0.4411 | 0.3821 | 189 | 117 | 72 | 153 | 0.87 | 0.82 |
| 25 | -0.6691 | 0.7873 | 210 | 139 | 71 | 174.5 | 1.18 | 0.83 |
| 40 | -0.8647 | 1.029 | 220 | 143 | 77 | 181.5 | 1.19 | 0.77 |
| 50 | -0.9842 | 1.117 | 225 | 147 | 78 | 186 | 1.13 | 0.76 |
| 60 | -1.002 | 1.159 | 226 | 152 | 74 | 189 | 1.16 | 0.80 |
| 75 | -1.107 | 1.254 | 232 | 155 | 77 | 193.5 | 1.13 | 0.77 |
| 90 | -1.159 | 1.297 | 235 | 157 | 78 | 196 | 1.12 | 0.76 |
| 100 | -1.108 | 1.29 | 229 | 159 | 70 | 194 | 1.16 | 0.84 |

Table 3.4 Shows the values of the oxidation and reduction peak current (I_{pa} and I_{pc} respectively), the oxidation and reduction peak potential (E_{pa} and E_{pc}), ΔE (i.e. E_{pa} – E_{pc}), the formal potential E⁰, the absolute value of the I_{pc}/I_{pa} ratio and the number of electrons n, at different scan rates (v). *NA = not applicable

The redox reaction corresponding to the I_{pa} and I_{pc} peaks for the 6MHACuSe and 3MPACuSe QDs, was considered to be quasi-reversible. Thus the number of electrons could not be calculated using Equation 3.4. The redox reaction of the MSACuSe QDs was concerned to be completely reversible. Through Equation 3.4 the value of n was estimated to n ≈ 1. The same number of electrons were assumed to be involved in the 6MHACuSe and 3MPACuSe QDs electron transfer.

From the cyclic voltammetry, a shift in current peak potential could be observed. In the case of the 6MHACuSe QDs the oxidation current peak (I_{pa}) shifts towards higher potential values

from $E_{pa} = 178$ mV to $E_{pa} = 198$ mV. In contrast, the reduction current peak I_{pc} shift towards lower potential values, from $E_{pc} = 96$ mV to $E_{pc} = 30$ mV. This separation in ΔE values for the redox reaction caused by the 6MHACuSe QDs is due to the quasi-reversible nature of the reaction. In a quasi-reversible reaction, the $\Delta E/n$ ratio is > 59 mV, and is increasing with increasing scan rates. Also for the 3MPACuSe QDs, the $\Delta E/n$ ratio shows a shift towards higher values with increase in scan rate. However, in the case of the MSACuSe QDs, the ΔE value does not have a net shift towards higher potential values indicating that the reaction is of reversible nature.[64] Furthermore, the cyclic voltammogram of the 6MHACuSe QDs (Figure 3.22) also shows a small oxidation peak at $E_{pa} = -592$ mV. Also for 3MPACuSe (Figure 3.24) there is a distinct oxidation peak visible at around $E_{pa} = 624$ mV. To further understand exactly which components of the QDs that are being subject to the oxidation/reduction reaction, the electrochemical behavior of the QDs precursor was investigated. Cyclic voltammetry of the precursors: $\text{Cu}(\text{NO}_3)_2$, reduced selenium (Se^{2-}) and the capping agents 6MHA, MSA and 3MPA, was investigated with the same conditions as the QDs (i.e. bare Au electrode in 0.1 M phosphate buffer pH 7.40). The phosphate buffer was spiked with aqueous solutions of the precursors. The resulting voltammograms are shown in Figure 3.28 to Figure 3.32.

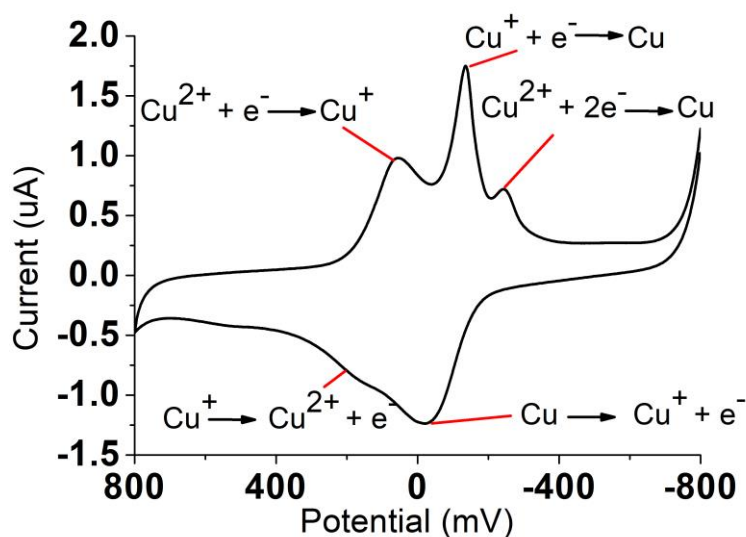


Figure 3.28 Cyclic voltammograms of 4 mM $\text{Cu}(\text{NO}_3)_2$ diluted in 0.1 M phosphate buffer (pH 7.40) measured with bare gold electrode with proposed reaction mechanisms responsible for the current peaks.

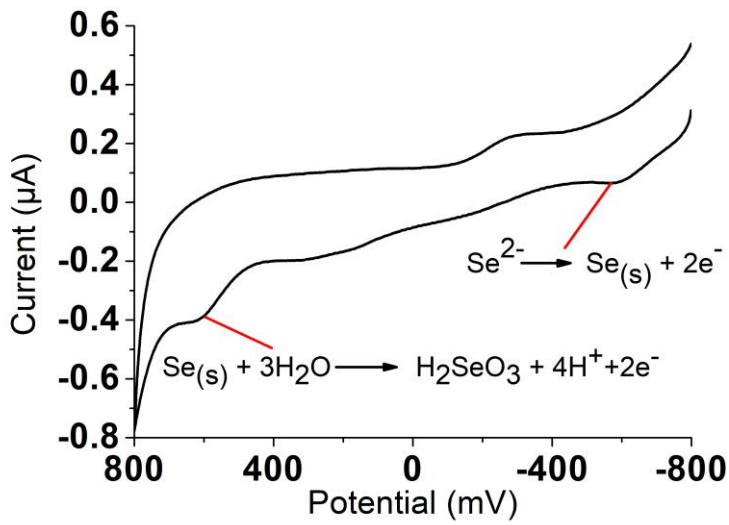


Figure 3.29 Cyclic voltammograms of 2 mM Se^{2-} (right) diluted in 0.1 M phosphate buffer (pH 7.40) measured with bare gold electrode with proposed reaction mechanisms responsible for the current peaks.

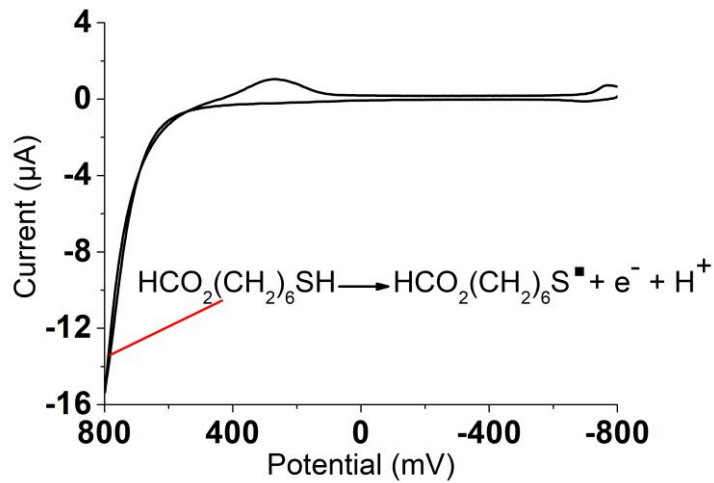


Figure 3.30 Cyclic voltammogram measured with bare Au electrode of 32 mM 6MHA diluted in 0.1 phosphate buffer (pH 7.40) with proposed reaction mechanisms responsible for the current peaks.

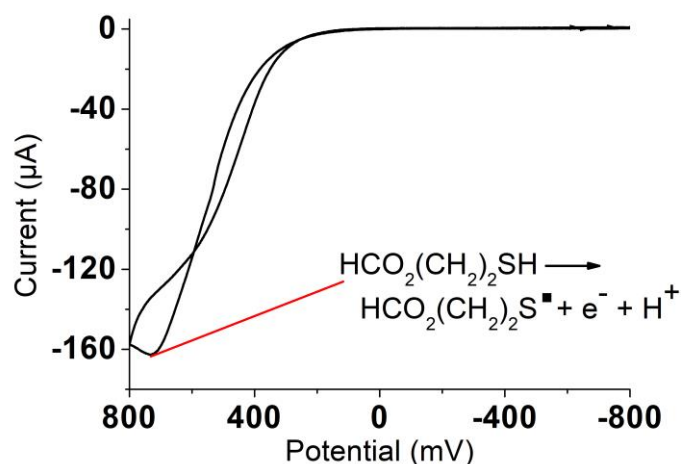


Figure 3.31 Cyclic voltammogram measured with bare Au electrode of 32 mM 3MPA diluted in 0.1 phosphate buffer (pH 7.40) with proposed reaction mechanisms responsible for the current peaks.

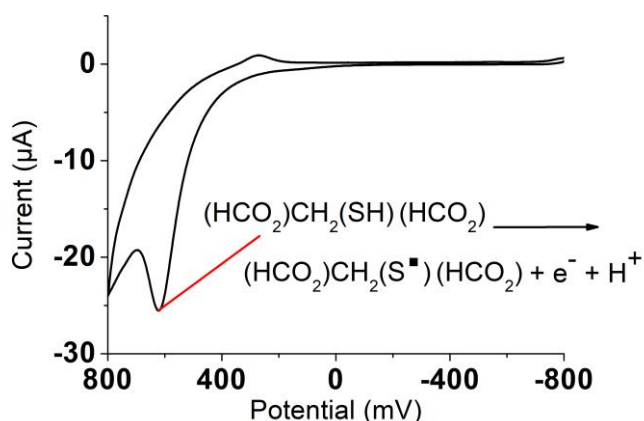
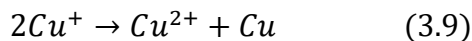
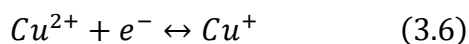


Figure 3.32 Cyclic voltammogram measured with bare gold electrode of 32 mM MSA diluted in 0.1 phosphate buffer (pH 7.40) with proposed reaction mechanisms responsible for the current peaks.

The electrochemical behavior of Cu^{2+} in phosphate buffer solution is illustrated in Figure 3.28. The electrochemical characteristics of copper in aqueous media has been well characterized and is demonstrated in Equation 3.6 to Equation 3.8. In absence of complexing agents stabilizing Cu^+ , disproportionation occurs in accordance to of Equation 3.9.[65,66]

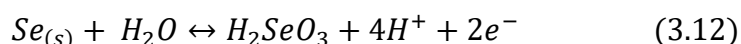


In the presence of complexing agents, Cu^+ is stable in aqueous solution. Thus, Cu^{2+} may undergo a two-step electron transfer from Cu^{2+} to Cu . This causes the $\text{Cu}^{2+}/\text{Cu}^+$ redox reaction to be visible in the cyclic voltammetry as two redox peaks, which is illustrated in Figure 3.28. The oxidation peak occurring at -22 mV was assigned to the one electron oxidation of Cu to Cu^+ . Whereas the oxidation at 180 mV was assigned to the oxidation of Cu^+ to Cu^{2+} . Two reduction peaks were observed at 55 mV and -135 mV, respectively. The first reduction peak was attributed to the reduction of Cu^{2+} to Cu^+ and the second reduction peak was ascribed to further reduction of Cu^+ to Cu . In addition, a weak reduction peak at -245 mV was assigned to the two electron transfer reduction of Cu^{2+} to Cu .

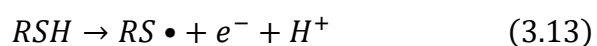
Figure 3.29 shows the cyclic voltammogram of Se^{2-} in phosphate buffer. The reaction mechanism for the reduction of selenium using NaBH_4 , is illustrated in Equation 3.10.



Where NaHSe corresponds to the selenium being in 2- reduced form. Se^{2-} can thereafter occur in equilibrium states in aqueous solutions.[53,67] The reactions occurring for the cyclic voltammogram (Figure 3.29) was assigned to the reactions illustrated in Equation 3.11 (for the peak occurring at -585 mV) and Equation 3.12 (for the oxidation peak occurring at 630 mV).

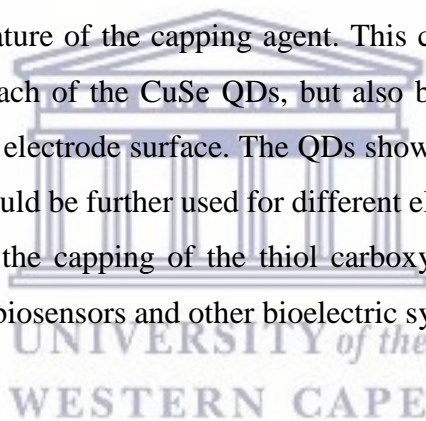


The capping agent interaction with the gold electrode was also investigated. The oxidation current visible in the cyclic voltammograms for the capping agents (Figure 3.30 to Figure 3.32) at -600 mV to > 800 mV, could be attributed to the oxidation of the thiol group (RSH) to form thiol radicals ($\text{RS}\cdot$). Which could thereafter react to form disulphides.[68,69] The proposed mechanism is shown in Equation 3.13 and Equation 3.14.



The oxidation and reduction current peaks occurring for the 6MHACuSe QDs and 3MPACuSe QDs is possible to connect to the quasi-reversible redox reaction of $\text{Cu}^+ \leftrightarrow \text{Cu}^{2+} + \text{e}^-$, of the copper species within the QDs. The average formal potential for the reaction was calculated to $E^{0'} \approx 120$ mV for 6MHACuSe QDs and $E^{0'} \approx 159$ mV for the 3MPACuSe QDs respectively. The oxidation peak occurring at $E_{pa} = -592$ mV for the 6MHACuSe QDs, could be assigned to the oxidation of $\text{Se}^{2-} \rightarrow \text{Se} + 2\text{e}^-$, within the quantum dots. The oxidation peak occurring at $E_{pa} = 624$ mV for the 3MPACuSe QDs, is probably caused by the oxidation of the deprotonated thiol capping agent on the QDs surface. Another explanation could also be the oxidation selenium.[70] The completely reversible reaction visible for the MSACuSe QDs involves transfer of one electron and is occurring with the average formal potential of $E^{0'} = 183$ mV. The redox reaction could be assigned to the one electron oxidation and reduction of $\text{Cu} \leftrightarrow \text{Cu}^+ + \text{e}^-$, of the copper agent within the QDs.

From the measurements it can be said that the quantum dots exhibit specific electrochemical properties depending of the nature of the capping agent. This can partly be explained by the different stoichiometries for each of the CuSe QDs, but also by the interaction between the specific capping agent and the electrode surface. The QDs showed good ability to immobilize on the electrode surface and could be further used for different electrochemical constructs. The biocompatibility attributed to the capping of the thiol carboxylic acid, makes them a good alternative in electrochemical biosensors and other bioelectric systems.



3.4 Conclusion

Water-soluble copper selenide QDs were successfully synthesized through an aqueous route with the use of different capping agents: 6MHA, 3MPA and MSA. These capping agents have, to the best of our knowledge, never been explored for capping of CuSe QDs before. The type of capping agent had effect on the stoichiometry, size distribution and stability of the QDs. The formed nanoparticles had a small average size which was confirmed through HRTEM, SAXS and XRD analysis. HRTEM and XRD analysis showed that 6MHACuSe QDs gave the smallest average core size when dried. The average core size calculated was 8.97 and 9.8 nm for HRTEM and XRD respectively. In aqueous solution, the MSACuSe QDs has the smallest hydrodynamic size 50.8 nm in diameter (concluded by DLS) and core size of 4 nm (showed in the SAXS measurements). However, the tendency to aggregate was also largest within the MSACuSe QDs. This could be seen by the irregular shape of the PDDF curve from the SAXS measurements and the high PDI value of the DLS measurements.

The capping of CuSeQDs was confirmed by FTIR via the specific COOH, CH₂ and C-S signature bands of 3MPA and 6MHA. The water-soluble nature of the MSACuSe QDs pointed towards bonding of the thiol carboxylic acid. However, the MSA bond to the CuSe QDs is indicated to be unstable, leading to lower stability of the QDs in aqueous solution. The stoichiometry of the QDs also showed to be affected by the capping agent of choice and was investigated through XRD analysis. The linear molecules 6MHA and 3MPA mainly gave non-stoichiometric form (Cu_{2-x}Se) and the branched MSA capping agent gave mainly β-CuSe stoichiometric form. This difference gave effect on the optical and electrochemical properties of the QDs, which was investigated through UV-vis absorption, PL and CV. The QDs exhibited a large blue shift of the band gap (caused by the quantum confinement effect) which was determined through UV-vis absorption studies. PL studies confirmed that the 6MHACuSe and 3MPACuSe QDs emits light at 435 nm whereas the MSACuSe QDs emits light at 485 nm. Cyclic voltammetry studies confirmed good electrochemical properties when immobilized on an electrode surface. These makes the QDs possible to use as an alternative in enzymatic electrochemical biosensor as an electron mediator and enzyme linking agent.

3.5 References

- [1] A. Leitenstorfer, Artificial atoms for quantum optics, *Nature*. 5 (2006) 855–856.
- [2] L.I. Medintz, H.T. Uyeda, R.E. Goldman, H. Mattoussi, Quantum dot bioconjugates for imaging, labelling and sensing, *Nat. Mater.* 4 (2005) 435–336.
doi:doi:10.1038/nmat1390.
- [3] W.C.W. Chan, D.J. Maxwell, X. Gao, R.E. Bailey, M. Han, S. Nie, Luminescent quantum dots for multiplexed biological detection and imaging, *Curr. Opin. Biotechnol.* 13 (2002) 40–46. doi:10.1016/S0958-1669(02)00282-3.
- [4] J.M. Chalovich, E. Eisenberg, Semiconductor Quantum Dots for Bioimaging and Biodiagnostic Applications, *Biophys. Chem.* 257 (2005) 2432–2437.
doi:10.1016/j.immuni.2010.12.017.Two-stage.
- [5] O.E. Semonin, J.M. Luther, M.C. Beard, Quantum dots for next- generation photovoltaics, *Mater. Today*. 15 (2012) 508–515. doi:10.1016/S1369-7021(12)70220-1.
- [6] M. Khan, S. Park, *Journal of Colloid and Interface Science* Glucose biosensor based on GOx / HRP bienzyme at liquid – crystal / aqueous interface, 457 (2015) 281–288.
- [7] Y.R. Park, J.H. Doh, K. Shin, Y.S. Seo, Y.S. Kim, S.Y. Kim, W.K. Choi, Y.J. Hong, Solution-processed quantum dot light-emitting diodes with PANI:PSS hole-transport interlayers, *Org. Electron. Physics, Mater. Appl.* 19 (2015) 131–139.
doi:10.1016/j.orgel.2014.12.030.
- [8] N. Singh, Z. Salam, N. Sivasankar, A. Subramania, ZnSe quantum dots sensitized electrospun ZnO nanofibers as an efficient photoanode for improved performance of QDSSC, *Mater. Sci. Semicond. Process.* 64 (2017) 16–23.
- [9] S. Chand, N. Thakur, S.C. Katyal, P.B. Barman, V. Sharma, P. Sharma, Recent developments on the synthesis , structural and optical properties of chalcogenide quantum dots, *Sol. Energy Mater. Sol. Cells.* 168 (2017) 183–200.
- [10] P. V Kamat, Quantum Dot Solar Cells . Semiconductor Nanocrystals as Light Harvesters †, *J. Phys. Chem.* 112 (2008) 18737–18753.
- [11] C. Coughlan, M. Iba, O. Dobrozhan, A. Singh, A. Cabot, K.M. Ryan, Compound Copper Chalcogenide Nanocrystals, *Chem. Rev.* 117 (2017) 5865–6109.
doi:10.1021/acs.chemrev.6b00376.
- [12] N. Moloto, H. Puggens, S. Govindraju, B. Rakgalakane, M. Kalenga, Schottky solar cells : Anisotropic versus isotropic CuSe nanocrystals, *Thin Solid Films.* 531 (2013) 446–450.
- [13] X. She, Q. Zhang, C. Wang, S. Chen, New insights into the phosphine-free synthesis of ultrasmall Cu 2 Å x Se nanocrystals at the liquid – liquid interface, *R. Soc. Chem. Adv.* 5 (2015) 90705–90711. doi:10.1039/c5ra18313h.
- [14] C.M. Hessel, V.P. Pattani, M. Rasch, M.G. Panthani, B. Koo, J.W. Tunnell, B.A. Korgel, Copper Selenide Nanocrystals for Photothermal Therapy, *Nano Lett.* 11 (2011) 2560–2566.
- [15] S.L. White, P. Banerjee, P.K. Jain, Liquid-like cationic sub-lattice in copper selenide clusters, *Nat. Commun.* (2017) 1–11. doi:10.1038/ncomms14514.

- [16] R.D. Heyding, R.M. Murray, The crystal structures of $\text{Cu}_{1.8}\text{Se}$, Cu_3Se_2 , α - and γCuSe , CuSe_2 , and CuSe_2II , *Can. J. Chem.* 54 (1976).
- [17] A. Schäfer, M. Kollwitz, R. Ahlrichs, M. Kollwitz, R. Ahlrichs, Electronic excitation energies in copper selenide clusters Electronic excitation energies in copper selenide clusters, *J. Chem. Phys.* 104 (1996) 7113–7121. doi:10.1063/1.471404.
- [18] V.M. Glazov, A.S. Pashinkin, V.A. Fedorov, Phase Equilibria in the Cu-Se System, *Inorg. Mater.* 36 (2000) 641–652.
- [19] Y. Wu, I. Korolkov, X. Qiao, X. Zhang, J. Wan, X. Fan, Facile synthesis of CuSe nanoparticles and high-quality single-crystal two-dimensional hexagonal nanoplatelets with tunable near-infrared optical absorption, *J. Solid State Chem.* 238 (2016) 279–283.
- [20] H. Shen, H. Wang, H. Yuan, L. Ma, L. Song Li, Size-, shape-, and assembly-controlled synthesis of Cu_{2-x}Se nanocrystals via a non-injection phosphine-free colloidal method, *CrystEngComm.* 14 (2012) 555–560. doi:10.1039/c1ce05887h.
- [21] P. Huang, Y. Kong, Z. Li, Copper Selenide Nanosnakes : Bovine Serum Albumin-Assisted Room Temperature Controllable Synthesis and Characterization, *Nanoscale Res Lett.* 5 (2010) 949–956. doi:10.1007/s11671-010-9587-0.
- [22] X.Q. Chen, Z. Li, Y. Bai, Q. Sun, Z. Wang, S. Xue, Room-Temperature Synthesis of Cu_{2-x}E ($\text{E} = \text{S}, \text{Se}$) Nanotubes with Hierarchical Architecture as High-Performance Counter Electrodes of Quantum-Dot-Sensitized Solar Cells, *Chem. a Eur. J.* 20 (2014) 1–10. doi:10.1002/chem.201405354.
- [23] S. Govindraju, M.P. Kalenga, M. Airo, M.J. Moloto, L.M. Sikhvivilu, N. Moloto, Size quantization in Cu_2Se nanocrystals, *Opt. Mater. (Amst).* 38 (2014) 310–313.
- [24] P. Kumar, K. Singh, Synthesis , characterizations , and optical properties of copper selenide quantum dots, (2011) 103–110. doi:10.1007/s11224-010-9698-3.
- [25] K. Kaviyarasu, A. Ayeshamariam, E. Manikandan, J. Kennedy, R. Ladchumananandasivam, U. Umbelino De Gomes, M. Jayachandran, M. Maaza, Solution processing of CuSe quantum dots : Photocatalytic activity under RhB for UV and visible-light solar irradiation Dear Author , added to the article before publication , but are not reflected, *Mater. Sci. Eng. B.* 210 (2016) 1–9. doi:10.1016/j.mseb.2016.05.002.
- [26] O.A. Balitskii, M. Sytnyk, J. Stangl, D. Primetzhofer, H. Groiss, W. Heiss, Tuning the Localized Surface Plasmon Resonance in Cu_{2-x}Se Nanocrystals by Postsynthetic Ligand Exchange, (2014) 2–7.
- [27] O.U. Chen, Doped and Undoped Nanoparticles: Synthesis and Characterization, 2010.
- [28] H. Li, Y. Zhu, S. Avivi, O. Palchik, J. Xiong, Y. Koltypin, V. Palchik, A. Gedanken, Sonochemical process for the preparation of α -CuSe nanocrystals and flakes { , (2002) 3723–3727. doi:10.1039/b206193g.
- [29] C.W.E.I. Soon, Synthesis and Characterisation of Copper Selenide Nanoparticles via Emulsion Technique, 2011.
- [30] B. Ghatori, S. Bathula, K. Tyagi, A.K. Sirvasrava, A. Dhar, R.C. Budhani, Nanostructured copper - selenide with high thermoelectric figure - of - merit and

process for the preparation thereof, 2015.

- [31] C. Nanoparticles, B.M.A. Malik, P.O. Brien, A Novel Route for the Preparation of CuSe and, d (1999) 1441–1444.
- [32] P.P. Ingole, P.M. Joshi, S.K. Haram, Room temperature synthesis of 1-hexanethiolate capped Cu_{2-x}Se quantum dots, in Triton X-100 water-in-oil microemulsions, *Colloids Surfaces A Physicochem. Eng. Asp.* 337 (2009) 136–140. doi:10.1016/j.colsurfa.2008.12.011.
- [33] P.M. Kalenga, Supervisors:, N. Moloto, J. Moloto, L.M. Sikhwivhilu, Synthesis and characterization of copper chalcogenide nanoparticles and their use in solution processed photovoltaics, 2015.
- [34] L.I.U. Xing, L.U.O. Yang, Surface Modifications Technology of Quantum Dots Based Biosensors and Their Medical Applications, *Chinese J. Anal. Chem.* 42 (2014) 1061–1069. doi:10.1016/S1872-2040(14)60753-2.
- [35] X. Chen, Ambient Facile Synthesis of Gram-Scale Copper Selenide Nanostructures from Commercial Copper and Selenium Powder, (2015). doi:10.1021/acsami.5b01085.
- [36] P.M. Ndangili, A.M. Jijana, P.G.L. Baker, E.I. Iwuoha, 3-Mercaptopropionic acid capped ZnSe quantum dot-cytochrome P450 3A4 enzyme biotransducer for 17 β -estradiol, *J. Electroanal. Chem.* 653 (2011) 67–74. doi:10.1016/j.jelechem.2010.12.029.
- [37] I.M. Klotz, G.H. Czerlinski, H.A. Fiess, A Mixed-valence Copper Complex with Thiol Compounds, *J. Am. Chem. Soc.* 1 (1958) 2920–2923.
- [38] E. Nxusani, P.M. Ndangili, R. a. Olowu, a. N. Jijana, T. Waryo, N. Jahed, R.F. Ajayi, P. Baker, E.I. Iwuoha, 3-Mercaptopropionic Acid Capped Ga_2Se_3 nanocrystal-CYP3A4 Biosensor for the Determination of 17-Alpha-Ethinyl Estradiol in Water, *Nano Hybrids.* 1 (2012) 1–22. doi:10.4028/www.scientific.net/NH.1.1.
- [39] S. Sonia, P.S. Kumar, D. Mangalaraj, N. Ponpandian, C. Viswanathan, Influence of growth and photocatalytic properties of copper selenide (CuSe) nanoparticles using reflux condensation method, *Appl. Surf. Sci.* 283 (2013) 802–807.
- [40] D.M. Gruen, O.A. Shenderova, A.Y. Vu, Synthesis, Properties and Applications of Ultrananocrystalline Diamond, Springer, Netherlands, 2005.
- [41] K. Lin, Phase Identification Using Series of Selected Area Diffraction Patterns and Energy Dispersive Spectrometry within TEM, *Sci. Res.* 2 (2014) 57–66.
- [42] M. Nyman, L.B. McQuade, Small Angle X-ray Scattering of Group V Polyoxometalates, in: L. Ruhlmann, D. Schaming (Eds.), *Trend Polyoxometalates Res.*, Nova Science Publishers, 2015: pp. 151–170.
- [43] H. Schnablegger, Y. Singh, *The SAXS Guide*, 3rd ed., Anton Paar GmbH, 2013.
- [44] S. Kashanian, A.H. Azandaryani, K. Derakhshandeh, New surface-modified solid lipid nanoparticles using N-glutaryl phosphatidylethanolamine as the outer shell, *Int. J. Nanomedicine.* (2011) 2393–2401.
- [45] P. Pathak, M. Nagarsenker, Formulation and Evaluation of Lidocaine Lipid Nanosystems for Dermal Delivery, *AAPS Pharm. Science Technol.* 10 (2009). doi:10.1208/s12249-009-9287-1.

- [46] Malvern Instruments, Dynamic light scattering, Inf. White Pap. (2011) 1–6.
- [47] S.I. Jenkins, M.R. Pickard, D.N. Furness, Y.H. Humphrey, D.M. Chari, Differences in magnetic particle uptake by CNS neuroglial subclasses : implications for neural tissue engineering, *Nanomedicine*. 8 (2013) 951–968.
- [48] R. De Palma, S. Peeters, M.J. Van Bael, H. Van Den Rul, K. Bonroy, W. Laureyn, J. Mullens, G. Borghs, G. Maes, Silane Ligand Exchange to Make Hydrophobic Superparamagnetic Nanoparticles Water-Dispersible, *Chem. Mater.* 19 (2007) 1821–1831.
- [49] A. Dhawan, V. Sharma, Toxicity assessment of nanomaterials : methods and challenges, *Anal. Bioanal. Chem.* 398 (2010) 589–605. doi:10.1007/s00216-010-3996-x.
- [50] Malvern Instruments Ltd, Zetasizer Nano Series User Manual, 2004.
- [51] A. Arivarasan, S. Ganapathyb, A. Alsalmec, A. Jayavela, A. Ramasamy, Structural, optical and photooltaic properties of Co-doped CdTe QDs for quantum dots sensitized solar cells, *Superlattices Microstruct.* (2015). doi:10.1016/j.spmi.2015.10.032.This.
- [52] L. Jiménez-hernández, O. Estévez-hernández, M. Hernández-sánchez, J.A. Díaz, 3-mercaptopropionic acid surface modification of Cu-doped ZnO nanoparticles : Their properties and peroxidase conjugation, *Colloids Surfaces A Physicochem. Eng. Asp.* 489 (2016) 351–359.
- [53] G. Aylward, T. Findlay, *SI Chemical Data 6th Edition*, 6th ed., John Wiley & Sons Australia, Milton, 2008.
- [54] R. Iñiguez, O. Arellano, M. Flores-Acosta, S.J. Castillo, Copper-selenide and copper-telluride composites powders sintetized by ionic exchange, *Chalcogenide Lett.* 11 (2014) 13–19.
- [55] M. Koder, T. Kita, I. Miura, Hydroperoxo - Copper (II) Complex Stabilized by N 3 S-Type Ligand Having a Phenyl Thioether, *J. Am. Chem. Soc.* 123 (2001) 7715–7716.
- [56] Y. Lee, D. Lee, A.A.N. Sarjeant, L.N. Zakharov, A.L. Rheingold, K.D. Karlin, D. Chemistry, T. Johns, H. Uni, N.C. Street, C. National, V. Uni, S. Korea, V. Uni, Thioether Sulfur Oxygenation from O 2 or H 2 O 2 Reactivity of Copper Complexes with Tridentate N 2 S thioether Ligands, *Inorg. Chem.* 45 (2006) 10098–10107.
- [57] S. Dhar, D. Senapati, P.K. Das, P. Chattopadhyay, M. Nethaji, A.R. Chakravarty, Ternary Copper Complexes for Photocleavage of DNA by Red Light : Direct Evidence for Sulfur-to-Copper Charge Transfer and d - d Band Involvement, *J. Am. Chem. Soc.* 125 (2003) 12118–12124.
- [58] S. Sarkar, B. Das, Synthesis and characterization of mononuclear copper (II) complex of tetradentate N2S2 donor set and the study of DNA and bovine serum albumin binding Complex Metals : an Open Access Journal, *Complex Met.* 1 (2014) 80–87. doi:10.1080/2164232X.2014.887448.
- [59] V.M. García, L. Guerrero, P.K. Nair, M.T.. Nair, Effect of thermal processing on optical and electrical properties of copper selenide thin films, *Sperficies Y Vacío.* 9 (1999) 213–218.
- [60] Z. Jun-Jie, L. Jing-Jing, H. Hai-Ping, C. Fang-Fang, Quantum Dots for DNA

Biosensing, Springer Heidelberg, London, 2013.

- [61] T.M. Samir, M.M.H. Mansour, S.C. Kazmierczak, H.M.E. Azzazy, Quantum dots: heralding a brighter future for clinical diagnostics., *Nanomedicine (Lond)*. 7 (2012) 1755–69. doi:10.2217/nmm.12.147.
- [62] N.N. Trung, Q. Luu, B.T. Son, Enhanced Fluorescence , Morphological and Thermal Properties of CdSe / ZnS Quantum Dots Incorporated in Silicone Resin, *J. Nanosci. Nanotechnol.* 13 (2013) 434–442. doi:10.1166/jnn.2013.7081.
- [63] P. Monk, *Fundamentals of Electroanalytical Chemistry*, John Wiley & Sons Ltd, Manchester, 2001.
- [64] D.A.C. Brownson, C.E. Banks, *The Handbook of Graphene Electrochemistry*, Springer, 2014. doi:10.1007/978-1-4471-6428-9.
- [65] A.A.L.I. Shaikh, J. Firdaws, N.A. Pasha, P.K. Bakshi, A cyclic voltammetric study of the influence of supporting electrolytes on the redox behaviour of Cu(II) in aqueous medium, *J. Bangladesh Chem. Soc.* 24 (2011) 158–164. doi:10.3329/jbcs.v24i2.9704.
- [66] A.A. Shaikh, J. Firdaws, S. Serajee, M.S. Rahman, P.K. Bakshi, Electrochemical Studies of the pH Dependence of Cu (II) Reduction in Aqueous Britton-Robinson Buffer Solution, *Int. J. Electrochem. Sci.* 6 (2011) 2333–2343.
- [67] S.S. Viswanathan, C.-W. Lee, Selenium Electrochemistry, *RSC Adv.* 3 (2017) 10058–10077. doi:10.1039/C3RA40678D.
- [68] G. Ziyatdinova, L. Grigor, H. Budnikov, Electrochemical oxidation of sulfur-containing amino acids on an electrode modified with multi-walled carbon nanotubes, *Microchim. Acta.* 165 (2009) 353–359. doi:10.1007/s00604-009-0142-6.
- [69] A. Masek, E. Chrzescijanska, M. Zaborski, Estimation of the Antioxidative Properties of Amino Acids – an Electrochemical Approach, *Int. J. Electrochem. Sci.* 9 (2014) 7904–7915.
- [70] N. Gaponik, S.K. Poznyak, N.P. Osipovich, A. Shavel, A. Eychmu, Original Paper Electrochemical probing of thiol-capped nanocrystals, *Microchim. Acta.* 160 (2008) 327–334. doi:10.1007/s00604-007-0765-4.

Chapter 4: Enzyme-based Toremifene Biosensor



Summary

The chapter describes the fabrication of an enzyme-based electrochemical biosensor for the detection of toremifene (TOR). The biosensor consisted of a gold electrode modified with a monolayer of cysteamine conjugated to 6MHACuSe QDs. The QDs were further conjugated to cytochrome P450 2C9 enzyme (CYP2C9). The surface topography of surface modified gold electrodes was examined using atomic force microscopy (AFM) for confirmation of successful construction of biosensor surface. The biosensor response to different TOR concentrations were investigated using cyclic voltammetry (CV) and square-wave voltammetry (SWV).

Abstract

With rising knowledge of the effects on plasma concentration caused by allelic variations in the cytochrome P450 genes and other metabolic factors such as drug-drug or drug-food interactions, more attention is paid to the possibility of therapeutic drug monitoring (TDM). Thus, there is a rising demand for quick, low-cost and efficient equipment for drug targeting. For such devices, electrochemical biosensing techniques serve as a promising alternative. Toremifene is the chlorinated analogue of tamoxifen and is used for adjuvant antiestrogenic treatment for breast cancer and could serve as a candidate for TDM treatments. In this work, a proof of concept enzymatic electrochemical biosensor is developed for the detection of toremifene in aqueous solution. The biosensor utilized water-soluble 6-mercaptopropionic acid capped copper selenide quantum dots (6MHACuSe QDs) conjugated to a cysteamine self-assembled monolayer on a gold electrode. The 6MHACuSe QDs were further conjugated with CYP2C9 enzyme, which has shown to have a major part in the hydroxylation of toremifene (TOR) to form 4-hydroxytoremifene (4OH-TOR). Cyclic voltammetry (CV) and square-wave voltammetry (SWV) studies showed that the 6MHACuSe QDs served as an electron mediator and enzyme immobilizer on the electrode surface. The QDs also showed to retain the catalytic properties of the CYP2C9 enzyme. The small K_M^{APP} values obtained for CV and SWV (0.08 pM and 0.27 pM respectively) indicates high binding affinity between the substrate and CYP2C9 enzyme on the electrode surface. The biosensor response for the CV measurements had a very small dynamic linear range (DLR) up to 0.3 pM, $R^2 = 0.85078$, with a sensitivity of 241.2 nA pM^{-1} . The limit of detection (LOD) corresponded to 0.28 pg mL^{-1} . The DLR could be slightly improved by the use of SWV as a detection technique in comparison to cyclic voltammetry. The SWV measurements gave a DLR up to 0.6 pM ($R^2 = 0.98432$). The sensitivity obtained was 212.7 nA pM^{-1} with a LOD corresponding to 0.08 pg mL^{-1} . The LOD values obtained are lower than detection limits reported for other toremifene detection techniques. Toremifene in blood plasma or urine samples is commonly determined by HPLC or LC-MS/MS techniques and the LOD ranges within $0.2 - 30 \text{ ng mL}^{-1}$. In addition, the LODs of the biosensor construct is significantly lower than reported steady state plasma concentrations (C_{ss}) amongst patients with advanced breast cancer administered with 60 mg (normal daily dose) of TOR. Amongst these patients, $C_{ss} = 879 \text{ ng mL}^{-1}$. The biosensor has potential of detecting presence of very small amounts of toremifene in plasma samples.

4.1 Introduction

Breast cancer is the leading form of cancer amongst women. In the year of 2017, breast cancer is estimated to represent 30 % of the new cancer cases in the United States.[1,2] Antiestrogenic treatment is the fundament of medical breast cancer treatment. Amongst these, the selective estrogen receptor inhibitor (SERM) tamoxifen is the oldest prescribed drug for targeted antiestrogenic breast cancer therapy. [3] Toremifene is the chlorinated analogue of tamoxifen (Figure 4.1) and has also been approved for use as postoperative adjuvant antiestrogenic treatment of breast cancer. [4,5]

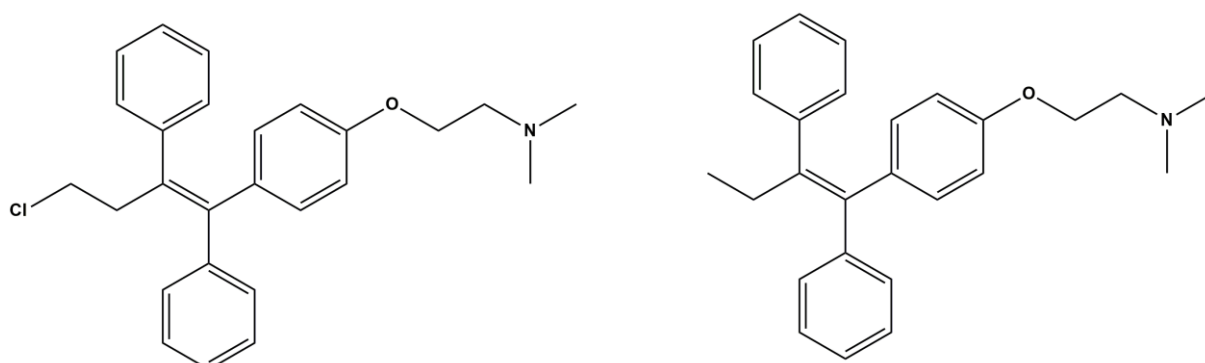


Figure 4.1 Molecular structure of Toremifene (left) and Tamoxifen (right).

Tamoxifen is often referred to as a prodrug due to its more potent ER-binding and inhibiting metabolites: 4-hydroxyl-tamoxifen and endoxifen.[6,7] Plasma concentrations of tamoxifen and its metabolites have shown significant variations within patients carrying different genotypes of the cytochrome P450 (CYP) 2D6 enzyme. [7–9] In contrast, toremifene is not considered a prodrug or as being affected by CYP2D6 polymorphism. [9] However, in a comparative metabolic study by Watanabe and co-workers [6], CYP2C9 enzyme showed to have a dominating role in the 4-hydroxylation of toremifene to 4-hydroxyl-toremifene (4OH-TOR) in human liver microsomes. 4OH-TOR is one of the main metabolites in the phase I metabolism of toremifene. CYP2C9 enzyme also has allelic variations of CYP2C9*2 and CYP2C9*3. To have polymorphic alteration in both the CYP2D6 and CYP2C9 is rare and constitutes less than 1 % of the Greek population.[10] However, the authors discuss the possibility that decreased functional alleles of both CYP2D6 and CYP2C9 could influence the pharmacokinetics of toremifene amongst the patients carrying them. [6]

With rising knowledge of the effects on plasma concentration caused by allelic variations in the cytochrome P450 genes and other metabolic factors such as drug-drug or drug-food interactions, more attention is paid to the possibility of therapeutic drug monitoring (TDM). The possibilities to observe the plasma concentration and moderate the doses individually between patients could optimize the dosing and treatment outcome. In a review by Widmer and co-workers [11] the authors analyze the benefits with therapeutic drug monitoring of anticancer drugs. The review demonstrates that TDM has had clinical benefits in some cases of cancer treatment where concentration-effect relationship has been studied.[11] The methods used for TDM are often liquid chromatography-tandem mass spectrometry (LC-MS/MS), which is quick and efficient but expensive. [11–13] Laboratories not equipped with LC-MS/MS apparatus, High-performance liquid chromatography coupled to ultraviolet (HPLC-UV) or fluorescence techniques is also an alternative. [14–16]. However, issues that may arise with these techniques is sampling of potentially significant amounts of blood, shipments to distant laboratory, extensive costs of the potentially expensive equipment, potential delays caused by delivery of results and possibly complex interpretation of data. Thus, technological developments that could facilitate the plasma measurements for TDM is needed.[11]

Electrochemical biosensors have been developed for various applications within medicine such as medical diagnostics and real-time disease condition monitoring of a patient. [17–19] In such devices, enzymes have been frequently utilized as a detection component. [19–23] The enzymes ability to specifically bind to a substrate but also detect many different analytes constitutes two of the main advantages as a part of an electrochemical biosensor.[24] Furthermore, enzyme based electrochemical biosensor has been successfully combined with an extra layer of biocompatible quantum dots (QDs) between the electrode and enzyme. The enzyme is then linked to the capping agent surrounding the QDs. The use of QDs as electron mediator was shown to increase the biosensor performance and provide a stable microenvironment for the enzyme.[21,25–28]

This study presents an enzyme based electrochemical biosensor for the detection of toremifene. The biosensor consists of a gold electrode modified with three layers. The first layer consisted of a self-assembled monolayer (SAM) of cysteamine, where the strong S-Au interaction between the sulfur of the thiol group and the gold was utilized. The second layer consisted of 6-mercaptohexanoic acid capped copper selenide (6MHACuSe) QDs. The QDs were immobilized on the electrode surface through conjugation of the carboxylic acid groups of the capping agent with the free amino groups of the cysteamine. The third layer consisted of

CYP2C9 enzyme conjugated to the QDs to form the final Au/Cys/6MHACuSe/CYP2C9 biosensor construct.

4.2 Experimentals

4.2.1 Chemicals

All chemicals used in the experiments were of analytical grade and were used as purchased without further purification. 6-mercaptophexanoic acid (6MHA, 90%), copper(II) nitrate hydrate ($\text{Cu}(\text{NO}_3)_2$, 99.999% trace metal basis), selenium powder (Se, 99.99% metal basis), sodium Borohydride (NaBH_4 , 98%), sodium hydroxide (NaOH , 99.99% trace metal basis), N-(3-dimethylaminopropyl)-N'-ethylcarbodiimide hydrochloride (EDC, $\geq 98\%$) and N-hydroxysuccinimide (NHS, 98%), cysteamine (Cys, $\geq 98.0\%$), toremifene Citrate (TOR, $\geq 98.0\%$), cytochrome P450 2C9 wild type allele enzyme, dimethyl sulfoxide (CYP2C9, $\geq 99.9\%$), dimethyl sulfoxide (DMSO, $>99.9\%$), sodium phosphate dibasic dihydrate (Na_2HPO_4 , $\geq 99.5\%$), sodium phosphate monobasic monohydrate (NaH_2PO_4 , $\geq 99.0\%$), were purchased from Sigma-Aldrich (Cape Town, South Africa). 0.10 M phosphate buffer solution, pH 7.40, was prepared from sodium phosphate dibasic dihydrate and sodium phosphate monobasic monohydrate using Millipore (18 M Ω /cm) purified through SimPak[®] 1 water purification system (Merck Millipore, Germany).

4.2.2 Instrumentation

Screen printed gold electrodes (ref. DRP-110) from DropSens, Spain, were used as working electrode characterization of the modified electrode using atomic force microscopy (AFM). The AFM measurements were made using Nanosurf Easy Scan AFM version 2.2 and easy controller (Nanosurf AG, Switzerland). Graphs were plotted in Gwyddion software.

Cyclic voltammetry (CV) and square wave voltammetry (SWV) was performed using BAS100W integrated and Automated Electrochemical Work Station from Bio Analytical Systems, Lafayette, USA. A three electrode setup was used in a 10 mL electrochemical cell. A gold electrode (surface area = 0.0201 cm²) from BAS was used as working electrode, a platinum wire from Sigma Aldrich served as the counter electrode and a Ag/AgCl (3 M NaCl) from BAS was used as the reference electrode. For investigation of the system response in anaerobic

condition, the phosphate buffer was saturated with $\text{Ar}_{(\text{g})}$ for 15 min. All the biosensor response measurements were performed under aerobic conditions since cytochrome P450 enzymes utilizes oxygen in the catalysis. For CV studies a scan rate of 25 mV s^{-1} was used. For SWV studies an amplitude of 25 mV, step size of 5 mV, frequency of 5 Hz was used with 16 samples per point.

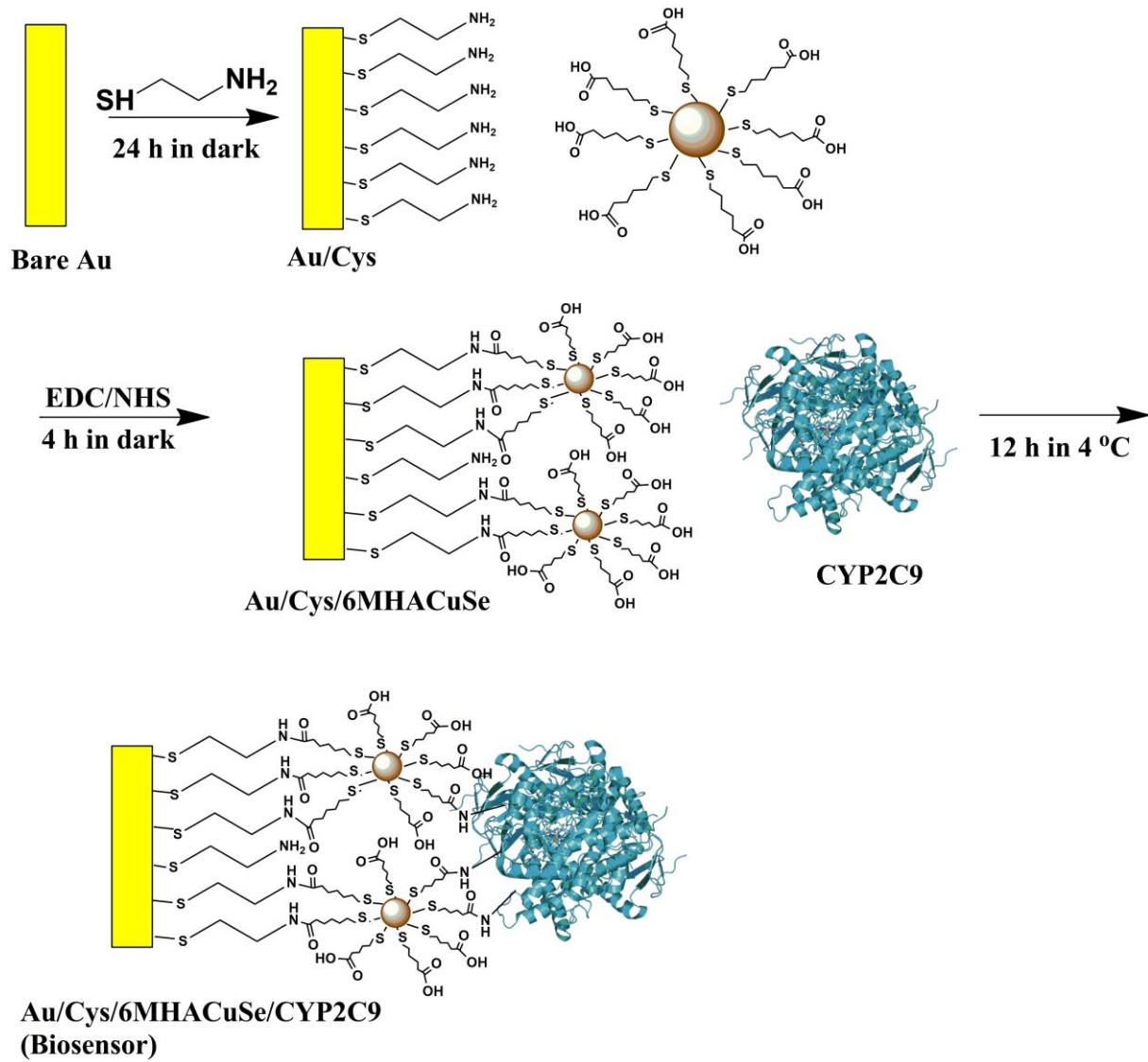
For biosensor response measurements, a stock solution of 1 mM toremifene citrate was prepared by diluting 3 mg toremifene citrate in 5 mL DMSO. From the stock 250 nM solution was prepared through stepwise dilution in 0.1 M phosphate buffer ($\text{pH} = 7.40$).

4.2.3 Construction of Au/Cys/6MHACuSe/CYP2C9 biosensor

6-mercaptohexanoic capped copper selenide quantum dots (6MHACuSe QDs) were synthesized as described in chapter 3.

Before modification a gold (Au) electrode was electrochemically cleaned in 50 mM H_2SO_4 through potential scanning between -400 to 1400 mV until a reproducible cyclic voltammogram was obtained. The electrode was then polished with 1, 0.50, and 0.03 μm alumina slurries in glassy polishing pads respectively followed. The polished electrode was ultrasonicated absolute ethanol and distilled water for 5 min respectively.

The freshly polished Au electrode was modified with a self-assembled monolayer (SAM) of cysteamine by deep coating the electrode in 0.02 M cysteamine solution for 24 h in dark, forming an Au/Cys electrode surface. The Au/Cys electrode was then dipped in a mixture of 6MHACuSe QDs and 0.01 M of EDC/NHS (1:1 ratio) for 4 hours in dark to form the quantum dot modified electrode (Au/Cys/6MHACuSe). The electrode was rinsed carefully with distilled water to remove any unbound molecules and dried under $\text{Ar}_{(\text{g})}$. 3 μL of 10 μM cytochrome P450 2C9 wild type allele enzyme diluted in phosphate buffer, was dropped on the electrode surface. The electrode was allowed to dry in 4 $^\circ\text{C}$ for 12 h to form the final Au/Cys/6MHACuSe/CYP2C9 biosensor construct. The biosensor development upon each surface modification is illustrated in Figure 4.2.



WESTERN CAPE
 Figure 4.2 Schematic illustration of the biosensor formation.

4.3 Results and discussion

4.3.1 Characterization of Au/Cys/6MHACuSe/CYP2C9 electrode surface

Atomic force microscopy (AFM) was performed in order to investigate the topography of the gold electrode upon each surface modification to investigate if the biosensor was successfully formed. The resulting AFM micrographs are illustrated in Figure 4.3 to Figure 4.6. The surface area roughness parameters are summarized in Table 4.1. The measurements were performed using gold screen printed electrode (AuSPE).

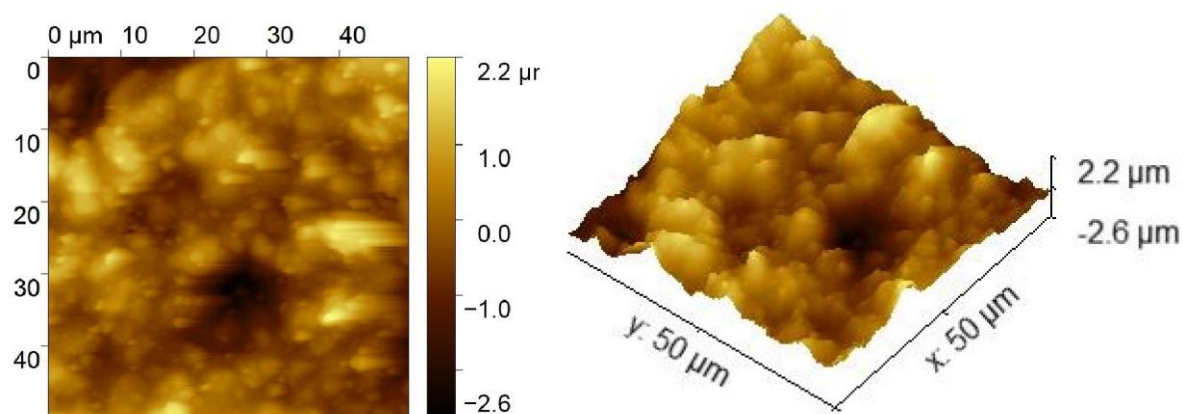


Figure 4.3 The simulated topography of the bare AuSPE.

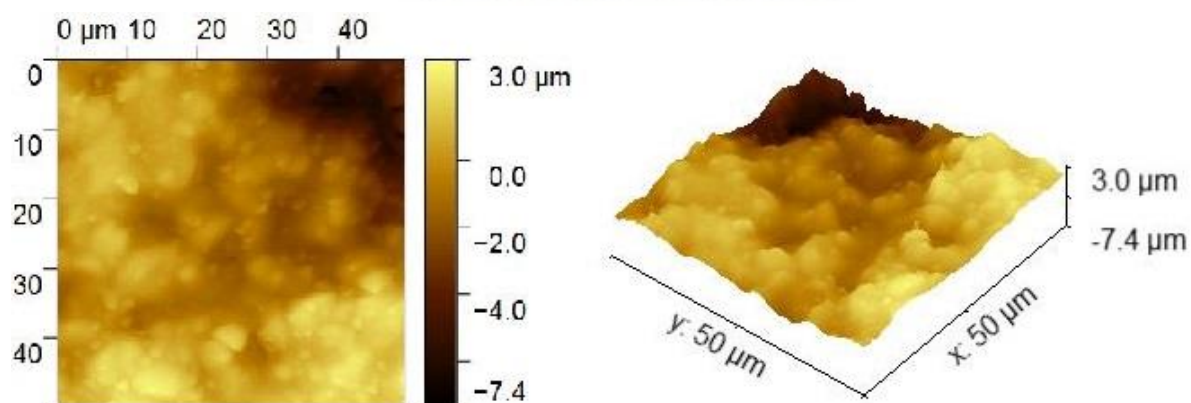


Figure 4.4 The simulated topography of the Au/Cys modified AuSPE.

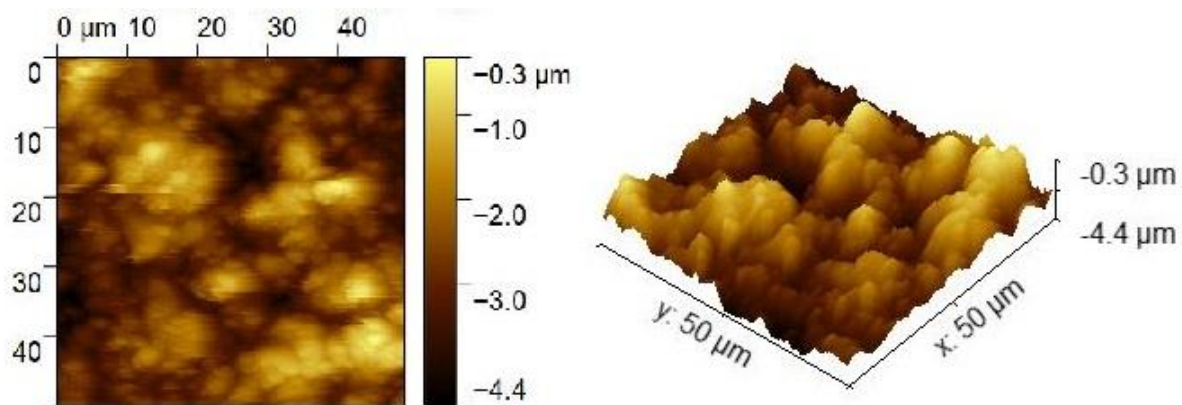


Figure 4.5 The simulated topography of the Au/Cys/6MHACuSe modified AuSPE.

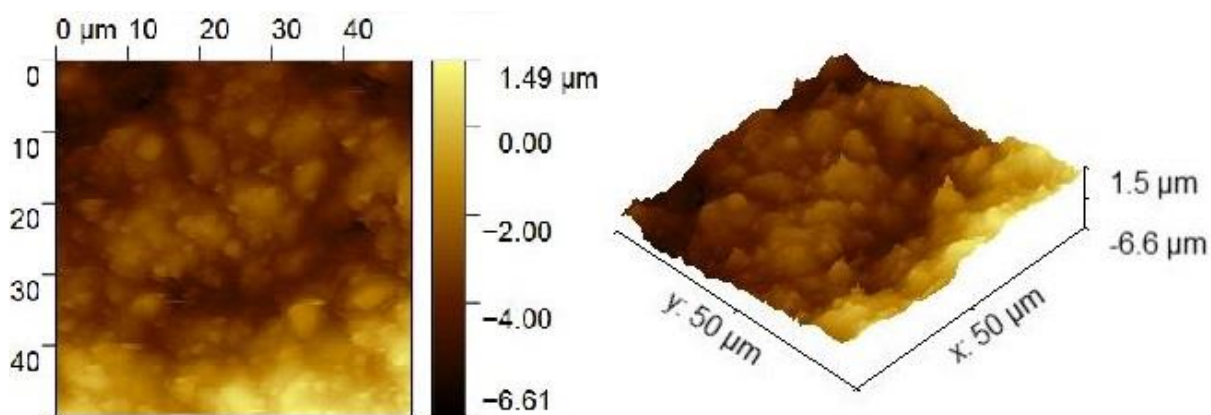


Figure 4.6 The simulated topography of the biosensor constructed on AuSPE.

UNIVERSITY of the
WESTERN CAPE

| Parameters | Bare Au | Au/Cys | Au/Cys/6MHACuSe | Au/Cys/6MHACuSe/CYP2C9 |
|------------|---------|---------|-----------------|------------------------|
| Sa (mV) | 63.2 | 89.6 | 64.5 | 98.4 |
| Sq (mV) | 86.6 | 138.8 | 82.7 | 173.5 |
| Sy (mV) | 3104.5 | 8566.3 | 1200.7 | 14883 |
| Sp (mV) | 1668.9 | 6248.2 | 893.5 | 9906.7 |
| Sv (mV) | -1435.6 | -2318.1 | -307.2 | -4976.0 |

Table 4.1 The average surface area roughness (Sa), the mean square roughness (Sq), the maximum height of the profile (Sy), the maximum profile peak height (Sp) and the maximum profile valley depth (Sv) for each surface modification of the AuSPE.

Table 4.1 shows that the surface area roughness increases with cysteamine immobilization. When immobilizing the 6MHACuSe QDs, the surface becomes smoother. Indicating a quite uniform layer of quantum dots organizing upon the cysteamine self-assembled monolayer. The surface area roughness further increases upon enzyme conjugation to the 6MHACuSe QDs layer. Furthermore, the maximum profile peak height is notably larger in comparison with previous surface modifications. Indicating that larger molecules has been attached to the surface. Zhang and co-workers [29] showed that upon enzyme immobilization an silica plate surface, the surface roughness increases with increasing enzyme activity. Making the increasing surface area roughness as an indicator of successful enzyme immobilization on the surface. Thus, the results confirm that the biosensor was successfully constructed through stepwise linking of cysteamine SAM, 6MHACuSe QDs and CYP2C9 enzyme.



4.3.2 Electrochemical characterization of biosensor

The electrochemical response of the biosensor components were investigated at $\text{Ar}_{(g)}$ saturation (anaerobic), in presence of oxygen (aerobic) and with addition of TOR. With the purpose of determine what reactions that are responsible for the observed current peaks. The behaviour of a surface modified electrode in absence of QDs (Au/Cys/CYP2C9) was also investigated. This was in order to examine the influence of the quantum dots in combination with the CYP2C9 enzyme. The cyclic voltammograms are illustrated in Figure 4.7 to Figure 4.9.

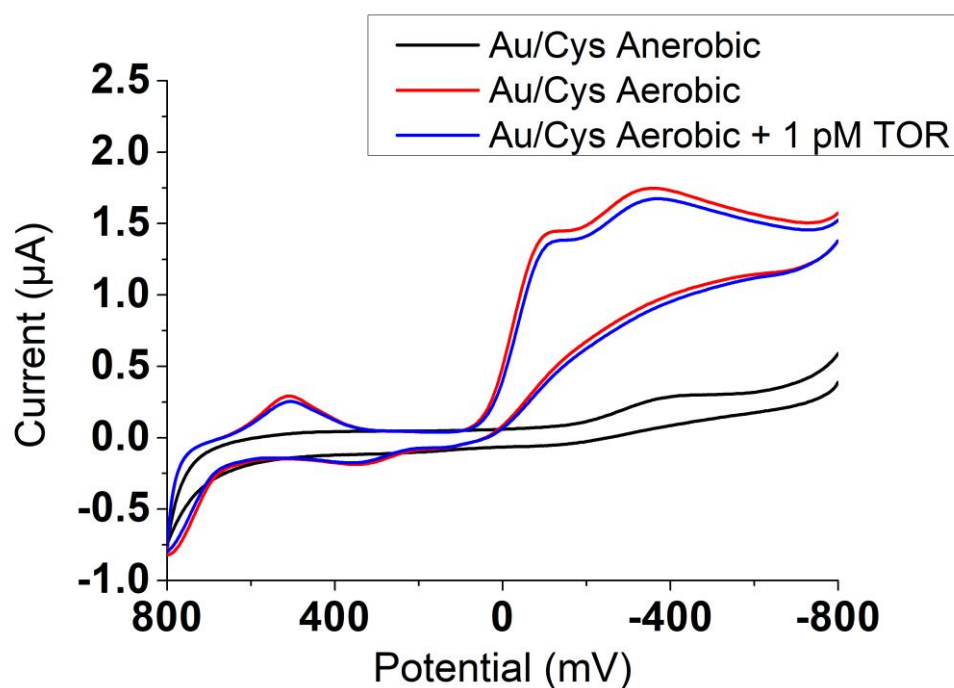


Figure 4.7 Cyclic voltammogram of cysteamine covered gold electrode at anaerobic conditions (black line), aerobic condition (red line) and aerobic condition in presence of 1 pM TOR (blue line) at 25 mV s^{-1} scan rate in 0.1 M phosphate buffer (pH = 7.40).

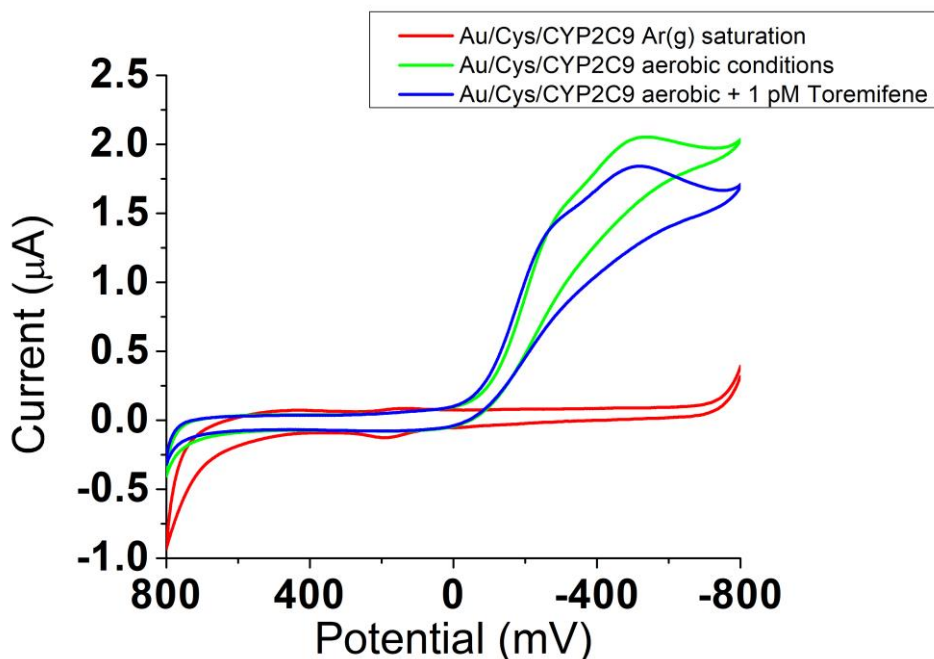


Figure 4.8 Cyclic voltammogram of Au/Cys/CYP2C9 modified electrode at anaerobic conditions (black line), aerobic condition (red line) and aerobic condition in presence of 1 pM TOR (blue line) at 25 mV s⁻¹ scan rate in 0.1 M phosphate buffer (pH = 7.40).

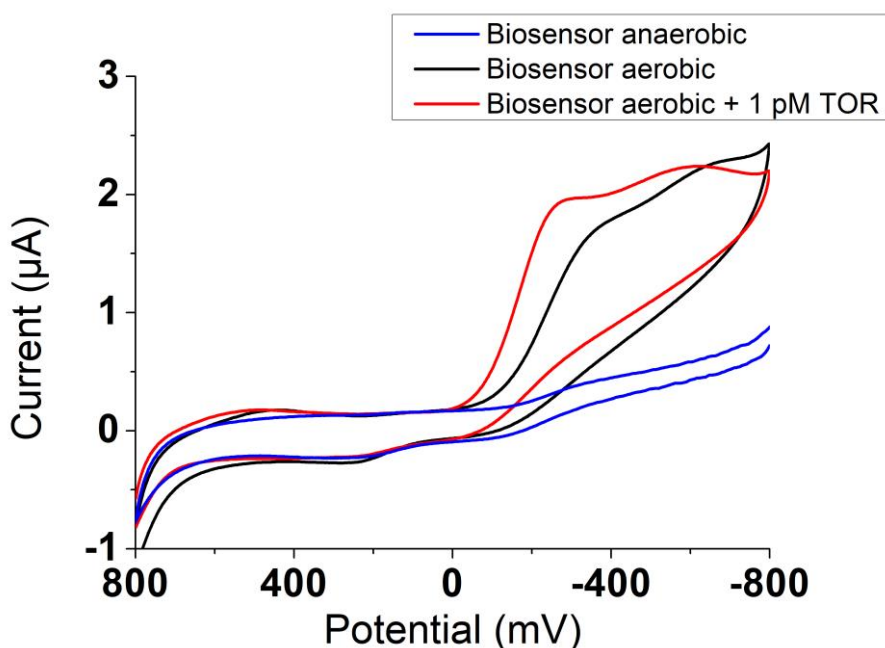


Figure 4.9 Cyclic voltammogram of biosensor construct (Au/Cys/6MHACuSe/CYP2C9) at anaerobic conditions (blue line), aerobic condition (black line) and aerobic condition in presence of 1 pM TOR (red line) at 25 mV s⁻¹ scan rate in 0.1 M phosphate buffer (pH = 7.40).

Figure 4.7 illustrates the cyclic voltammogram of the Au/Cys modified electrode. It is possible to see reduction peaks at $E_{pc} = -122$ mV and $E_{pc} = -350$ mV respectively in aerobic conditions. The peaks were attributed to the reduction of oxygen on the electrode surface.[30] This is supported by the cyclic voltammogram recorded in anaerobic conditions, where these reduction

current peak are absent. Moreover, the addition of 1 pM TOR resulted in a small decrease in the reduction current attributed to the reduction of oxygen.

When enzyme was conjugated to the electrode surface without the QDs, a reduction current peak was visible at $E_{pc} = -520$ mV in aerobic conditions (Figure 4.8). This peak was attributed to the reaction of CYP2C9 together with oxygen. This can be compared with the results obtained from Yang and co-workers [31]. In this work, the authors' designed a biosensor using CYP2C9 enzyme attached to an electrode with 11-mercaptopundecanoic acid and octanethiol SAM for detection of warfarin. For this biosensor construct, a reduction current peak was observed at $E_{pc} = -490$ mV which was attributed to the electron transfer to the heme group of the CYP2C9 enzyme. [31] Furthermore, upon addition of 1 pM TOR, a decrease in the reduction current peak at $E_{pc} = -520$ mV (Figure 4.8). Which indicates that only the cysteamine SAM was not successful in retaining the catalytic properties of the enzyme for toremifene metabolism.

For the biosensor construct (Figure 4.9) a reduction current peak at $E_{pc} = -631$ mV at aerobic conditions, was attributed to the reduction of the CYP2C9 heme group. Upon addition of 1 pM toremifene, a shift in the reduction peak potential could be observed from $E_{pc} = -631$ mV to $E_{pc} = -591$ mV, together with a small increase in peak current. This change was attributed to the catalytic reaction between the CYP2C9 enzyme and the toremifene analyte. Indicating the the 6MHACuSe QDs contributed to retaining of CYP2C9 enzyme activity.

The electrochemical behavior of the biosensor construct was also evaluated at scan rates from 25 mV s^{-1} to 100 mV s^{-1} . The resulting cyclic voltammograms are shown in Figure 4.10.

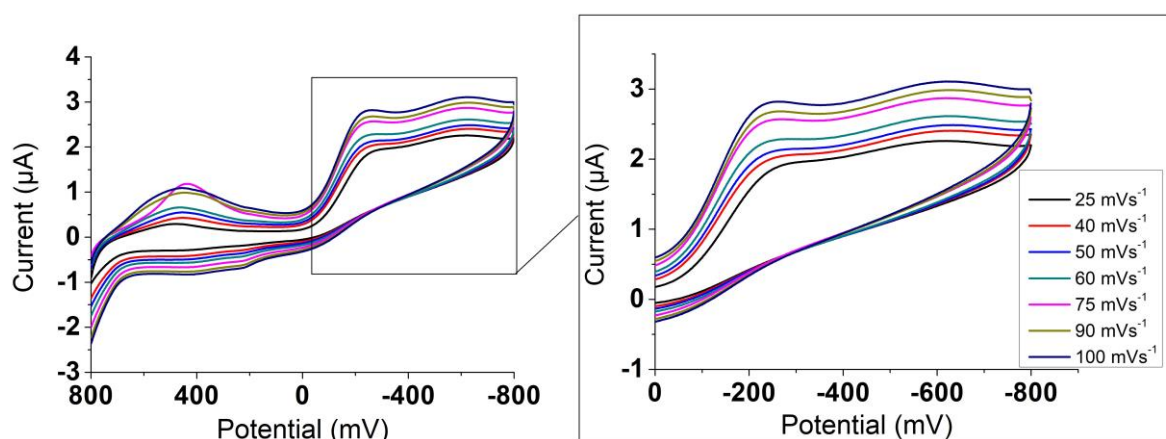


Figure 4.10 Cyclic voltammogram of the biosensor construct at different scan rates in full scale (left) and enlarge segment (right).

By investigating the dependency of the scan rate, it is possible to calculate the concentration of redox active specie on the electrode surface through Equation 4.2.[32,33]

$$I_p = \frac{n^2 F^2}{4RT} v A \Gamma \quad (4.2)$$

Where I_p is the oxidation or reduction peak current, n is the moles of electrons transferred per mole of the electroactive specie (in this case one), F is Faradays constant (96485 C/mole e^-), T is the temperature (in kelvin), v is the scan rate (Vs^{-1}), A is the electrode surface area (in cm^2) and Γ is the surface coverage of the electroactive species (moles/ cm^2). The relationship between the reduction peak current I_{pc} (at $E_{pc} = -631$) mV and the scan rate was illustrated in Figure 4.11.

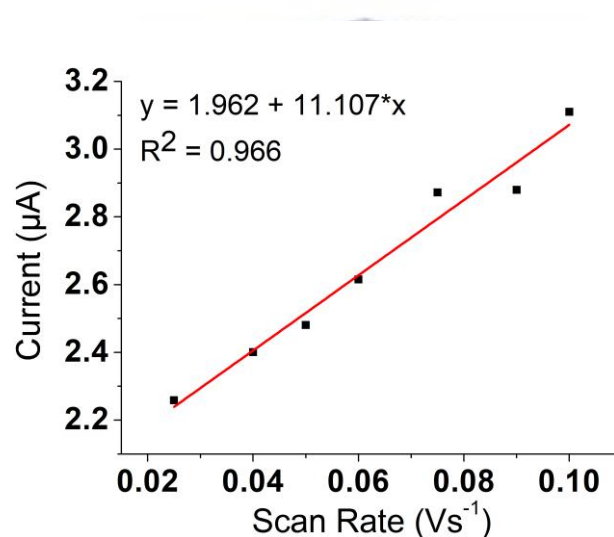


Figure 4.11 The reduction peak current (I_{pc}) of the reduction peak (occurring at $E_{pc} = -631$ mV) at different scan rates, for the biosensor construct.

The reduction peak current at $E_{pc} = -631$ mV had a linear relationship with increasing of the scan rate, with an R-squared value of $R^2 = 0.966$. Through Equation 4.2, the surface concentration of the redox active specie of the biosensor construct (the CYP2C9 enzyme) was calculated to $\Gamma = 5.89 \times 10^{-10}$ moles/ cm^2 .

4.3.3 Biosensor detection response upon addition of toremifene citrate

The response of the biosensor construct was investigated at different concentrations using cyclic voltammetry at a potential window of 800 mV to -800 mV. Small amounts of prepared TOR solution (250 pM) was gradually added to the phosphate buffer medium. The biosensor response for different TOR concentrations can be observed in Figure 3.12. The corresponding calibration plot of the current response (after subtraction of the 0 pM current response) is illustrated in Figure 3.13.

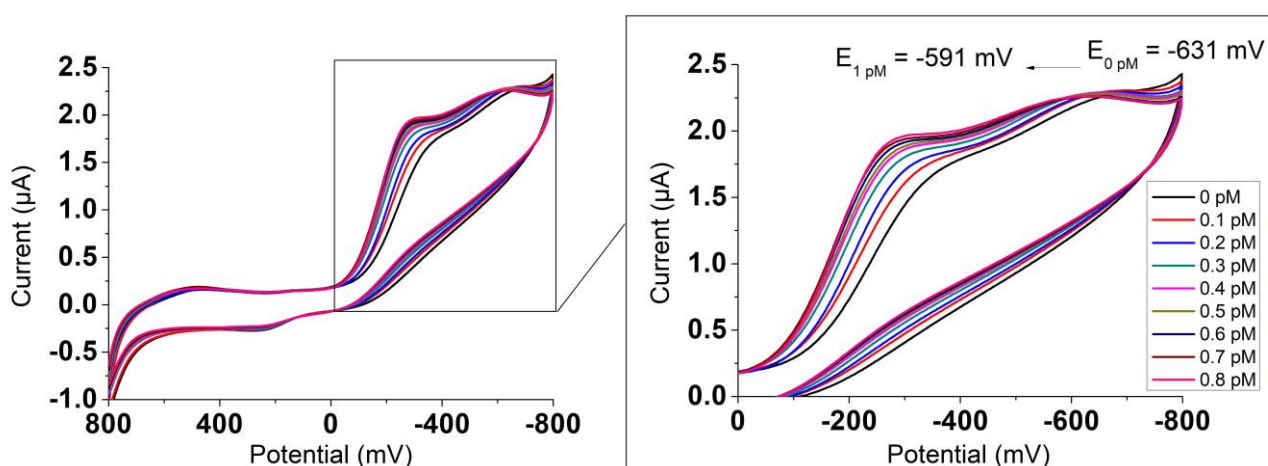


Figure 3.12 Cyclic voltammogram of the biosensor construct at different TOR concentrations at full scale (left) and enlarged segment (right) at 25 mVs⁻¹ in 0.1 M phosphate buffer (pH = 7.40).

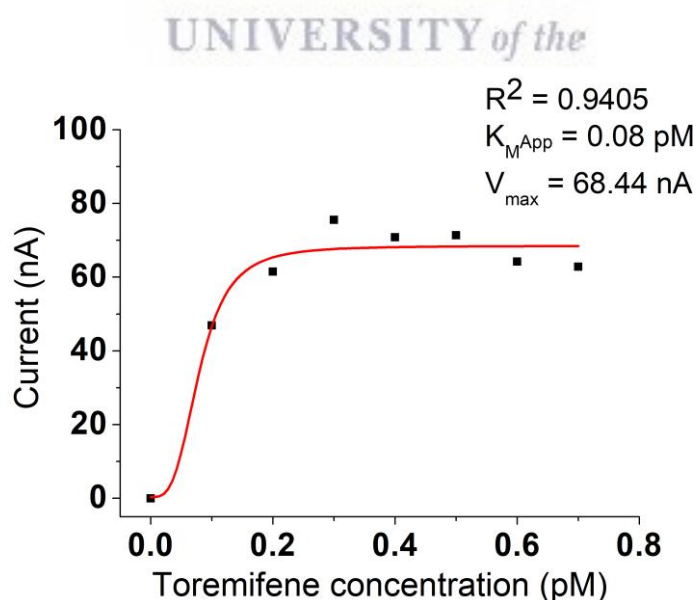


Figure 3.13 The calibration plot of the current response (after subtraction of the 0 pM current response) for the reduction peak current occurring at $E_{\text{pc}} = -631 \text{ mV}$ to -589 mV .

Figure 3.12 shows that with increasing amounts of TOR, the reduction peak at $E_{\text{pc}} = -631 \text{ mV}$ shift towards more positive reduction peak potentials with a net shift from -631 mV to -598

mV. The same increase and peak shift was not observed when the corresponding amounts of only DMSO dissolved in phosphate buffer (at same ratios as for the TOR solution) was added. This indicates that the presence of TOR is responsible for the change observed for the reduction current.

Figure 3.13 shows the dependence of the biosensor response to changes in TOR concentration obtained through cyclic voltammetry measurements. The data was sigmoidal curve fitted. The reduction peak current intensity I_{pc} increases gradually with increasing TOR concentration up to 0.2 pM where after a plateau is reached. For concentrations up to 0.7 pM, the biosensor response followed the Michaelis-Menten kinetics for enzyme based biotransducers [21] as shown in Equation 4.3.

$$I = \frac{V_{max}[TOR]}{K_M^{APP} + [TOR]} \quad (4.3)$$

Where I is the steady state current obtained after addition of toremifene substrate, V_{max} is the maximum peak current measured under saturated substrate conditions, $[TOR]$ is the bulk concentration of toremifene substrate and K_M^{APP} is the Michaelis-Menten constant. The Michaelis-Menten constant (K_M^{APP}) was calculated to $K_M^{APP} = 0.08$ pM. The small value obtained for K_M^{APP} indicates that the substrate binds strongly to the CYP2C9 enzyme.[21] In addition, it is possible to see that the enzyme saturates already at small concentrations (> 0.3 pM), indicating rather low enzyme activity on the electrode surface. The dynamic linear range (DLR) reached up to 0.3 pM, though the range was poorly linear ($R^2 = 0.85078$) showing that optimization is needed to obtain a higher DLR and a greater accuracy. The sensitivity of the sensor was 241.2 nA pM^{-1} . The lower limit of detection (LOD) corresponded to 0.28 pg mL^{-1} toremifene in aqueous solution. After 0.7 pM, the peak current intensity started decreasing, showing that the biosensor construct was not effective after this concentration point.

The biosensor response at different TOR concentrations was also investigated using square-wave voltammetry (SWV) at a potential range of 300 mV to -800 mV. The resulting SWV response was illustrated in Figure 3.14. The corresponding calibration plot (after subtraction of the 0 pM current response) was illustrated in Figure 3.15.

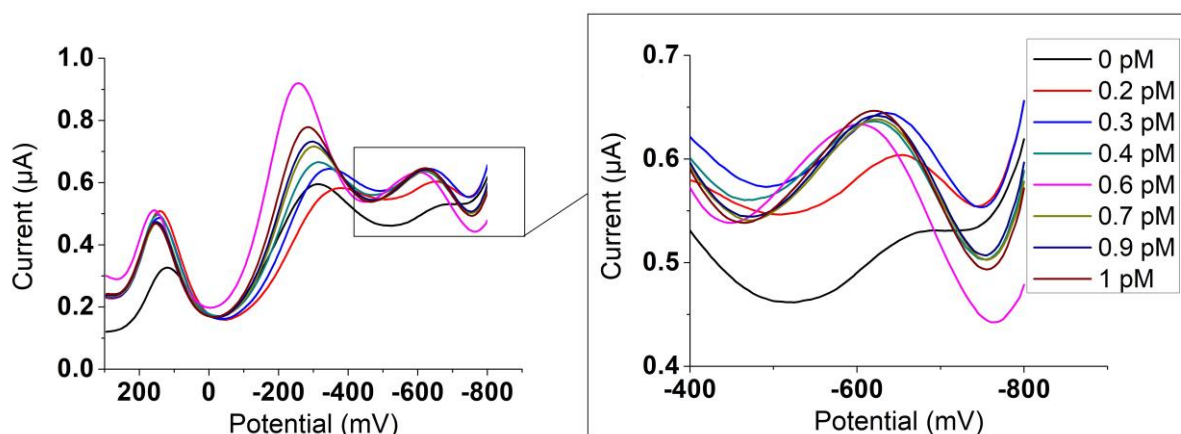


Figure 3.14 The square-wave voltammograms of the biosensor construct at different TOR concentrations.

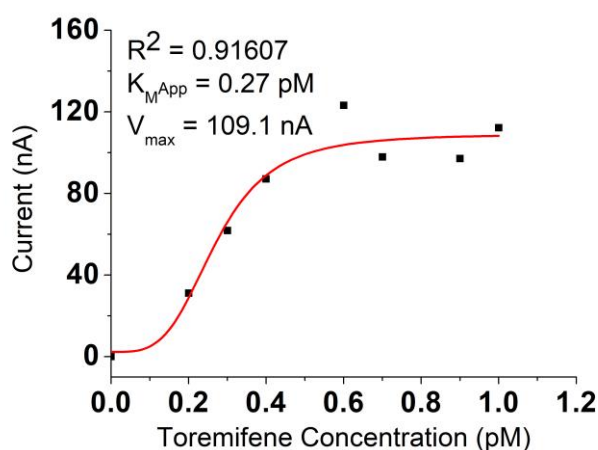


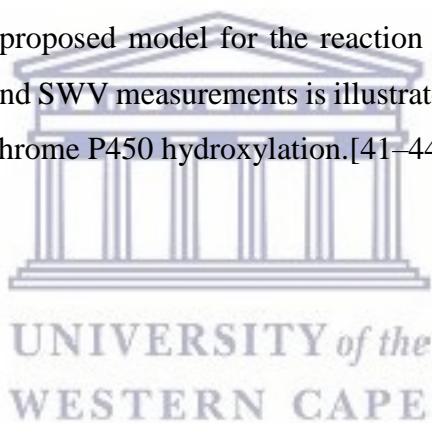
Figure 3.15 The calibration plot of the current response (after subtraction of the 0 pM current response) for the biosensor response from SWV measurements.

For the SWV measurements, the same peak potential shift could be observed accompanied by an increase in the peak current. The dependence of the biosensor response using SWV at different TOR concentrations was illustrated in Figure 3.15. The peak current increases gradually up to 0.6 pM. At higher concentrations a plateau is reached. The biosensor response likewise followed the Michaelis-Menten kinetics for enzyme based biotransducers (Equation 4.3) [21]. When SWV was used as electrochemical method the dynamic linear range for the biosensor response was larger (up to 0.6 pM, $R^2 = 0.98432$) with a sensitivity of 212.7 nA pM^{-1} . The LOD was calculated to 0.08 pg mL^{-1} .

In both cases, The LOD obtained are lower than detection limits reported for other toremifene detection techniques. Toremifene in blood plasma or urine samples is commonly determined by HPLC or LC-MS/MS techniques and the LOD ranges within $0.2 - 30 \text{ ng mL}^{-1}$. [34–38]

Recently, Watanabe and co-workers [6] reported the use of a LC-MS/MS technique with a LOD corresponding to 0.2 ng mL^{-1} (0.5 nM). The biosensor LOD is also lower than the reported steady state plasma concentrations (C_{ss}) reported amongst patients with advanced breast cancer treated with 60 mg of TOR (which is the normal daily dose for TOR treatment). Amongst these patients, $C_{ss} = 879 \text{ ng mL}^{-1}$. [35,39] SWV generally is more sensitive to small concentration changes in the pico molar range, compared to CV. [40] Thus, SWV could be a more fitting technique for analysis using the constructed biosensor in comparison to the results obtained from the CV analysis. The sensor could be useful for detection of very small TOR concentrations in blood plasma.

The utilizing of the 6MHACuSe QDs as an enzyme immobilizer helped to retain the enzymes catalytic properties, in comparison to only cysteamine. The importance of the CYP2C9 enzyme in the 4-hydroxylation of TOR was recently reported by Watanabe and co-workers.[6] Thus, the biosensor could also serve as a tool for further understanding the significance of CYP2C9 in the TOR metabolism. The proposed model for the reaction mechanism for the reduction reactions occurring in the CV and SWV measurements is illustrated in Figure 3.16, and is based on the catalytic cycle for cytochrome P450 hydroxylation.[41–44]



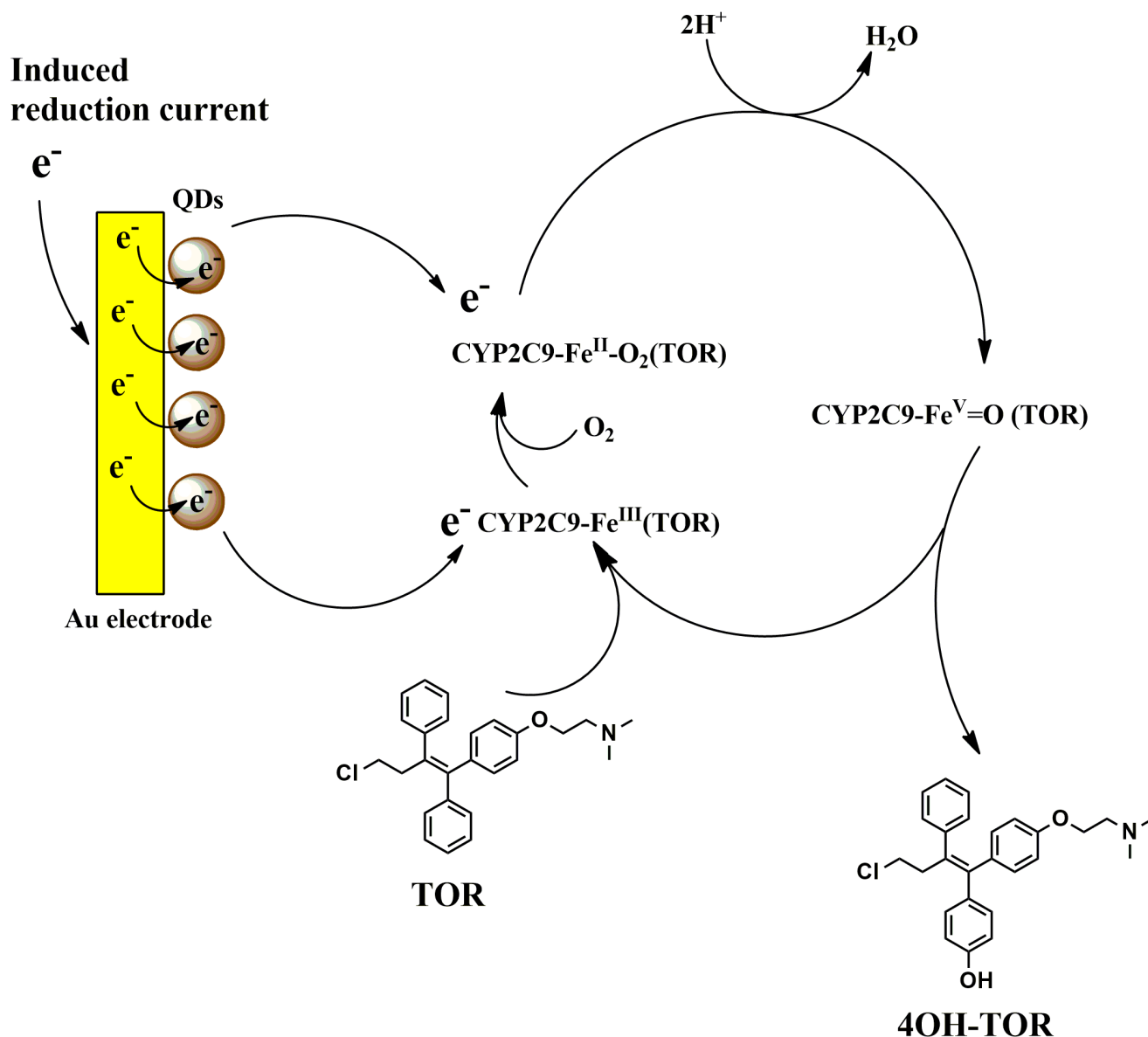


Figure 3.16 Proposed mechanism for reaction occurring at biosensor surface.

However, the biosensor solution would need to be further analyzed using liquid chromatography mass spectrometry or nuclear magnetic resonance. This for the purpose of observing formation of the hydroxylated TOR metabolite 4-hydroxytoremifene (4OH-TOR) which would further confirm that the bioconversion actually is taking place.

4.4 Conclusion

In this work, a QDs-based enzyme electrochemical biosensor was successfully constructed for the detection of TOR in aqueous solution. Through topography studies using AFM the successful construction of the biosensor on a gold electrode surface was confirmed. This was further confirmed through electrochemical studies where a typical reduction peak at $E_{pc} \approx -600$ mV could be detected. The 6MHACuSe QDs contributed to retaining the CYP2C9 enzyme catalytic properties in comparison to only cysteamine as an enzyme immobilizer. This was confirmed through cyclic voltammetry studies (Figure 4.8 and Figure 4.9). Control studies confirm that it is the addition of TOR that causes the change in reduction current in the presence of CYP2C9 enzyme on the electrode surface. This indicated that the metabolic properties of the enzyme were retained. This is further confirmed by the fact that the biosensor response followed the typical Michaelis-Menten kinetics for enzyme based biotransducers.[21]

The small K_M^{APP} values obtained for CV and SWV (0.08 pM and 0.27 pM respectively) indicates high binding affinity between the substrate and CYP2C9 enzyme on the electrode surface, although the DLR obtained from the CV measurements was very small (up to 0.3 pM, $R^2 = 0.85078$) with a sensitivity of 241.2 nA pM⁻¹ and LOD corresponding to 0.28 pg mL⁻¹. This makes the sensor more suitable for determining the presence of toremifene in a sample, rather than determining the exact concentration of the sample. The DLR could be slightly improve by the use of SWV as a detection technique in comparison to cyclic voltammetry. The SWV measurements gave a DLR up to 0.6 pM ($R^2 = 0.98432$). The sensitivity obtained was 212.7 nA pM⁻¹ with a LOD corresponding to 0.08 pg mL⁻¹. The improvement is likely due to the fact that SWV is more sensitive to small concentration changes in the pico molar range. The LOD obtained are lower than detection limits reported for other toremifene detection techniques. Toremifene in blood plasma or urine samples is commonly determined by HPLC or LC-MS/MS techniques and the LOD ranges within 0.2 – 30 ng mL⁻¹. [6,34–38] In addition, the LODs of the biosensor constructs is significantly lower than steady state plasma concentrations (C_{ss}) reported amongst patients with advanced breast cancer administered with 60 mg (normal daily dose) of TOR. Amongst these patients, $C_{ss} = 879$ ng mL⁻¹. [35,39]

The low LODs presented shows that the biosensor has potential of detecting presence of very small amounts of toremifene in plasma samples. This potential could be time-saving for doctors utilizing such a TDM device in practice. Peak plasma concentration levels amongst patients administered with 60 mg of TOR is reached between 1.5-3 h.[35] Because of the low detection

limit of the biosensor construction, the time required to obtain a detectable signal for TOR in the blood could be significantly reduced. This could contribute to reduce waiting times which is beneficial both to patients and doctors involved, as well as cost-effective. Furthermore, the importance of the CYP2C9 enzyme in the 4-hydroxylation of TOR was recently reported by Watanabe and co-workers.[6] Thus, the sensor could additionally serve as a tool for further understanding the role of the CYP2C9 enzyme in the 4-hydroxylation of TOR to form 4OH-TOR.



4.5 References

- [1] R.L. Siegel, K.D. Miller, A. Jemal, *Cancer Statistics*, 2017, *A Cancer J. Clin.* 67 (2017) 7–30. doi:10.3322/caac.21387.
- [2] P. Chalasani, J. Kiluk V, *Breast Cancer, MedScape.* (2017) 4–6. <http://emedicine.medscape.com/article/1947145-overview>.
- [3] R. Kumar Gara, V. Sundram, S. C. Chauhan, M. Jaggi, *Anti-Cancer Potential of a Novel SERM Ormeloxifene*, 20 (2014) 4177–4184.
- [4] S. Pyrhonen, R. Valavaara, H. Modig, M. Pawlicki, T. Pienkowski, S. Gundersen, J. Bauer, G. Westman, S. Lundgren, *Comparison of toremifene and tamoxifen in postmenopausal patients with advanced breast cancer : a randomized double-blind , the â€™ nordic â€™ phase III study*, *Br. J. Cancer.* 76 (1997) 270–277.
- [5] S. Pyrhönen, J. Ellm, J. Vuorinen, M. Gershanovich, T. Tominaga, M. Kaufmann, D.F. Hayes, *Meta-analysis of trials comparing toremifene with tamoxifen and factors predicting outcome of antiestrogen therapy in postmenopausal women with breast cancer*, *Breast Cancer Res. Treat.* 56 (1999) 133–143.
- [6] M. Watanabe, N. Watanabe, S. Maruyama, T. Kawashiro, *Comparative metabolic study between two selective estrogen receptor modulators , toremifene and tamoxifen , in human liver microsomes **, *Drug Metab. Pharmacokinet.* 30 (2015) 325–333.
- [7] Y. Jin, Z. Desta, V. Stearns, B. Ward, H. Ho, K. Lee, T. Skaar, A.M. Storniolo, L. Li, A. Araba, R. Blanchard, A. Nguyen, L. Ullmer, J. Hayden, S. Lemler, R.M. Weinshilboum, J.M. Rae, D.F. Hayes, D.A. Flockhart, *CYP2D6 Genotype, Antidepressant Use, and Tamoxifen Metabolism During Adjuvant Breast Cancer Treatment*, *J. Natl. Cancer Inst.* 97 (2005) 30–39. doi:10.1093/jnci/dji005.
- [8] S. Borges, Z. Desta, L. Li, T.C. Skaar, B.A. Ward, A. Nguyen, Y. Jin, A.M. Storniolo, D.M. Nikoloff, L. Wu, G. Hillman, D.F. Hayes, V. Stearns, D.A. Flockhart, *Quantitative effect of CYP2D6 genotype and inhibitors on tamoxifen metabolism: Implication for optimization of breast cancer treatment*, *Clin. Pharmacol. Ther.* 80 (2006) 61–74. doi:10.1124/jpet.104.065607.
- [9] C.L. Vogel, M.A. Johnston, C. Capers, D. Braccia, *Toremifene for Breast Cancer : A Review of 20 Years of Data*, *Clin. Breast Cancer.* 14 (2014) 1–9. doi:10.1016/j.clbc.2013.10.014.
- [10] K. Arvanitidis, G. Ragia, M. Iordanidou, S. Kyriaki, A. Xanthi, A. Tavridou, V.G. Manolopoulos, *Genetic polymorphisms of drug-metabolizing enzymes CYP2D6, CYP2C9, CYP2C19 and CYP3A5 in the Greek population*, *Fundam. Clin. Pharmacol.* 21 (2007) 419–426. doi:10.1111/j.1472-8206.2007.00510.x.
- [11] N. Widmer, C. Bardin, E. Chatelut, A. Paci, G. Veal, A. Astier, J. Beijnen, D. Leve, *Review of therapeutic drug monitoring of anticancer drugs part two – Targeted therapies*, *Eur. J. Cancer.* 50 (2014) 2020–2036.
- [12] A. Haouala, B. Zanolari, B. Rochat, M. Montemurro, K. Zaman, M.A. Duchosal, H.B. Ris, S. Leyvraz, N. Widmer, L.A. Decosterd, *Therapeutic Drug Monitoring of the new targeted anticancer agents imatinib, nilotinib, dasatinib, sunitinib, sorafenib and lapatinib by LC tandem mass spectrometry*, *J. Chromatogr. B Anal. Technol. Biomed. Life Sci.* 877 (2009) 1982–1996. doi:10.1016/j.jchromb.2009.04.045.

- [13] S. Bouchet, E. Chauzit, D. Ducint, N. Castaing, M. Canal-Raffin, N. Moore, K. Titier, M. Molimard, Simultaneous determination of nine tyrosine kinase inhibitors by 96-well solid-phase extraction and ultra performance LC/MS-MS, *Clin. Chim. Acta.* 412 (2011) 1060–1067. doi:10.1016/j.cca.2011.02.023.
- [14] N. Widmer, A. Béguin, B. Rochat, T. Buclin, T. Kovacovics, M.A. Duchosal, S. Leyvraz, A. Rosselet, J. Biollaz, L.A. Decosterd, Determination of imatinib (Gleevec®) in human plasma by solid-phase extraction-liquid chromatography-ultraviolet absorbance detection, *J. Chromatogr. B Anal. Technol. Biomed. Life Sci.* 803 (2004) 285–292. doi:10.1016/j.jchromb.2004.01.006.
- [15] S. Pursche, O.G. Ottmann, G. Ehninger, E. Schleyer, High-performance liquid chromatography method with ultraviolet detection for the quantification of the BCR-ABL inhibitor nilotinib (AMN107) in plasma, urine, culture medium and cell preparations, *J. Chromatogr. B Anal. Technol. Biomed. Life Sci.* 852 (2007) 208–216. doi:10.1016/j.jchromb.2007.01.019.
- [16] E.O. Aranda, J. Esteve-Romero, M. Rambla-Alegre, J. Peris-Vicente, D. Bose, Development of a methodology to quantify tamoxifen and endoxifen in breast cancer patients by micellar liquid chromatography and validation according to the ICH guidelines, *Talanta.* 84 (2011) 314–318. doi:10.1016/j.talanta.2011.01.022.
- [17] M.M.P.S. Neves, M.B. González-García, C. Delerue-Matos, A. Costa-García, Multiplexed electrochemical immunosensor for detection of celiac disease serological markers, *Sensors Actuators B Chem.* 187 (2013) 33–39. doi:10.1016/j.snb.2012.09.019.
- [18] H. Wang, Y. Zhang, H. Yu, D. Wu, H. Ma, H. Li, B. Du, Q. Wei, Label-free electrochemical immunosensor for prostate-specific antigen based on silver hybridized mesoporous silica nanoparticles, *Anal. Biochem.* 434 (2013) 123–127. doi:10.1016/j.ab.2012.11.012.
- [19] E.-H. Yoo, S.-Y. Lee, Glucose Biosensors: An Overview of Use in Clinical Practice, *Sensors.* 10 (2010) 4558–4576. doi:10.3390/s100504558.
- [20] E. Schneider, D.S. Clark, Cytochrome P450 (CYP) enzymes and the development of CYP biosensors, *Biosens. Bioelectron.* 39 (2013) 1–13. doi:10.1016/j.bios.2012.05.043.
- [21] P.M. Ndagili, A.M. Jijana, P.G.L. Baker, E.I. Iwuoha, 3-Mercaptopropionic acid capped ZnSe quantum dot-cytochrome P450 3A4 enzyme biotransducer for 17 β -estradiol, *J. Electroanal. Chem.* 653 (2011) 67–74. doi:10.1016/j.jelechem.2010.12.029.
- [22] L.I.U. Xing, L.U.O. Yang, Surface Modifications Technology of Quantum Dots Based Biosensors and Their Medical Applications, *Chinese J. Anal. Chem.* 42 (2014) 1061–1069. doi:10.1016/S1872-2040(14)60753-2.
- [23] T. Hu, L. Zhang, W. Wen, X. Zhang, S. Wang, Enzyme catalytic amplification of miRNA-155 detection with graphene quantum dot-based electrochemical biosensor, *Biosens. Bioelectron.* 77 (2016) 451–456. doi:10.1016/j.bios.2015.09.068.
- [24] P. Singh, S.K. Pandey, J. Singh, S. Srivastava, S. Sachan, S.K. Singh, Biomedical Perspective of Electrochemical Nanobiosensor, *Nano-Micro Lett.* 8 (2016) 193–203. doi:10.1007/s40820-015-0077-x.

- [25] E. Nxusani, P.M. Ndangili, R. a. Olowu, a. N. Jijana, T. Waryo, N. Jahed, R.F. Ajayi, P. Baker, E.I. Iwuoha, 3-Mercaptopropionic Acid Capped Ga₂Se₃nanocrystal-CYP3A4 Biosensor for the Determination of 17-Alpha-Ethinyl Estradiol in Water, *Nano Hybrids*. 1 (2012) 1–22. doi:10.4028/www.scientific.net/NH.1.1.
- [26] X. Xu, J. Qian, J. Yu, Y. Zhang, S. Liu, Cytochrome P450 enzyme functionalized-quantum dots as photocatalysts for drug metabolism, *Chem. Commun.* 1 (2014) 7607–7610. doi:10.1039/c4cc01717j.
- [27] T. Zeng, S. Leimkühler, J. Koetz, U. Wollenberger, Effective Electrochemistry of Human Sulfite Oxidase Immobilized on Quantum-Dots-Modified Indium Tin Oxide Electrode, *ACS Appl. Mater. Interfaces*. 7 (2015) 21487–21494. doi:10.1021/acsami.5b06665.
- [28] J. Qian, W. Zhu, L. Mi, X. Xu, J. Yu, D. Cui, Y. Xue, S. Liu, Nanohybrids of quantum dots and cytochrome P450 for light-driven drug metabolism, *J. Electroanal. Chem.* 733 (2014) 27–32. doi:10.1016/j.jelechem.2014.09.012.
- [29] P. Zhang, W. Tan, Atomic force microscopy for the characterization of immobilized enzyme molecules on biosensor surfaces, *Fresenius J. Anal. Chem.* 369 (2001) 302–307.
- [30] C.R. Raj, A.I. Abdelrahman, T. Ohsaka, Gold nanoparticle-assisted electroreduction of oxygen, *Electrochem. Commun.* 7 (2005) 888–893. doi:10.1016/j.elecom.2005.06.005.
- [31] M. Yang, J.L. Kabulski, L. Wollenberg, X. Chen, M. Subramanian, T.S. Tracy, D. Lederman, P.M. Gannett, N. Wu, Electrocatalytic Drug Metabolism by CYP2C9 Bonded To A Self-Assembled Monolayer Modified Electrode, *Drug Metab. Dispos.* 37 (2008) Under Revision. doi:10.1124/dmd.108.025452.In.
- [32] D.A.C. Brownson, C.E. Banks, *The Handbook of Graphene Electrochemistry*, Springer, 2014. doi:10.1007/978-1-4471-6428-9.
- [33] E.A. Schneider, Oriented Attachment of Cytochrome P450 2C9 to a Self-Assembled Monolayer on a Gold Electrode as a Biosensor Design, University of California, 2011.
- [34] M. Mazzarino, I. Fiacco, X. de la Torre, F. Botrè, A mass spectrometric approach for the study of the metabolism of clomiphene, tamoxifen and toremifene by liquid chromatography time-of-flight spectroscopy, *Eur. J. Mass Spectrom.* 14 (2008) 171. doi:10.1255/ejms.921.
- [35] V.J. Wiebe, C.C. Benz, I. Shemano, T.B. Cadman, M.W. DeGregorio, Pharmacokinetics of toremifene and its metabolites in patients with advanced breast cancer, *Cancer Chemother. Pharmacol.* 25 (1990) 247–251. doi:10.1007/BF00684880.
- [36] J. Kim, C.C. Coss, C.M. Barrett, M.L. Mohler, C.E. Bohl, C.M. Li, Y. He, J.T. Dalton, Role and pharmacologic significance of cytochrome P-450 2D6 in oxidative metabolism of toremifene and tamoxifen †‡, *Int. J. Cancer.* 132 (2013) 1475–1485. doi:10.1002/ijc.27794.
- [37] K.T. Kivistö, K. Villikka, L. Nyman, M. Anttila, P.J. Neuvonen, Tamoxifen and toremifene concentrations in plasma are greatly decreased by rifampin, *Clin. Pharmacol. Ther.* 64 (1998) 648–654. doi:10.1016/S0009-9236(98)90055-8.
- [38] M. Anttila, S. Laakso, P. Nyländen, E.A. Sotaniemi, Pharmacokinetics of the novel antiestrogenic agent toremifene in subjects with altered liver and kidney function, *CPT*

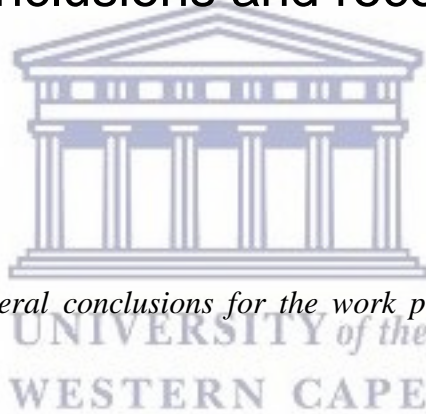
- Clin. Pharmacol. Ther. 57 (1995) 628–635. doi:10.1016/0009-9236(95)90225-2.
- [39] NJ Bridgewater, Fareston_ [package insert], Kyowa Kirin Inc. (1997). <http://www.fareston.com/uploads/documents/fareston-pi.pdf>.
- [40] S. Mendoza, E. Bustos, J. Manríquez, L.A. Godínez, Voltammetric Techniques, in: Handb. Instrum. Tech. Anal. Chem., 2015: pp. 21–48. doi:10.1002/9781118684030.ch2.
- [41] K. Auclair, Z. Hu, D.M. Little, P.R. Ortiz de Montellano, J.T. Groves, Revisiting the mechanism of P450 enzymes with the radical clocks norcarane and spiro[2,5]octane, J. Am. Chem. Soc. 124 (2002) 6020–6027. doi:10.1021/ja025608h.
- [42] N. Bistolas, U. Wollenberger, C. Jung, F.W. Scheller, Cytochrome P450 biosensors - A review, Biosens. Bioelectron. 20 (2005) 2408–2423. doi:10.1016/j.bios.2004.11.023.
- [43] G.E. Hrycay, M.S. Bandiera, Monooxygenase, Peroxidase and Peroxygenase Properties and Mechanisms of Cytochrome, Springer, 2015.
- [44] D.L. Nelson, M.M. Cox, Principles of Biochemistry, Fifth, W.H Freeman and Company, New York, 2008.



Chapter 5: Conclusions and recommendations

Summary

The chapter presents the general conclusions for the work presented together with future recommendations.



5.1 Conclusions and recommendations

The aim of this work was to produce a quantum dot (QD) based enzymatic electrochemical biosensor for the purpose of detecting toremifene (TOR), a medication used for breast cancer treatment. The biosensor would consist of a gold electrode modified with: a cysteamine self-assembled monolayer, water-soluble copper selenide quantum dots (CuSe QDs) and cytochrome P450 (CYP) 2C9 enzyme. This construct would serve as a proof of concept model for a therapeutic drug monitoring (TDM) device for measuring plasma concentration of the toremifene drug in the blood plasma in patients.

The aim of the work required synthesis of water-soluble CuSe QDs that could be conjugated to the CYP2C9 enzyme. Chapter 3 of this work described the successful synthesis of water-soluble, biocompatible CuSe QDs using three different capping agents: 6-mercaptohexanoic acid (6MHA), 3-mercaptopropionic acid (3MPA) and mercaptosuccinic acid (MSA). The method presented for synthesis of the CuSe QDs, is an aqueous route and thus free from potentially harmful or costly organic solvents. Furthermore, the method is rapid and requires no heating or expensive equipment. This is a contribution to the knowledge regarding synthesis of copper selenide QDs. It shows advantages to many other routes reported on the synthesis of CuSe QDs that require heating, specialized equipment and/or are time consuming.[1–14] To the best of our knowledge, copper selenide QDs has never been capped with 6MHA, 3MPA or MSA before. Thus, this work presents not only a novel route for synthesis of CuSe QDs but also presents a novel type of surface modified CuSe QDs. The study showed that the choice of capping agent had effect on stoichiometry and average particle size of the CuSe QDs. This had further effect on the optical and electrochemical properties. A summary of the characterized properties of the 6MHA-, 3MPA- and MSACuSe QDs is summarized in Table 5.1. The aim of the surface modifications was to improve the water soluble properties of the QDs, in order to make biological applications possible. The good electrochemical properties and biocompatible nature of the QDs made them a possible alternative for different biological applications for instance through bioconjugation with other organic molecules. An example of such applications is to serve as a component in enzymatic electrochemical biosensors, which was demonstrated in this work.

| Type of QDs | Average core diameter (nm) (HRTEM) | Average core diameter (nm) (SAXSpace) | Average hydrodynamic size (nm) (DLS) | Optical band gap: E _g /E _g (eV) (UV-vis absorption) | λ _{max} (nm) (UV-vis absorption) | Fluorescence wavelength (nm) (Photoluminescence) | Formal potential E ⁰ (mV) (CV) | Functional groups (FTIR) |
|-------------|------------------------------------|---------------------------------------|--------------------------------------|---|---|--|---|--------------------------------|
| 6MHACuSe | 8.97 (± 2.27) | 5.6 | 78.8 | 2.44/1.77 | 435 | 435 | 113.5-137 | CH ₂ , COOH, C-S |
| 3MPACuSe | 9.77 (± 2.79) | 8 | 105.7 | 2.98/1.79 | 400 | 435 | 145-170.5 | CH ₂ , COOH, C-S |
| MSACuSe | 9.90 (± 4.35) | 4 | 50.8 | 3.26/2.83 | 340 | 485 | 153-194 | - |

Table 5.1 Summary of the characterized properties of the synthesized 6MHACuSe, 3MPACuSe and MSACuSe QDs.

The 6MHACuSe QDs was applied as a component in the intended biosensor construct for detection of TOR. The study showed that the 6MHACuSe QDs contributed to retaining the CYP2C9 enzyme catalytic properties in comparison to only cysteamine as an enzyme immobilizer. This was confirmed through cyclic voltammetry (CV) studies. The biosensor response was also investigated using square-wave voltammetry (SWV). Control studies confirms that it is the addition of TOR that causes the change in reduction current in the presence of CYP2C9 enzyme on the electrode surface. Indicating that the metabolic properties of the enzyme were retained. This is further confirmed by the fact that the biosensor response followed the typical Michaelis-Menten kinetics for enzyme based biotransducers.[15] The small K_M^{APP} values obtained for CV and SWV (0.08 pM and 0.27 pM respectively) indicates high binding affinity between the substrate and CYP2C9 enzyme on the electrode surface. Though, the dynamic linear range (DLR) obtained from the CV measurements was very small (up to 0.3 pM, $R^2 = 0.85078$) with a sensitivity of 241.2 nA pM^{-1} and limit of detection (LOD) corresponding to 0.28 pg mL^{-1} . The SWV measurements gave a DLR up to 0.6 pM ($R^2 = 0.98432$). The sensitivity obtained was 212.7 nA pM^{-1} with a LOD corresponding to 0.08 pg mL^{-1} . By using SWV instead of CV, the DLR was slightly improved. Toremifene in blood plasma or urine samples is commonly determined by HPLC or LC-MS/MS techniques and the LOD ranges within $0.2 - 30 \text{ ng mL}^{-1}$. [16–21] In addition, the LODs of the biosensor constructs is significantly lower than reported steady state plasma concentrations (C_{ss}) reported amongst patients with advanced breast cancer administered with 60 mg (normal daily dose) of TOR. Amongst these patients, $C_{ss} = 879 \text{ ng mL}^{-1}$. [18,22] Thus, the biosensor has potential of detecting presence of very small amounts of toremifene in plasma samples. This potential could be time-saving for doctors utilizing such a TDM device in practice. Peak plasma concentration levels amongst patients administered with 60 mg of TOR is reached between 1.5-3 h.[18]

Because of the low detection limit of the biosensor construction, the time required to obtain a detectable signal for TOR in the blood could be significantly reduced. This could contribute to reduce waiting times which is beneficial both to patients and doctors involved, as well as cost-effective. Thus, the biosensor construct has potential of serving as a more time and cost-efficient tool in comparison to the conventional methods that are used today for determination of TOR plasma or urine concentration. Furthermore, the biosensor also serves as a model to simulate one part of the phase I metabolic pathway of TOR. Lohmann and co-workers [23] used an enzyme based electrochemical system for the simulation of the TOR phase I and phase II metabolism. The system utilized an in an electrochemical flow-through cell in combination

with a LC/MS system in combination with the enzyme glutathione-S-transferase. However, to the best of our knowledge, an electrochemical biotransducers with the purpose of studying the interaction between CYP2C9 and TOR has not been reported before. The importance of the CYP2C9 enzyme in the 4-hydroxylation of TOR was recently reported by Watanabe and co-workers.[16] Thus, the sensor could additionally serves as a tool for further understanding the role of the CYP2C9 enzyme in the phase I metabolic pathway forming 4-hydroxyl-toremifene. This could further contribute to increased understanding of the metabolic pathway of the breast cancer medication and also understanding of the CYP metabolism of xenobiotics in the body.

In the work presented, novel water-soluble CuSe QDs were synthesized, characterized and applied in the successful construction of a proof of concept enzymatic electrochemical biosensor for the detection of TOR in aqueous solution. Through this, the work has contributed to further understanding the CYP catabolized metabolic pathway of TOR as well as contributing to further knowledge about the CYP metabolism of xenobiotics in the human body. The biosensor construct has potential to serve as an easier, quicker and cheaper alternative for determining the TOR plasma concentration of breast cancer patients administered with the drug. This in comparison to the techniques used today for such measurements (mainly HPLC or LC-MS/MS techniques) that has potential issues regarding shipments to distant laboratory, extensive costs of the potentially expensive equipment, potential delays caused by delivery of results and possibly complex interpretation of data. [24] This could contribute to early determination of potential plasma variations caused by CYP polymorphism or drug-drug interactions, with the purpose of conducting more effective individualize treatment. This is in agreement with the guidelines for early cancer diagnostics presented by the world health organization (WHO), 2017. In these guidelines, WHO empathizes the need to access high-quality, affordable treatments within a short time frame from the diagnosis, in order to treat cancer in an early stage of the disease.[25] Such treatments could certainly involve personalized treatment using TDM, which then requires quick and low-cost equipment in order to make such treatments available for all breast cancer patients treated with TOR. Thus, in support of the WHO guidelines for early cancer treatment and diagnostics, there is a world-wide benefit of TDM devices as the one constructed in this work.

5.2 References

- [1] X. She, Q. Zhang, C. Wang, S. Chen, New insights into the phosphine-free synthesis of ultrasmall Cu_{2-x}Se nanocrystals at the liquid – liquid interface, *R. Soc. Chem. Adv.* 5 (2015) 90705–90711. doi:10.1039/c5ra18313h.
- [2] H. Shen, H. Wang, H. Yuan, L. Ma, L. Song Li, Size-, shape-, and assembly-controlled synthesis of Cu₂xSe nanocrystals via a non-injection phosphine-free colloidal method, *CrystEngComm.* 14 (2012) 555–560. doi:10.1039/c1ce05887h.
- [3] O.A. Balitskii, M. Sytnyk, J. Stangl, D. Primetzhofer, H. Groiss, W. Heiss, Tuning the Localized Surface Plasmon Resonance in Cu_{2-x}Se Nanocrystals by Postsynthetic Ligand Exchange, (2014) 2–7.
- [4] O.U. Chen, *Doped and Undoped Nanoparticles: Synthesis and Characterization*, 2010.
- [5] H. Li, Y. Zhu, S. Avivi, O. Palchik, J. Xiong, Y. Kolytyn, V. Palchik, A. Gedanken, Sonochemical process for the preparation of a -CuSe nanocrystals and flakes {, (2002) 3723–3727. doi:10.1039/b206193g.
- [6] C.W.E.I. Soon, *Synthesis and Characterisation of Copper Selenide Nanoparticles via Emulsion Technique*, 2011.
- [7] S.L. White, P. Banerjee, P.K. Jain, Liquid-like cationic sub-lattice in copper selenide clusters, *Nat. Commun.* (2017) 1–11. doi:10.1038/ncomms14514.
- [8] B. GAHTORI, S. BATHULA, K. TYAGI, A.K. SRIVASTAVA, A. Dhar, R.C. Budhani, Nanostructured copper - selenide with high thermoelectric figure - of - merit and process for the preparation thereof, 2015.
- [9] C. Nanoparticles, B.M.A. Malik, P.O. Brien, A Novel Route for the Preparation of CuSe and, d (1999) 1441–1444.
- [10] S. Govindraj, M.P. Kalenga, M. Airo, M.J. Moloto, L.M. Sikhwivhilu, N. Moloto, Size quantization in Cu₂Se nanocrystals, *Opt. Mater. (Amst).* 38 (2014) 310–313.
- [11] P.P. Ingole, P.M. Joshi, S.K. Haram, Room temperature synthesis of 1-hexanethiolate capped Cu_{2-x}Se quantum dots, in Triton X-100 water-in-oil microemulsions, *Colloids Surfaces A Physicochem. Eng. Asp.* 337 (2009) 136–140. doi:10.1016/j.colsurfa.2008.12.011.

- [12] K. Kaviyarasu, A. Ayeshamariam, E. Manikandan, J. Kennedy, R. Ladchumananandasivam, U. Umbelino De Gomes, M. Jayachandran, M. Maaza, Solution processing of CuSe quantum dots : Photocatalytic activity under RhB for UV and visible-light solar irradiation Dear Author , added to the article before publication , but are not reflected, Mater. Sci. Eng. B. 210 (2016) 1–9. doi:10.1016/j.mseb.2016.05.002.
- [13] P.M. Kalenga, Supervisors:, N. Moloto, J. Moloto, L.M. Sikhwivhilu, Synthesis and characterization of copper chalcogenide nanoparticles and their use in solution processed photovoltaics, 2015.
- [14] P. Kumar, K. Singh, Synthesis , characterizations , and optical properties of copper selenide quantum dots, (2011) 103–110. doi:10.1007/s11224-010-9698-3.
- [15] P.M. Ndagili, A.M. Jijana, P.G.L. Baker, E.I. Iwuoha, 3-Mercaptopropionic acid capped ZnSe quantum dot-cytochrome P450 3A4 enzyme biotransducer for 17B-estradiol, J. Electroanal. Chem. 653 (2011) 67–74. doi:10.1016/j.jelechem.2010.12.029.
- [16] M. Watanabe, N. Watanabe, S. Maruyama, T. Kawashiro, Comparative metabolic study between two selective estrogen receptor modulators , toremifene and tamoxifen , in human liver microsomes *, Drug Metab. Pharmacokinet. 30 (2015) 325–333.
- [17] M. Mazzarino, I. Fiacco, X. de la Torre, F. Botrè, A mass spectrometric approach for the study of the metabolism of clomiphene, tamoxifen and toremifene by liquid chromatography time-of-flight spectroscopy, Eur. J. Mass Spectrom. 14 (2008) 171. doi:10.1255/ejms.921.
- [18] V.J. Wiebe, C.C. Benz, I. Shemano, T.B. Cadman, M.W. DeGregorio, Pharmacokinetics of toremifene and its metabolites in patients with advanced breast cancer, Cancer Chemother. Pharmacol. 25 (1990) 247–251. doi:10.1007/BF00684880.
- [19] J. Kim, C.C. Coss, C.M. Barrett, M.L. Mohler, C.E. Bohl, C.M. Li, Y. He, J.T. Dalton, Role and pharmacologic significance of cytochrome P-450 2D6 in oxidative metabolism of toremifene and tamoxifen †‡, Int. J. Cancer. 132 (2013) 1475–1485. doi:10.1002/ijc.27794.
- [20] K.T. Kivistö, K. Villikka, L. Nyman, M. Anttila, P.J. Neuvonen, Tamoxifen and toremifene concentrations in plasma are greatly decreased by rifampin, Clin.

- Pharmacol. Ther. 64 (1998) 648–654. doi:10.1016/S0009-9236(98)90055-8.
- [21] M. Anttila, S. Laakso, P. Nyländen, E.A. Sotaniemi, Pharmacokinetics of the novel antiestrogenic agent toremifene in subjects with altered liver and kidney function, *CPT Clin. Pharmacol. Ther.* 57 (1995) 628–635. doi:10.1016/0009-9236(95)90225-2.
- [22] NJ Bridgewater, Fareston_ [package insert], Kyowa Kirin Inc. (1997).
<http://www.fareston.com/uploads/documents/fareston-pi.pdf>.
- [23] W. Lohmann, U. Karst, Electrochemistry meets enzymes: Instrumental on-line simulation of oxidative and conjugative metabolism reactions of toremifene, *Anal. Bioanal. Chem.* 394 (2009) 1341–1348. doi:10.1007/s00216-008-2586-7.
- [24] N. Widmer, C. Bardin, E. Chatelut, A. Paci, G. Veal, A. Astier, J. Beijnen, D. Leve, Review of therapeutic drug monitoring of anticancer drugs part two – Targeted therapies, *Eur. J. Cancer.* 50 (2014) 2020–2036.
- [25] World health organization, *Guide to cancer early diagnosis*, Geneva, 2017.

